# Oxide thermoelectrics
# via a glass-ceramic route

Dissertation
zur Erlangung des Grades
***"Doktor der Naturwissenschaften"***

am Fachbereich Physik, Mathematik und Informatik
der Johannes Gutenberg-Universität
in Mainz

(Julian Lingner)

geb. in Münster
Mainz, 2015

Datum der mündlichen Prüfung
24.04.2015

# Kurzdarstellung

Thermoelektrizität beschreibt die reversible Beeinflussung und Wechselwirkung von Elektrizität und Temperatur $T$ in Systemen abseits des thermischen Gleichgewichtes. In diesen führt ein Temperaturgradient entlang eines thermoelektrischen Materials zu einem kontinuierlichen Ungleichgewicht in der Energieverteilung der Ladungsträger. Dies hat einen Diffusionsstrom der energiereichen Ladungsträger zum kalten Ende und der energiearmen Ladungsträger zum heißen Ende zur Folge. Da in offenen Stromkreisen kein Strom fließt, wird ein Ungleichgewicht der Ströme über das Ausbilden eines elektrischen Feldes kompensiert. Die dadurch entstehende Spannung wird als Seebeck Spannung bezeichnet. Über einen geeigneten Verbraucher, folgend aus dem Ohm' schen Gesetz, kann nun ein Strom fließen und elektrische Energie gewonnen werden. Den umgekehrten Fall beschreibt der sogenannte Peltier Effekt, bei dem ein Stromfluss durch zwei unterschiedliche miteinander verbundene Materialien ein Erwärmen oder Abkühlen der Kontaktstelle zur Folge hat. Die Effizienz eines thermoelektrischen Materials kann über die dimensionslose Größe $ZT = \frac{S^2 \sigma}{\kappa} T$ charakterisiert werden. Diese setzt sich zusammen aus den materialspezifischen Größen der elektrischen Leitfähigkeit $\sigma$, der thermischen Leitfähigkeit $\kappa$ und dem Seebeck Koeffizienten $S$ als Maß der erzeugten Spannung bei gegebener Temperaturdifferenz. Diese Arbeit verfolgt den Ansatz glaskeramische Materialien mit thermoelektrischen Kristallphasen zu synthetisieren, sie strukturell zu charakterisieren und ihre thermoelektrischen Eigenschaften zu messen, um eine Struktur-Eigenschaft Korrelation zu erarbeiten. Hierbei werden im Detail eine elektronenleitende (Hauptphase $SrTi_xNb_{1-x}O_3$) sowie eine löcherleitende Glaskeramik (Hauptphase $Bi_2Sr_2Co_2O_y$) untersucht. Unter dem Begriff Glaskeramiken sind teilkristalline Materialien zu verstehen, die aus Glasschmelzen durch gesteuerte Kristallisation hergestellt werden können. Über den Grad der Kristallisation und die Art der ausgeschiedenen Spezies an Kristallen lassen sich die physikalischen Eigenschaften dieser Systeme gezielt beeinflussen. Glaskeramiken bieten, verursacht durch ihre Restglasphase, eine niedrige thermische Leitfähigkeit und die Fermi Energie lässt sich durch Dotierungen in Richtung des Leitungs- oder Valenzbands verschieben. Ebenso besitzen glaskeramische Materialien durch ihre Porenfreiheit verbesserte mechanische Eigenschaften gegenüber Keramiken und sind weniger anfällig für den Einfluss des Sauerstoffpartialdruckes $p_{O_2}$ auf die Parameter. Ein glaskeramisches und ein gemischt keramisch/glaskeramisches thermoelektrisches Modul aus den entwickelten Materialien werden konzipiert, präpariert, kontaktiert und bezüglich ihrer Leistung vermessen.

# Abstract

Thermoelectricity describes the reversible influence and interaction of electricity and temperature $T$ in systems away from thermal equilibrium. A temperature gradient across a thermoelectric material leads to a continuous imbalance of the energy distribution of the charge carriers. This results in a diffusion current of the energy-rich charge carriers towards the cold end, while the low-energy charge carriers flow towards the hot end. Because no current can flow in an open circuit, an imbalance in these currents is compensated by the formation of an electrical field. The resulting voltage is called Seebeck voltage. According to Ohm's law, a current will flow if a load resistance is applied to the setup, so the temperature difference is responsible for the generation of electrical energy. Vice versa, the Peltier effect can be observed, if current flows through two different materials and their contact junction heats up or cools down in the process. The efficiency of a thermoelectric material is characterized by the dimensionless figure of merit $ZT = \frac{S^2\sigma}{\kappa}T$. This quantity is composed of material dependent properties, namely the electrical conductivity $\sigma$, the thermal conductivity $\kappa$ and the Seebeck coefficient $S$, which is a measure for the voltage drop across the material at a given temperature difference. Under normal circumstances, these values cannot be modified independently from each other, therefore, concepts of low dimensional structuring and new materials to enhance the power are part of ongoing research. This thesis presents the approach of synthesizing glass-ceramic materials with thermoelectric crystal phases. A structural characterization is shown and their thermoelectric properties are measured in order to establish a structure-property correlation. For that, an electron-conducting (main phase $SrTi_xNb_{1-x}O_3$) as well as a hole-conducting glass-ceramic (main phase $Bi_2Sr_2Co_2O_y$) are investigated. Here, the terminology glass-ceramics covers semi-crystalline materials, which are fabricated by glass melts and a subsequent heat treatment. The degree of crystallization and the species of precipitated crystals can specifically influence the physical properties of the system. Due to their residual glass phase, glass-ceramics offer a low thermal conductivity and their Fermi energy can be shifted towards the conduction or valence band by doping. Furthermore, glass-ceramic materials possess improved mechanical stability compared with ceramics and they are less susceptible to atmospheric influences like the oxygen partial pressure $p_{O_2}$. A glass-ceramic and a mixed ceramic/glass-ceramic thermoelectric module from the developed materials are designed, prepared, contacted, and characterized concerning their power output.

# Contents

# List of Figures

# 1. Introduction

Since the beginning of the Industrial Revolution, which started at the end of the 18th century, fossil fuels have been established as principal and reliable resources for the energy supply of mankind [Ola05]. Fossil fuels are substances like coal, petroleum and natural gas that are the result of natural, anaerobic decomposition processes of animal and vegetable organisms over a time span of millions of years [Ber03]. Today, these carbon based fuels are favored over the usage of alternative energy resources as can be seen from the frequency of their consumption and recent studies reveal that this trend will also continue in the future. In its "International Energy Outlook" report of 2013, the United States Energy Information Administration (EIA) predicts an increase of the overall world energy consumption from $W_{\text{world}} = 524$ to $820$ quadrillion ($10^{15}$) Btu[1] during the period of time between the year 2010 to 2040. This corresponds to an increase in energy demand of $56\%$ within the next 30 years [Dom13]. The total share of renewable energies among the different
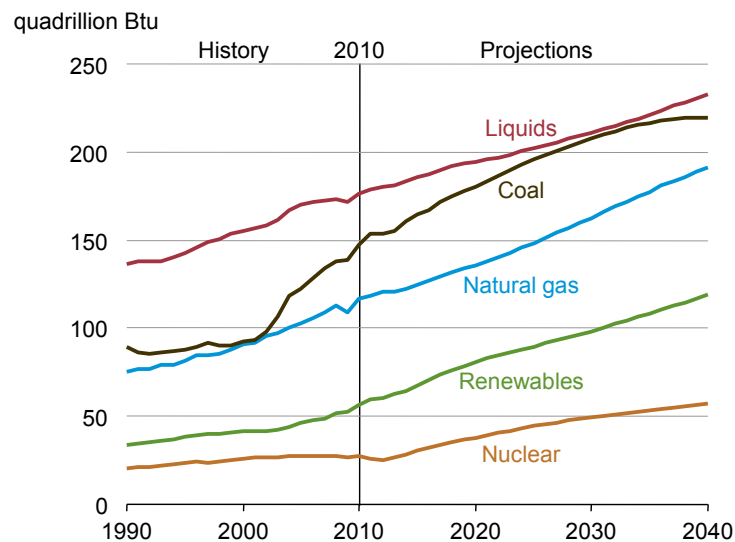


**Figure 1.1.:** World energy consumption by fuel type, 1990-2040 [Dom13]

competing forms of energy is strongly growing, however, power generation by fossil fuels still covers more than three quarters of the total demand according to the world

---

[1]British thermal unit, $1\,\text{Btu} = 1055.55\,\text{J}$

energy consumption (see figure 1.1). The extensive usage of fossil fuels comes with disadvantages and drawbacks due to several factors. The limited availability of the aforementioned natural resources and the huge timescale during which they are regenerated, leads to an increased scarcity of coal, petroleum and gas with growing consumption. Moreover, burning of those fossil fuels leads to enormous amounts of unwanted by-products like carbon dioxide ($CO_2$), which is seen as one of the main reasons for causing the greenhouse effect in the earth's atmosphere [HJL$^{+}$81]. Another important issue is the low efficiency of combustion processes due to the vast amount of waste heat that is emitted during operation. For example, combustion engines in automobiles only use about one third of the produced energy from gas to actually move the vehicle, while the rest is lost in the form of waste heat on the exhaust pipe, the coolant and by frictional effects [YC09]. While searching for alternatives to satisfy the global demand for energy, solar power comes into mind. Considering the average amount of solar radiation hitting the earth, solar energy is a potent and very powerful candidate to drastically lower the demand for energy obtained from fossil resources. Hypothetically speaking, solar cells with a conversion efficiency of $20\,\%$, which cover only $0.1\,\%$ of earth's land mass, would be sufficient to meet the total energy demand in the world [Lew05], [SP03]. Nevertheless, it has to be kept in mind that conversion of radiation energy comes along with the generation of large amounts of waste heat as well. In summary it can be expected that the primary energy consumption and waste heat production due to the prevalently used energy carriers will heavily increase in the near future. A central question will be, if and in what way this inevitable occurrence of waste heat can be taken advantage of.

A possibility to compensate for the presence of waste heat in industrial processes or combustion engines is the direct conversion of the temperature gradient $\Delta T$ into electrical power by using thermoelectric generators (TEG) as solid state energy converters. Their advantage is the fact, that they can operate without mechanically moving parts, which makes them very reliable, durable and low-maintenance. They can be found in various applications like sensor technology (thermocouples) or aerospace (radioisotope thermoelectric generators). State-of-the-art generators have the disadvantage of a comparably low waste heat to power conversion efficiency, which prevents them to be used more extensively in various fields. Nevertheless, the economical potential behind the vast amounts of waste heat can be illustrated by a simple calculation. Assuming that the power output of a nuclear power plant is about $P = 1400\,\mathrm{MW}$ (Neckarwestheim, Baden-Württemberg Germany [EnB14]), an availability of $100\,\%$ leads to an annual ($t = 24\,\mathrm{hours} \times 365\,\mathrm{days}$) energy yield of $W_a = Pt = 1400 \times 24 \times 365 = 12.26\,\mathrm{TWh}$. In 2010, the world energy consumption accord-

ing to the cited study was around $W_{\text{world}} = 524 \times 10^{15} \times 1055.55$ J, which corresponds to a requirement of $15.36 \times 10^4$ TWh. If it would be possible to reduce the consumed energy only by $0.1\%$ (e.g. more efficient, waste heat reduced technologies and processes), twelve nuclear power plants could be taken off the grid from an energy savings point of view. Of course this is a rather bold example, because not all of the annually consumed energy is emitted as waste heat. If only the actual annual waste heat output of Germany is taken into account, this accumulates to around $300$ TWh according to a study by [Drö13] in 2013. Taking advantage of this amount of energy with thermoelectric generators having an efficiency of $10\%$ would be equivalent to two nuclear power plants. This demonstrates that if it is possible to increase the efficiency of thermoelectric materials and therefore generators, they offer a high potential of saving large amounts of energy. In recent years, several approaches towards dealing with the task of enhancing the thermoelectric efficiency have been made. These are discussed in section 1.3 with their respective advantages and drawbacks. The following section covers the basic concept of thermoelectricity and necessary terms which are needed to describe it properly.

## 1.1. Thermoelectricity

Thermoelectricity describes the physical principles that focus on the conversion of temperature differences into electricity (and vice versa) using thermoelectric materials. These materials (usually electron conducting n-type and hole conducting p-type semiconductors) are used in thermoelectric modules, where they are electrically connected in series by metal contacts on a substrate material (usually $Al_2O_3$). Such a module can be used in the generator mode (see figure 1.2, a temperature gradient $\Delta T$ drives a current $I$) as well as in the refrigerator mode (see figure 1.3, a power source generates a temperature difference $\Delta T$). In these simplified illustrations, the thermoelectric module only consists of a single pair of electron and hole conducting materials. As it can be seen, both materials are connected via metallic contacts (black) to the substrate, the thermal gradient runs through the materials in parallel. Because the magnitude of thermovoltage $U$ generated by a single pair of materials is only about a few $100 \, \mu V$, many of these thermocouples are usually connected in series to yield a considerable output power.

As mentioned earlier, thermoelectric effects require a temperature difference, which is the reason why they have to be treated as non-equilibrium phenomena. Scientists like L. Onsager could develop important insights and contributions to a general theory for
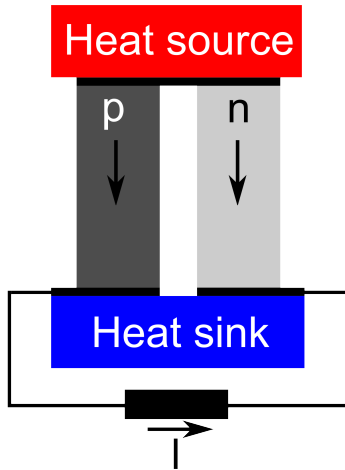
**Figure 1.2.:** Thermoelectric device, generator mode
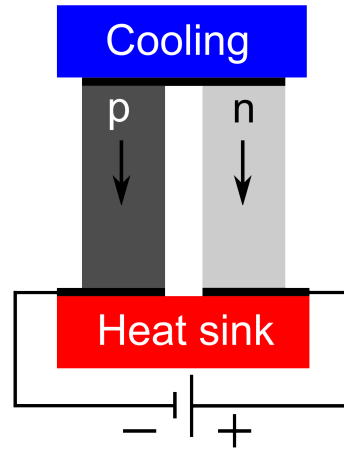


**Figure 1.3.:** Thermoelectric device, refrigerator mode

the treatment of those (i.e. Onsager reciprocal relations [Ons31a], [Ons31b]) and the derivation of the thermoelectric quantities from this theory is presented in section 5.1.5. For now, the discussion will assume, that the local deviation from thermal equilibrium is small, hence the principles and models of equilibrium thermodynamics can be applied. These are the illustration of the materials using band structure concepts with the corresponding Fermi energies $E_F$.

### 1.1.1. Seebeck effect

The first of the thermoelectric effects is the Seebeck effect. This effect describes the conversion of an external temperature difference into a voltage signal and is named after the German Baltic physicist T. J. Seebeck. In 1821, Seebeck discovered, that a compass needle got deflected if it was brought near a ring made of two different metals A and
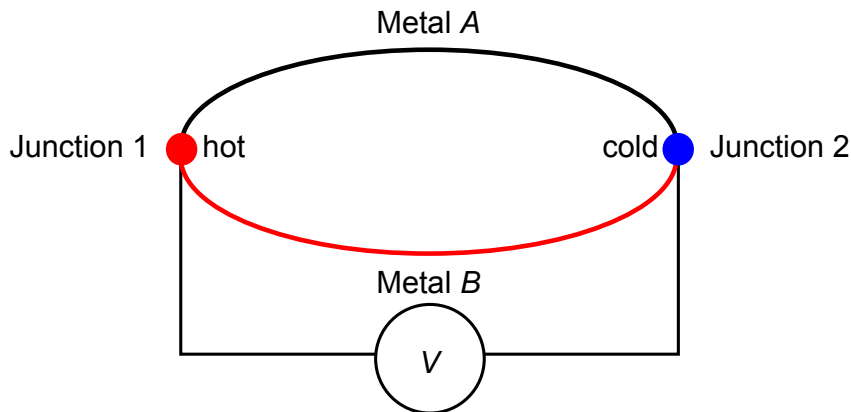


**Figure 1.4.:** Illustration of the Seebeck effect in a closed loop

B, when the junctions between the two metals were kept at different temperatures. This setup corresponds to a thermocouple, where the two different metals show a different response to the temperature difference and the arising ring current generates a magnetic field. At first, Seebeck did not find the correct explanation for this occurrence, which is why the phenomenon became known as the thermomagnetic effect [See22]. It was later clarified by H. C. Ørsted that electrical currents can be responsible for magnetic fields and the term thermoelectricity was established.

As a generalization, a temperature gradient that is applied to a thermoelectric module, leads to a voltage drop across the setup and if a load resistance is connected to the module, a current is able to flow (see figure 1.2). Here, the electrons move from the metallic contact into the p-type material. The electrons cross the material and after reentering the metallic contact, they pass through the n-type material back into the metallic wire.

$$f_0(E, T) = \frac{1}{e^{\frac{E-\mu}{k_B T}} + 1} \tag{1.1}$$

In order to understand the microscopic processes in a material that is subjected to a thermal gradient, it is beneficial to first consider the simple case of a single metal that is subjected to a temperature difference. Because the charge carriers are electrons, their energy distribution in the material is characterized by the Fermi distribution $f_0$. The expression of $f_0$ in equation (1.1) depends on the charge carrier energy $E$, the chemical potential $\mu$, the Boltzmann constant $k_B$ as well as the absolute temperature $T$. Considering figure 1.5, it can be seen that the Fermi distribution $f_0$ in the vicinity of $E_F$ is less steep for higher temperatures than it is for lower temperatures. Therefore, the hot end of the metal has a higher concentration of electrons above the Fermi level than the cold end (see figure 1.6). The temperature difference $\Delta T$ leads to a
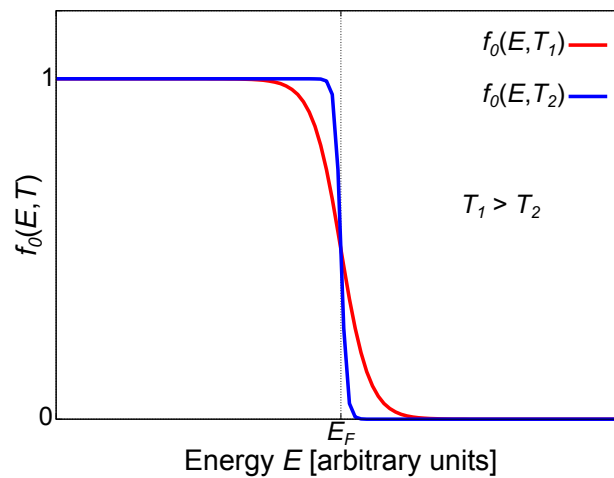


**Figure 1.5.:** Fermi distribution $f_0(E, T)$ for two temperatures $T_1 > T_2$

concentration gradient and the electrons in the material start to move from the hot to the cold side. This happens to compensate for the concentration gradient and because the "hot" electrons have a greater momentum than the "cold" electrons. This means, that on average, the diffusion from $T_h$ to $T_c$ happens faster than the other way around.



**Figure 1.6.:** Illustration of charge distribution in a metal

For semiconductors, an increase of the temperature usually leads to an increase of the charge carrier density. If the smearing range of the Fermi function ($\approx 2k_B T$) is smaller than the energy gap $E_g$, the Fermi function within the bands ($E < E_V$ and $E > E_C$) can be approximated using the Boltzmann distribution [IL09]. Using this, expressions for the charge carrier densities of intrinsic semiconductors $n_i$ can be obtained

$$n_n = 2 \left( \frac{2\pi m_n^\star k_B T}{h^2} \right)^{3/2} \exp\left( -\frac{E_L - E_F}{k_B T} \right) \tag{1.2}$$

$$n_p = 2 \left( \frac{2\pi m_p^\star k_B T}{h^2} \right)^{3/2} \exp\left( \frac{E_V - E_F}{k_B T} \right) \tag{1.3}$$

Equations 1.2 and 1.3 show, that an increase in temperature implies an increased charge carrier concentration in the case of semiconductors. Therefore, a temperature gradient across a semiconducting material leads to a concentration gradient of charge carriers. In order to break the symmetry between electrons and holes and reach high conductivities, semiconductors are usually doped with impurities. For doped semiconductors, free electrons in the conduction band may originate from the valence band as well as the impurity sites. The temperature dependence of the charge carrier density is therefore described by different expressions depending on whether excitation from the impurity sites or the valence band is prevalent. However, the general trend of increased carrier density with increasing temperature is also observed. When electrons move away from their respective donors (holes move away from their acceptors), they leave behind a positive (negative), immobile charge.

This leads to a formation of an electric field $E$ across the material, which opposes the concentration gradient $\frac{dn}{dx}$ and its resulting charge carrier diffusion. After a certain time, an equilibrium state is established, where the backflow of charge carriers caused by the electric field equals the diffusion current driven by the temperature difference. This relation is described by the drift-diffusion model [Bre99], which can be derived from the Boltzmann transport equation (1.4) and is discussed in the following part. If $f$ is assumed to be the distribution function of the particles, $\vec{v}$ the velocity, $\vec{F}$ the imposed force field, $\nabla_r$ and $\nabla_p$ the gradients with respect to spatial and momentum coordinates and $\left(\frac{\partial f}{\partial t}\right)_{\text{coll}}$ the collision term, the following expression for the distribution function can be obtained.

$$\frac{\mathrm{d}f}{\mathrm{d}t} = \frac{\partial f}{\partial t} + \vec{v}\,\nabla_r f + \vec{F}\,\nabla_p f = \left(\frac{\partial f}{\partial t}\right)_{\text{coll}} \tag{1.4}$$

A solution for this equation can be found, if the collision term on the right hand side is known or if a reasonable approximation can be made for it. In order to make this consideration as simple as possible, equation (1.4) will be considered for a one-dimensional case. Furthermore, stationary conditions ($\frac{\partial f}{\partial t} = 0$) as well as the relaxation time approximation $\left(\frac{\partial f}{\partial t}\right)_{\text{coll}} = -\frac{f(x,v)-f_0}{\tau}$ are assumed within the Boltzmann transport equation. Finally, the derivations are carried out under the assumptions of parabolic bands ($p = \hbar k$). The transport equation now reads

$$v\frac{\partial f}{\partial x} + \frac{eE}{m^\star}\frac{\partial f}{\partial v} = \frac{f_0 - f(x,v)}{\tau} \tag{1.5}$$

with the electric field $E$, the charge $e$ (negative for electrons, positive for holes), the effective mass $m^\star$, the velocity $v$, the position $x$ and the distribution function $f(x,v)$. In general, the current density $J(x)$ can be expressed as

$$J(x) = e\int v f(x,v)\,\mathrm{d}v \tag{1.6}$$

After multiplying equation (1.5) with $v$ and integrating over $v$, the right hand side reads

$$\frac{1}{\tau}\big[\underbrace{\int v f_0\,\mathrm{d}v}_{=0} - \int v f(x,v)\,\mathrm{d}v\big] = -\frac{J(x)}{e\tau} \tag{1.7}$$

The first integral vanishes because $f_0$ is symmetric in $v$. The left side of equation (1.5) yields

$$\frac{\mathrm{d}}{\mathrm{d}x}\int v^2 f(x,v)\,\mathrm{d}v + \frac{eE}{m^\star}\int v\frac{\partial f}{\partial v}\,\mathrm{d}v \tag{1.8}$$

Because the integral of the distribution function gives the charge carrier density $n$, partial integration leads to

$$\int v \frac{\partial f}{\partial v} \, \mathrm{d}v = \underbrace{\left[ v f(x,v) \right]_{-\infty}^{\infty}}_{=0} - \int f(x,v) \, \mathrm{d}v = -n(x) \tag{1.9}$$

$$\int v^2 f(x,v) \, \mathrm{d}v = n(x) \left\langle v^2 \right\rangle \tag{1.10}$$

Combining both parts of equation (1.7) and (1.8) yields expression (1.11).

$$J(x) = e\tau \frac{eE}{m^\star} n(x) - e\tau \frac{\mathrm{d}}{\mathrm{d}x} n(x) \left\langle v^2 \right\rangle \tag{1.11}$$

Making use of the expression for the charge carrier mobility $\mu = \frac{e\tau}{m^\star}$, the square velocity momentum $\left\langle v^2 \right\rangle = \frac{k_B T}{m^\star}$ as well as the diffusion coefficient $D = \frac{\mu k_B T}{e}$, the current density $J_i$ can be expressed by equation (1.12) and (1.13).

$$J_n(x) = \mu_n E(x) q n_n + q \frac{\mathrm{d}}{\mathrm{d}x} \left( D_n n_n \right) \tag{1.12}$$

$$J_p(x) = \mu_p E(x) q n_p - q \frac{\mathrm{d}}{\mathrm{d}x} \left( D_p n_p \right) \tag{1.13}$$

For this, $q$ as the absolute value of the electronic charge has been used. The first part describes the drift of the charge carriers due to the electrical field while the second part denotes the diffusion flow due to the concentration gradient. If the expression for the electrical conductivity $\sigma_i = q\, n_i\, \mu$ is used, the equations can be shortened to

$$J_n(x) = \sigma_n E(x) + q \frac{\mathrm{d}}{\mathrm{d}x} \left( D_n n_n \right) \tag{1.14}$$

$$J_p(x) = \sigma_p E(x) - q \frac{\mathrm{d}}{\mathrm{d}x} \left( D_p n_p \right) \tag{1.15}$$

In the case of a uniform material, the diffusion part of the equations can be rewritten by swapping the spatial and time derivations. It can be shown through experiments, that the term in brackets of equation (1.16) and (1.17) corresponds to the Seebeck coefficient $S$ scaled with the electrical conductivity $\sigma$ [BKSG13].

$$J_n(x) = \sigma_n E(x) + \underbrace{q \left( n_n \frac{\mathrm{d}D_n}{\mathrm{d}T} + D_n \frac{\mathrm{d}n_n}{\mathrm{d}T} \right)}_{-\sigma_n S_n} \frac{\mathrm{d}T}{\mathrm{d}x} \tag{1.16}$$
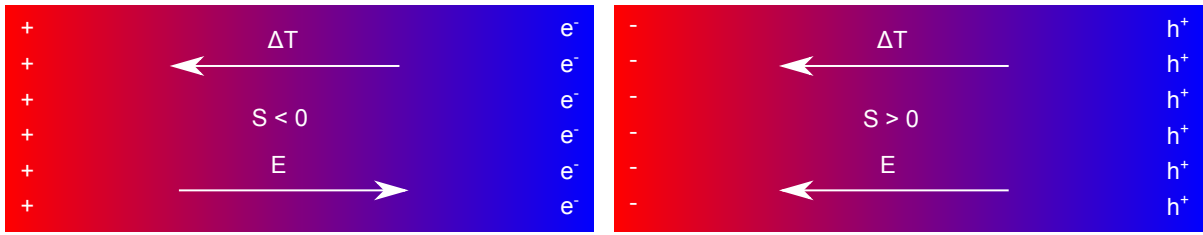
**Figure 1.7.:** Convention for the sign of the Seebeck coefficient $S$

$$J_p(x) = \sigma_p E(x) - \underbrace{q\left(n_p \frac{\mathrm{d}D_p}{\mathrm{d}T} + D_p \frac{\mathrm{d}n_p}{\mathrm{d}T}\right)}_{\sigma_p S_p} \frac{\mathrm{d}T}{\mathrm{d}x} \tag{1.17}$$

The sign of the Seebeck coefficient $S_i$ is defined to be positive, if the arising electrical field is parallel to the applied temperature gradient (see figure 1.7).

## 1.1.2. Peltier effect

The Peltier effect describes the heating or cooling of a junction between two conductors $\mathrm{A}$ and $\mathrm{B}$, if there is a flow of current through them. It is named after the French physicist J. C. A. Peltier who discovered the effect in 1834 [Pel34]. The amount of produced heat per unit time $\dot{Q}$ depends on the Peltier coefficients $\Pi_A$ and $\Pi_B$ of the respective conductors and can be expressed by

$$\dot{Q} = (\Pi_A - \Pi_B)\, I \tag{1.18}$$

A negative sign in $\dot{Q}$ symbolizes the cooling of the junction, a positive value stands for a temperature increase. Considering equation 1.18, it is obvious that not only the Peltier coefficients but also the direction of the current is responsible for either cooling or heating, which makes the Peltier effect reversible. The Peltier coefficient $\Pi$ is related to the Seebeck coefficient $S$ through equation (1.19).

$$\Pi = ST \tag{1.19}$$

The Peltier effect can be visualized using figure 1.8 and the following description. Considering the junctions between the n-type material and the metal, an external voltage leads to a current flow from left to right through the setup (electrons move from the right to the left side). The electrons have to move through the metal on the right side into the semiconductor. In order for this to happen, the energy difference $\Delta E$ between the electron energy in the metal above the Fermi energy and the energy of the conduction band $E_C$ is needed. On average, the probability for this crossover is
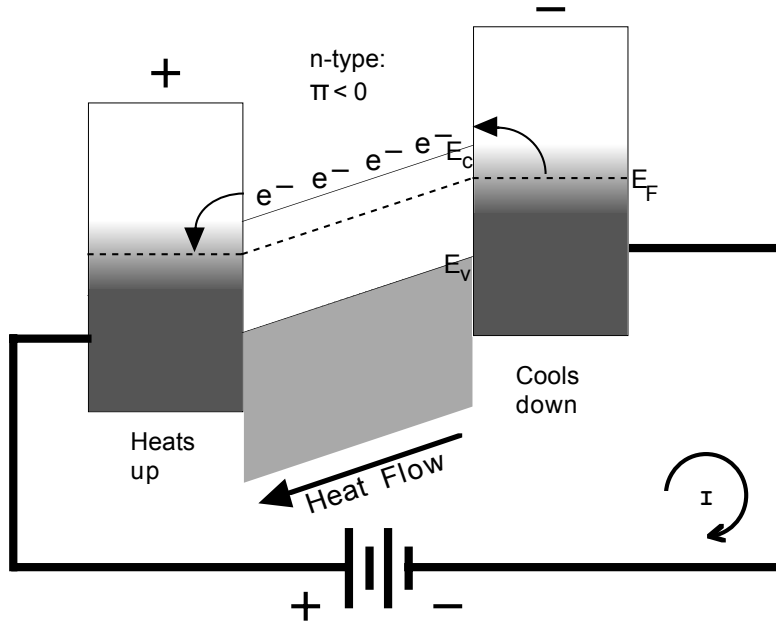
**Figure 1.8.:** Illustration of the Peltier effect, taken from [WEL96]

higher for electrons having higher energies than for electrons with lower energies. For that reason, the right hand side in figure 1.8 is depleted of high energy electrons and is subsequently cooled down. After the electrons have passed the semiconductor, they reenter the metal on the left side. Here, no energy barrier has to be overcome, so the amount of high energy electrons rises. This means that heat is transported effectively from the right to the left side, the electrical current $I$ causes a temperature difference $\Delta T$ at the junctions.

### 1.1.3. Thomson effect

For the sake of completeness the third thermoelectric effect, namely the Thomson effect, is mentioned. The Thomson effect is based on the fact, that the Seebeck coefficient is usually temperature-dependent. This means, that a temperature difference $\Delta T$ across the material leads to a local change in the Seebeck coefficient. If current flows in a material, which is superimposed by a temperature gradient, a continuous heat emission or absorption along the material is found. This effect has been predicted by W. Thomson (Lord Kelvin) and verified in 1851. The thermal output can be described using the current density $\vec{J}$ in a homogeneous conductor with a temperature gradient $\nabla T$ and the Thomson coefficient $\mathcal{K}$.

$$P = -\mathcal{K}\vec{J}\nabla T \tag{1.20}$$

It has to be kept in mind, that effects like Joule heating and regular thermal conductivity are not taken into account for this consideration. These effects superimpose the Thomson effect, which makes the measurement of the latter a laborious task. The Thomson coefficient relates to the temperature derivative of the Seebeck coefficient $\frac{dS}{dT}$ by equation (1.21).

$$\mathcal{K} = T\frac{dS}{dT} \tag{1.21}$$

Because the Thomson effect usually gives a small contribution and is only important for high temperature differences, it is often neglected for all practical purposes. However, for thermoelectric materials operating at high temperatures, it is important to take it into consideration.

## 1.2. Derivation of the figure of merit *ZT*
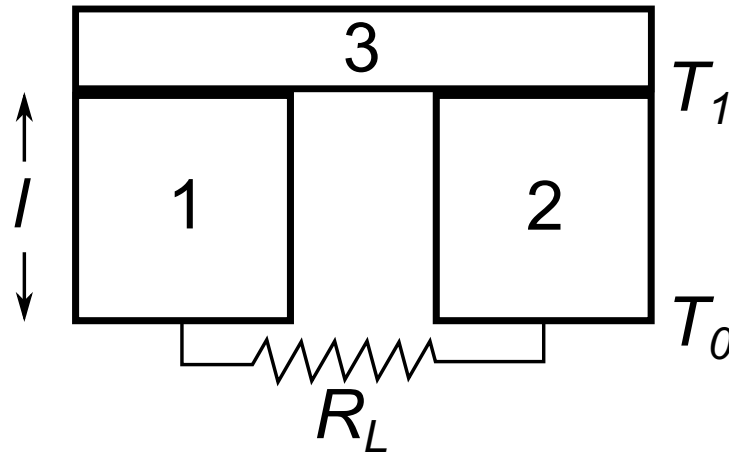


**Figure 1.9.:** Illustration of a thermoelectric generator

The figure of merit $ZT$ of a thermoelectric material is a measure for its efficiency $\eta$ and serves as a tool to assess the capability of the respective systems. It can be obtained as a quantity in the ratio of output power $P$ to input of heat energy $Q$. For its derivation after [Nic08], the simple illustration of a thermoelectric generator in figure 1.9 can be considered. The thermoelectric device consists of a p-type leg (1), an n-type leg (2) and a connecting metal strip (3). An external resistance $R_L$ is applied to the cold end sides of the legs at $T_0$. The Seebeck coefficient $S_d$ of the device can be expressed by the individual coefficients of the respective p- and n-type legs $S_p$ and $S_n$ by

$$S_d = S_p - S_n = |S_p| + |S_n| \tag{1.22}$$

The hot ends, which are joined by the metallic contact, are connected to the heat source at a temperature $T_1$. If the internal resistances of the legs are called $R_1$ and $R_2$ and their thermal conductances are denoted by $K_1$ and $K_2$, the total resistance and conductance of the device can be expressed by

$$R = R_1 + R_2 = \left( \frac{\rho_1}{A_1} + \frac{\rho_2}{A_2} \right) l \tag{1.23}$$

and

$$K = K_1 + K_2 = (\kappa_1 A_1 + \kappa_2 A_2) \frac{1}{l} \tag{1.24}$$

with the length $l$ of the thermoelectric legs and their respective cross sections $A_1$ and $A_2$. The efficiency of the device can be estimated, if the effects of generated and absorbed Peltier heating at the two junctions of the material, the heat conduction from the hot to the cold end and Joule heat generated by the current are considered and compared to the useful electrical energy received from the thermoelements. The Thomson heat generated and absorbed inside the materials is neglected in this consideration, which can be done if the Seebeck coefficient $S$ is considered to be temperature-independent. Starting with the Peltier heating, the amount of heat energy $Q_{T_1}$ received by the hot side of both thermoelements can be denoted by

$$Q_{T_1} = S_d I T_1 \tag{1.25}$$

The amount of heat $Q_h$ which is transported from the hot to the cold side of the device can be expressed by

$$Q_h = K(T_1 - T_0) \tag{1.26}$$

The Joule heat $Q_J$, which is generated in the materials, can be written as

$$Q_J = I^2 R \tag{1.27}$$

The useful power $P$ delivered from the two thermoelements can be expressed by

$$P = I^2 R_L \tag{1.28}$$

with a current $I = \frac{S_d(T_1 - T_0)}{R_L + R}$. By writing $m = \frac{R_L}{R}$, and inserting the expression for the current in equation 1.25, $Q_{T_1}$ can be expressed by

$$Q_{T_1} = S_d^2 T_1 (T_1 - T_0) \frac{1}{R(m+1)} \tag{1.29}$$

Eliminating the current $I$ in equation 1.28 yields

$$P = S_d^2(T_1 - T_0)^2 \frac{m}{R(m+1)^2} \tag{1.30}$$

Because half of the total Joule heat generated is passed to the hot junction, this returns an amount of $\frac{1}{2}I^2R$ to the heat source. This has to be accounted for in the expression for the efficiency $\eta$. This quantity will now be defined as the ratio of useful energy which is delivered to the external circuit to the energy consumed or received from the heat source. The full expression reads

$$\eta = \frac{P}{Q_{T_1} + Q_h - \frac{1}{2}I^2R} \tag{1.31}$$

$$= \frac{S_d^2(T_1 - T_0)^2 \frac{1}{R}\frac{m}{(m+1)^2}}{S_d^2 T_1(T_1 - T_0)\frac{1}{R}\frac{1}{(m+1)} + K(T_1 - T_0) - \frac{1}{2}\frac{S_d^2(T_1-T_0)^2}{R(m+1)^2}} \tag{1.32}$$

$$= \frac{T_1 - T_0}{T_1} \frac{\frac{m}{m+1}}{1 + \frac{KR}{S_d^2}\frac{m+1}{T_1} - \frac{1}{2}\frac{(T_1-T_0)}{T_1}\frac{1}{m+1}} \tag{1.33}$$

This expression shows, that the efficiency of a thermoelectric device essentially depends on three quantities. First of all, the hot and cold side temperatures $T_1$ and $T_0$ have to be chosen in a way, that a high temperature difference $\Delta T$ across the material can be achieved. Furthermore, the ratio of load resistance to internal resistance $m = \frac{R_L}{R}$ is responsible, for the device performance. A maximum output power can be obtained at $m = 1$, however, the maximum efficiency $\eta_{\max}$ is reached at $m = \sqrt{1 + \frac{1}{2}Z(T_1 + T_0)}$ which can be seen by setting $\frac{\partial \eta}{\partial m}$ to zero and solving for $m$. With this, the efficiency reads

$$\eta_{\max} = \frac{T_1 - T_0}{T_1} \frac{\sqrt{1 + ZT_m} - 1}{\sqrt{1 + ZT_m} + \frac{T_0}{T_1}} \tag{1.34}$$

with $T_m = \frac{T_1 + T_0}{2}$. The material dependence of expression 1.33 and 1.34 is found in the quantity $\frac{KR}{S_d^2} = Z^{-1}$, which has to be minimized in order to obtain high efficiencies. Assuming $S_n = S_p$ as well as $\rho_1 = \rho_2$ and $\kappa_1 = \kappa_2$ while keeping the cross section the same, $ZT$ can be expressed as

$$ZT = \frac{S_d^2}{KR}T = \frac{S^2}{\kappa\rho}T \tag{1.35}$$

The $ZT$ value is a dimensionless quantity that shows a strong dependence on material parameters but a high operating temperature $T$ will also increase its value, regardless of the material-dependent properties.
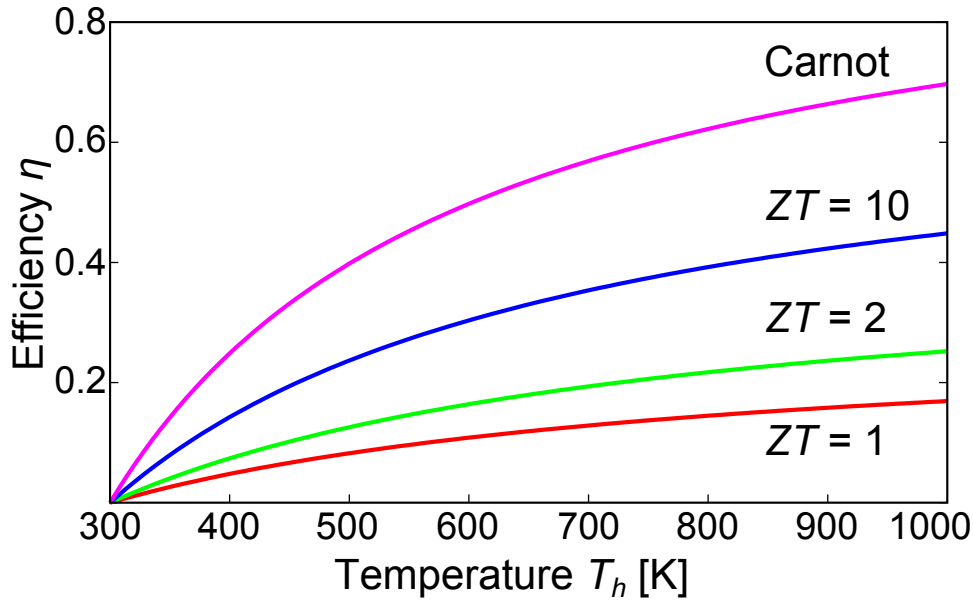
**Figure 1.10.:** Conversion efficiency $\eta$ for different values of $ZT$

## 1.3. Efficiency of thermoelectric materials

As it can be expected from the derived expression for the figure of merit in the previous section, the increase of the efficiency of thermoelectric materials is usually connected to the increase of the value of $ZT$. In general, a higher value of $ZT$ means a more suitable material for thermoelectric purposes. Since the discovery of thermoelectric materials, a majority of research focused on finding ways to increase this value. Just by looking at equation 1.35 it is obvious that an increase in $ZT$ can be achieved by increasing the Seebeck coefficient $S$ and the electrical conductivity $\sigma$ while decreasing the thermal conductivity $\kappa$. Because these quantities are difficult to modify individually and depend on microstructure, electronic band structure and charge carrier mobility, this cannot always be realized. Figure 1.10 shows a visualization of the efficiency derived in equation 1.34. In theory, only the Carnot process limits the thermoelectric efficiency. For a fixed cold side temperature $T_c = 300\,\mathrm{K}$, the efficiency $\eta$ depending on the hot side temperature $T_h$ is plotted for different values of $ZT$. $ZT$ values of state of the art materials with the best performance are in the range of $ZT = 1$-$2$ [Chu10].

### 1.3.1. Material classes

If the material properties decide on whether a certain material is suitable for thermoelectric purposes, it is only logical to review different material classes under this aspect. Metals exhibit a high electrical conductivity $\sigma$ but their low thermopower $S$
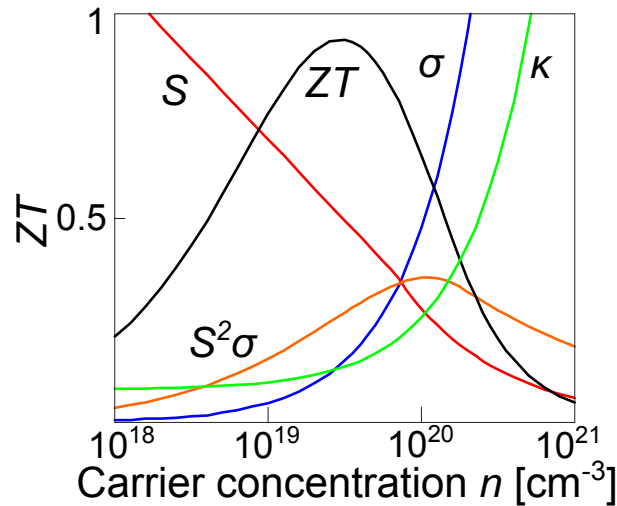
**Figure 1.11.:** Carrier concentration dependency of TE properties, redrawn from [ST08]

combined with their high thermal conductivity $\kappa$ lead to a poor value of $ZT$. Insulators are also no appropriate thermoelectric materials, since they have a high Seebeck coefficient but their electrical conductivity is so low, that their $ZT$ values are usually even below the value of metals [Woo88]. Optimized thermoelectric properties have to be balanced between a sufficiently high Seebeck coefficient and a fairly good electrical conductivity while keeping the thermal conductivity at a minimum at the same time. These requirements are only met by doped, semiconducting materials. Figure 1.11 shows the slopes of characteristic thermoelectric properties for a semiconductor with a fixed energy gap with the parabolic bands approximation. In order to maximize the figure of merit $ZT$, the charge carrier concentration has to be in the range of $n = 10^{19}$ - $10^{20}\,\mathrm{cm}^{-3}$. Because the Seebeck coefficient and the electrical conductivity are both quantities, which are determined by the electronic band structure of the material, it is important to understand how the band structure should look like for an optimized $S$ and $\sigma$.

### 1.3.2. Band structure for optimized *ZT* value

The electronic band structure of thermoelectric materials plays a crucial role in the optimization of the parameters to reach a high efficiency. In 1996, G. D. Mahan and J. O. Sofo published a study that focused on the $ZT$ optimization from a mathematical point of view [MS96]. They investigated under which assumptions and requirements to the electronic structure of the material a maximized efficiency can be reached. For this, some basic expressions have to be defined.

The thermoelectric parameters can be obtained as solutions of the Boltzmann transport equation as

$$\sigma = e^2 \int\limits_{-\infty}^{\infty} dE \left( -\frac{\partial f_0}{\partial E} \right) \Sigma(E) \tag{1.36}$$

$$T\sigma S = e \int\limits_{-\infty}^{\infty} dE \left( -\frac{\partial f_0}{\partial E} \right) \Sigma(E)(E - \mu) \tag{1.37}$$

$$T\kappa_0 = \int\limits_{-\infty}^{\infty} dE \left( -\frac{\partial f_0}{\partial E} \right) \Sigma(E)(E - \mu)^2 \tag{1.38}$$

with the chemical potential $\mu$ and the Fermi distribution $f_0$. $\Sigma(E)$ is the so called transport distribution function and is given by

$$\Sigma(E) = N(E)v_x(E)^2 \tau(E) \tag{1.39}$$

under the assumption of parabolic bands. Here, $N(E)$ is the density of states, $v_x(E)$ denotes the group velocity of the carriers in the direction of the applied field, $\tau(E)$ the relaxation time and $E$ the energy. Furthermore, the electronic thermal conductivity in the absence of any electrochemical potential gradient $\kappa_0$ is related to the thermal conductivity under zero electrical current $\kappa_e$ by

$$\kappa_0 = \kappa_e + T\sigma S^2 \tag{1.40}$$

In this, $\kappa_e$ can be interpreted as a purely conductive contribution while $\kappa_0$ also contains convection effects. By rearranging the thermoelectric expressions, they can be written as

$$\sigma = \sigma_0 I_0 \tag{1.41}$$

$$\sigma S = \left( \frac{k_B}{e} \right) \sigma_0 I_1 \tag{1.42}$$

$$\kappa_0 = \left( \frac{k_B}{e} \right)^2 T\sigma_0 I_2 \tag{1.43}$$

with $\sigma_0 = e^2/\hbar a_0$ where $\hbar$ is the reduced Planck constant and $a_0$ the Bohr radius. Furthermore, the dimensionless integrals $I_n$ have been used which read

$$I_n = \int\limits_{-\infty}^{\infty} dx \frac{e^x}{(e^x + 1)^2} s(x) x^n \tag{1.44}$$

where $s(x) = \hbar a_0 \sum (\mu + x k_B T)$ as the dimensionless transport distribution function is used. With this, $ZT$ takes a simple form of

$$ZT = \frac{\xi}{1 - \xi + A} \tag{1.45}$$

with $\xi = \frac{I_1^2}{I_0 I_2}$ and $A = \frac{1}{\alpha I_2}$, where $\alpha = (k_B/e)^2 T \sigma_0 / \kappa_l$. In order to maximize $ZT$, one can see that

$$ZT = \frac{\xi}{1 - \xi + A} \leq \frac{1}{A} = \frac{\kappa_0}{\kappa_l} \tag{1.46}$$

Since the value is obviously bounded by $\frac{\kappa_0}{\kappa_l}$ ($\kappa_l$ = lattice contribution to the thermal conductivity) in this consideration, a transport distribution function to fulfill $\xi = 1$ has to be found, in order to guarantee this upper limit. In the reference it was found, that the Dirac function is the only distribution which serves this purpose. If this transport distribution has the form of $s(x) = C\delta(x - b)$ ($C$ being a constant and $b$ indicating the peak position with respect to the Fermi level), the integrals in equation 1.41-1.43 can easily be calculated and a $ZT$ of

$$ZT_{\max} = 0.439 \left(\frac{k_B}{e}\right)^2 \frac{\sigma_0 T C}{\kappa_l} \tag{1.47}$$

can be obtained. With this, it could be shown, that a maximum of the $ZT$ value occurs, if the density of states approaches the shape of a delta function. In real materials, the electronic structure in the region around the conduction band will never follow an ideal delta shape. However, for electronic f-levels, which contribute to a rather sharp Lorentz peak in the density of states, this is an acceptable approximation. Adding constant terms in $N(E)$ (about $10\%$ background intensity), to account for a more realistic case, led to a reduction of a possible $ZT$ of around $25\%$. Even though the results of G. D. Mahan and J. O. Sofo are somehow abstract, they give insights which electronic structure is desirable. According to their results, a narrow distribution of the electronic states near the chemical potential, combined with a high charge carrier velocity as well as a small residual distribution in the density of states is the target for highly efficient thermoelectric materials.

### 1.3.3. Thoughts on the strong correlation

As it has been shown and discussed before, the transport parameters of conventional thermoelectric materials like $Bi_2Te_3$ or PbTe can be described approximately by Boltzmann transport mechanisms. However, the class of transition metal oxides,
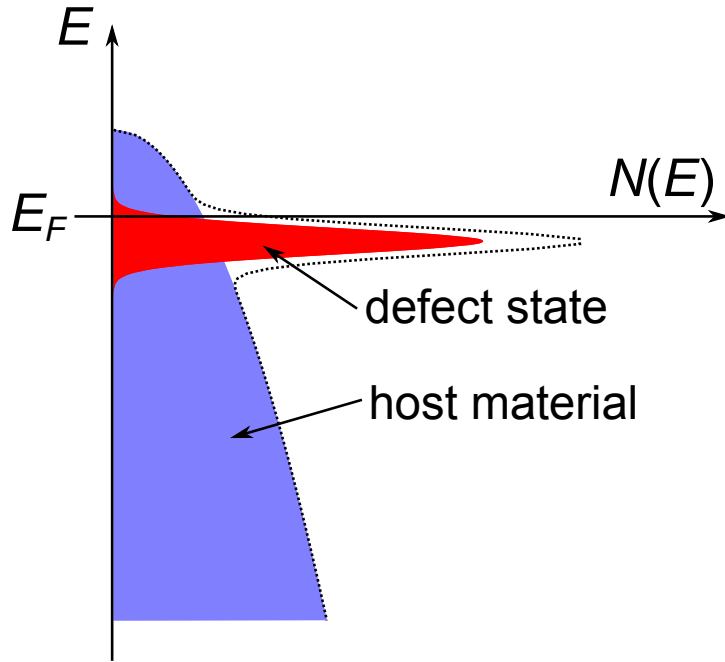
**Figure 1.12.:** Illustration of the density of states *N(E)* for good TE materials

which show a stronger correlation of the electrons, is insufficiently described by the Boltzmann formalism. Those materials are characterized by narrow bands, localized charge carriers and a hopping mechanism of the conductivity. R. Kubo realized that a more rigid and general formalism would be necessary to describe the processes in such materials [Kub57]. This treatment is rather complex and extensive, so only the approximation for large temperatures should be mentioned, as it was suggested by P. M. Chaikin and G. Beni [CB76]. In order to describe the behavior of electrons on a rigid lattice, the so called Hubbard model suggests a Hamiltonian of the following form

$$H = -t \sum_{\langle i,j \rangle, \sigma} \left( c_{i,\sigma}^{\dagger} c_{j,\sigma} + c_{j,\sigma}^{\dagger} c_{i,\sigma} \right) + U \sum_{i} c_{i\uparrow}^{\dagger} c_{i\uparrow} c_{i\downarrow}^{\dagger} c_{i\downarrow} \qquad (1.48)$$

Furthermore, Coulomb forces are only considered for electrons with spin $\uparrow$ and $\downarrow$ that occupy the same spot in this approximation. The kinetic part of the energy is expressed by the transfer integral $t$, which describes the overlap of the wave functions between neighboring sites. The sum runs only over neighboring sites $i$, $j$ and their spin direction $\sigma$. The fermionic creation and annihilation operators $c_{i,\sigma}^{\dagger}$ and $c_{i,\sigma}$ refer to an electron with spin $\sigma$ at site $i$. Under the given approximations, the Hubbard model describes the interaction between the kinetic energy, Coulomb repulsion and Pauli principle and can be applied to strongly correlated systems or band magnetism. For high temperatures ($t \ll k_B T$) the Seebeck coefficient of systems, whose Hamiltonian

is based on 1.48, can be expressed by

$$S = -\frac{k_B}{e} \frac{\partial \ln g}{\partial N} \tag{1.49}$$

where $g$ determines the degeneracy of the states, which is obtained from the system with its $N_A$ sites and $N$ charge carriers. In this high temperature approximation, the calculation of the Seebeck coefficient reduces to solving a simple combinatorial problem. This reads: How many possibilities $g$ exist to distribute $N$ charge carriers onto $N_A$ available sites. Considering a one-dimensional fermionic system ($N_{\uparrow(\downarrow)}$ = number of charge carriers with spin up (down)), which does not show any interaction among the charge carriers ($k_B T \gg U$), the degeneracy can be expressed as

$$g = \sum_{N_\uparrow = 0}^{N} \left( \frac{N_A!}{N_\uparrow!(N_A - N_\uparrow)!} \frac{N_A!}{N_\downarrow!(N_A - N_\downarrow)!} \right) \tag{1.50}$$

with $N = N_\uparrow + N_\downarrow$ and $N < N_A$. Using Stirling's approximation, the Seebeck coefficient $S$ now reads

$$S = -\frac{k_B}{e} \ln \left( \frac{2 - n}{n} \right) \tag{1.51}$$

Here, $n$ stands for the local charge density (which is the ratio of charge carriers $N$ to available sites $N_A$). For strongly correlated systems it is important to keep in mind, that two charge carriers cannot occupy the same site due to the strong repulsion ($k_B T \ll U$). For this case, the equation yields

$$g = \frac{2^N N_A!}{N!(N_A - N)!} \tag{1.52}$$

and the thermopower reads

$$S = -\frac{k_B}{e} \ln \left( \frac{2(1 - n)}{n} \right) \tag{1.53}$$

This expression was further generalized for cobaltate materials by W. Koshibae [KTM00], because both degeneracies $g_i$ (for different valencies $Co^{i+}$) as well as the occupied sites $M$ of the $Co^{4+}$ ions influence the resulting Seebeck coefficient. The total degeneracy $g$ and the Seebeck coefficient $S$ can be expressed by using equation 1.54 and 1.55 with

$$g = g_3^{N_A - M} g_4^M \frac{N_A!}{M!(N_A - M)!} \tag{1.54}$$

and

$$S = -\frac{k_B}{e} \ln\left(\frac{g_3}{g_4}\frac{x}{1-x}\right) \tag{1.55}$$

where $x = \frac{M}{N_A}$ denotes the concentration of $Co^{4+}$ ions. It can be deduced from expression 1.55, that the Seebeck coefficient of cobaltates is mainly determined by the ratio of the degeneracies as well as the ratio of the valences [KM01]. This additional contribution to the thermopower explains the comparably high Seebeck coefficient for these kinds of materials, besides showing metal-like conductivity. The possibility of tuning $S$ via the ratio of the valence states without significantly influencing the electrical conductivity is a key component for the success which the cobaltates had as thermoelectric materials since the late 1990s.

### 1.3.4. Phonon influence on the thermoelectric efficiency

Up until now, the electronic properties have been discussed. Taking $ZT$ from equation 1.35 into account, it can be understood, that a low thermal conductivity is favorable if a preferable high thermoelectric efficiency is to be achieved. The classic kinetic theory of gases gives an expression (equation 1.56) for the thermal conductivity of solids $\kappa$.

$$\kappa = \frac{1}{3}c_v\overline{v_p}^2\overline{\tau} = \frac{1}{3}c_v\overline{v_p}\overline{\Lambda} \tag{1.56}$$

In this expression, $c_v$ denotes the specific heat at constant volume, $\overline{v_p}$ the mean phonon velocity, $\overline{\tau}$ the scattering time (time between two scattering events) and $\overline{\Lambda}$ the mean free path. Strictly speaking, the phonon velocity $c_v$ is given by the dispersion relation between frequency $\omega$ and wave vector of the individual phonons, which is why $\kappa$ is actually described by the sum over every phonon mode. However, for this sum the approximation using the mean expressions in equation 1.56 has been used. At low temperatures ($T < 10\,\mathrm{K}$), the thermal conductivity is mainly influenced by the contributions from the specific heat $c_v$ and shows a $T^3$ behavior, while the mean free path $\Lambda$, which is dependent on the phonon scattering, is nearly constant. At high temperatures, the value of the the specific heat approaches the classical value of $3R$ and the mean free path decreases with $1/T$. The mean phonon velocity $v_p$ can be assumed to be temperature-independent [Woo88]. This explanation may be sufficient for a general picture but lacks the depth to explain more complex scattering processes in the material. To do that, the different contributions to the relaxation time $\tau$ have to be taken into account.

$$\tau^{-1} = \tau_p^{-1} + \tau_D^{-1} + \tau_B^{-1} + \tau_{\mathrm{e-ph}}^{-1} \tag{1.57}$$
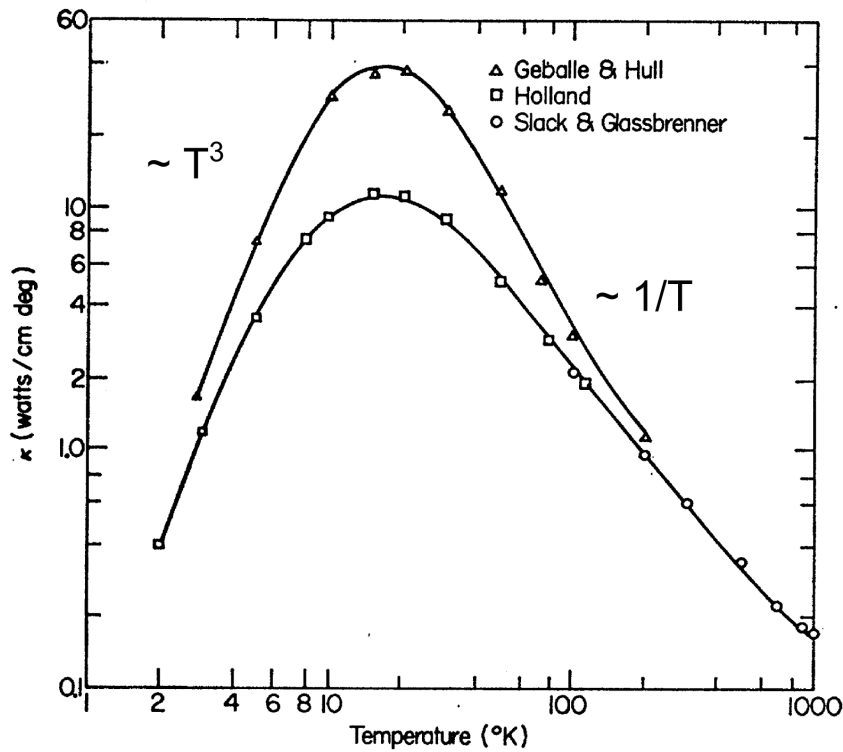
**Figure 1.13.:** Thermal conductivity of germanium, taken from [Hol63], □: normal Ge, △: single isotope Ge

Here, $\tau_p$ characterizes the relaxation time for phonon-phonon scattering (Normal and Umklapp, $\tau_p^{-1} \propto \omega^2$), $\tau_D$ represents the defect scattering in the crystal ($\tau_D^{-1} \propto \omega^4$) and $\tau_B$ (independent of frequency, $\tau_B^{-1} \propto \omega^0$) the phonon-grain boundary scattering [CvB60]. $\tau_{e-ph}^{-1}$ which has a linear to square dependence on $\omega$ denotes the phonon-electron scattering [SA64]. It is easy to see, that the relaxation time $\tau$ has a strong inverse dependence on the phonon frequency $\omega$. Phonons with smaller wavelengths are preferably scattered on defects, while electron scattering dominates the low frequency phonons. Considering the 4th power of the frequency dependence of the inverse scattering time on defects, it is clear, that the overall contribution of high frequency phonons to the thermal conductivity $\kappa$ is small and therefore, mostly phonons with long wavelengths are responsible for the heat transport [SA64]. These phonons have to be minimized, in order to enhance the material's efficiency.

The temperature $T$ has a similar influence as the phonon frequency $\omega$ on the dominating scattering process. At low temperatures, phonon-phonon scattering is relatively weak and the dominating processes are phonon-boundary and phonon-electron scattering. With increasing temperature and rising number of phonon modes, phonon-phonon scattering gains more importance over the other processes. Over a large

21

temperature range, phonon-defect scattering plays an important role and can be adjusted by doping with impurities (atoms or vacancies) in order to reduce the mean free path and subsequently the thermal conductivity.

### 1.3.5. Electrical conductivity

As mentioned in chapter 1.3, the thermoelectric parameters in bulk materials can usually not be modified independently. This can easily be seen by studying the expressions for these properties. For metals and heavily doped semiconductors, the Seebeck coefficient $S$ can be expressed using the approximation of parabolic bands and an energy independent scattering as

$$S = \frac{8\pi^2 k_B^2}{3eh^2} m^\star T \left(\frac{\pi}{3n}\right)^{3/2} \tag{1.58}$$

In this, $m^\star$ represents the effective mass and $n$ stands for the charge carrier concentration. The electrical conductivity $\sigma$ has a linear dependence on the charge carrier concentration as

$$\sigma = n\, e\, \mu \tag{1.59}$$

A high charge carrier density is favored for the electrical conductivity but decreases the Seebeck coefficient. This mutual influence can also be observed indirectly via the effective mass. As described in subsection 1.3.2, a flat band structure with a sharp increase near the Fermi energy is important to receive good thermoelectric properties. Because this leads to a high effective mass, the Seebeck coefficient benefits from this which can be seen by equation 1.58. A heavy effective mass however, hinders the charge carrier mobility and therefore the electrical conductivity. A similar reverse dependence can also be found between the electrical conductivity $\sigma$ and the electrical contribution to the thermal conductivity $\kappa_e$. The Wiedemann-Franz law reads

$$\frac{\kappa_e}{\sigma} = LT \tag{1.60}$$

with $L = \frac{\pi^2 k_B^2}{3e^2}$ and shows that these quantities are connected such that a high electrical conductivity leads inevitably to a high thermal conductivity [ST08].

### 1.3.6. Influence of dimensionality

Until the early 1990s, a vast majority of research done in the field of thermoelectricity focused on bulk materials and on ways to improve the efficiency of those. The classic

approach to enhance the $ZT$ value was to increase the power factor or decrease the thermal conductivity. In order to achieve the latter, the usage of materials containing heavy elements like Bi or Pb is favored, because they lead to low sound velocities and therefore low thermal conductivities of the materials. Furthermore, materials with complex crystal structures, where the atoms do not occupy well-defined positions can scatter phonons effectively. An enhancement of the power factor can be achieved, if additional energy levels in the density of states near the Fermi level are introduced via doping. By doping, the density of states is locally increased which leads to an increase of the effective mass which is proportional to the Seebeck coefficient $S$ according to equation 1.58. By selective doping, the power factor can be increased without a strong deterioration of the charge carrier mobility. A modern approach towards the enhancement of the efficiency is the so called PGEC (Phonon Glass Electron Crystal) concept introduced by G. A. Slack [Sla95]. For this, materials are chosen which show a high electrical conductivity due to their optimized periodicity of the lattice structure, while at the same time retaining a low thermal conductivity due to the complex structural properties of the lattice. Those approaches focus on the structural changes of the materials, so it is obvious to also investigate the dimensional influence on the $ZT$ value. For that, M. Dresselhaus started to give a new perspective to scientists, concerning the approach to the topic of enhancing the efficiency in 1993. Her work in [HD93a] and [HD93b] dealt with electronic states in confined systems and the impact of those on thermoelectric systems. This approach demonstrated the enhancement of the power factor by increasing the density of states near the Fermi level by quantum confinement rather than external doping. This can be achieved, if the size of the material is tailored to be comparable to the spatial extent of the electronic wave functions. Assuming an energy independent scattering (charge carrier mobility $\mu(E) = \mu$), the electrical conductivity is proportional to the density of states. The Mott-Jones relation (valid for metals and heavily doped semiconductors) shows that the power factor increases with increasing change in slope of the density of states.

$$S = \frac{\pi^2}{3} \frac{k_B^2 T}{e} \left( \frac{\partial \log \sigma(E)}{\partial E} \right)_{E=E_F} \tag{1.61}$$

Because the density of states in low-dimensional systems changes and shows nearly dispersion-less bands (see figure 1.14), a specific placement of those bands by nanostructuring can lead to a strong increase of the power factor. Based on this, both publications by Dresselhaus showed that the $ZT$ value could be drastically improved by enhancing the density of states near the band edges by electron confinement. In the work a general expression for $ZT$ with the dependence on dimensionality $N$ is
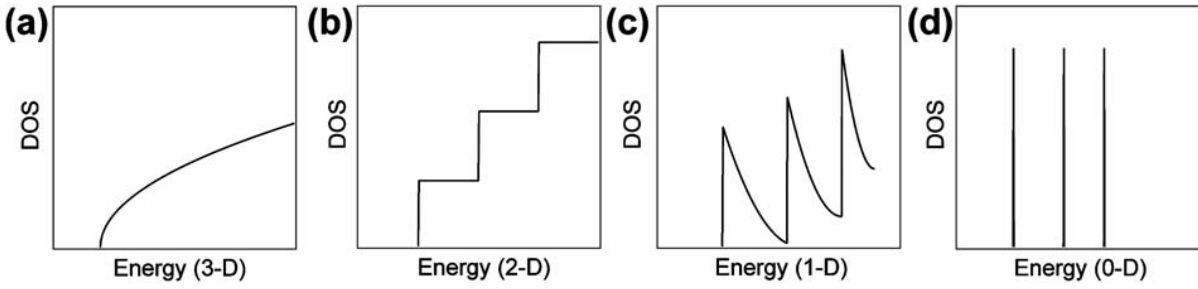
**Figure 1.14.:** Dimensionality influence on the density of states, taken from [SHJ11]

given. For a one-band material (e.g. heavily doped semiconductor, with the majority of charge transport in the conduction band) with constant relaxation time $\tau$ and the assumption of parabolic bands, the figure of merit can be expressed by

$$
ZT_N = \frac{\frac{N}{2}\left(\alpha_N \frac{F_{\frac{N}{2}}}{F_{\frac{N}{2}-1}} - \eta\right)^2 F_{\frac{N}{2}-1}}{\frac{1}{B} + \left(\frac{N+4}{2}\right) F_{\frac{N}{2}+1} - \beta_N \frac{F_{\frac{N}{2}}^2}{F_{\frac{N}{2}-1}}}
\tag{1.62}
$$

with $\alpha_N = \frac{N^2-6N+16}{3}$, $\beta_N = \frac{2N^2-9N+34}{6}$, $\eta = \frac{\mu}{k_B T}$ as the reduced chemical potential and $F_i(\eta) = \int \left(\frac{x^i \mathrm{d}x}{\exp(x-\eta)+1}\right)$. Using the mobility in the direction of $x$, $\mu_x$, the material dependence can be found in the parameter $B = \gamma_N \left(\frac{2k_B T}{\hbar^2}\right)^{\frac{N}{2}} \frac{k_B^2 T \mu_x}{e\kappa_l}$ with $\gamma_1 \propto \frac{1}{a^2}$, $\gamma_2 \propto \frac{1}{a}$, $\gamma_3 \propto a^0$ and quantum width $a$.

For $N = 3$ it is obvious, that the parameter $B$ is mainly characterized by intrinsic material properties, while the reduced chemical potential can be modified by doping, so that a maximum $ZT_{3D}$ can be achieved at a fixed value of $B$.

In order to increase $B$, the only possibility, in the case of $N = 3$, is to chose the current direction to be parallel to the direction of the highest mobility and to keep the thermal conductivity $\kappa$ as low as possible. For $N = 2$ however, the confinement leads to completely new possibilities to tune the parameter. In this case, $B$ can be increased by choosing the right direction of the current as well as by reducing the quantum width $a$ or choosing the right orientation of the planes. This effect is enhanced even more for one-dimensional structures, as the quantum width now has a square dependence on $B$. Another possibility how to use nanostructuring to enhance $ZT$ is the increase of interfaces and surfaces, to promote phonon scattering. Many experimental works could already prove, that this quantum well effect actually exists and can be used to increase the $ZT$ value (e.g. [OK07]).

# 2. Thermoelectric oxides
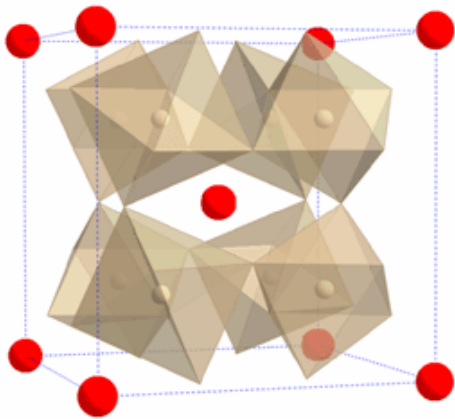


**Figure 2.1.:** Crystal structure of the skutterudite compound $EuFe_4Sb_{12}$ [KLH$^+$07]
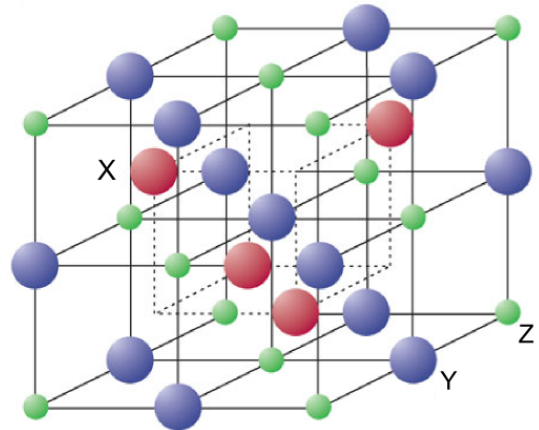


**Figure 2.2.:** Half-Heusler crystal structure, modified from [Fra10]

Probably the most well-known and frequently used thermoelectric materials originate from the group of the chalcogenides[1]. Out of those, especially $Bi_2Te_3$ is used for the low temperature regions (up to $T = 250\,°C$), whereas PbTe shows the best efficiency around $T = 500\,°C$ ($ZT = 0.8$) [ST08]. These materials have been known to represent good thermoelectric systems for a long time and new concepts like nanostructuring were able to improve their efficiency even further in the last years. The disadvantages of these materials are the scarcity of elements like tellurium and the bad environmental sustainability or toxicity of lead, antimony or selenium, which are used as dopants in these systems. Another important class of materials for thermoelectricity is the group of skutterudites (see figure 2.1). These feature a cubic structure with subsystems of $XY_6$ (X = Fe, Co, Rh, Ir and Y = P, As, Sb). Eight of these cubic cells share a corner so the connected octahedrons create a void in their middle. This void can be used as a site to dope several different atoms into. Often, these structures are described by the chemical formula $\square_2X_8Y_{24}$. The impurity atoms $\square$ in the center

---

[1]Chalcogenides describe compounds consisting of at least one chalcogen anion and an additional electropositive element. Even if all group 16 elements are chalcogens by definition, the term chalcogenide is mostly used for sulfides, selenides and tellurides, rather than oxides [GE84].

of the cell act as effective phonon scattering sites and lead to a reduction in thermal conductivity, so the $ZT$ values can reach up to $1.4$ at $T = 630\,°C$ [LTZU09]. Another known class of materials is described by the intermetallic Half-Heusler compounds. These consist of three fcc sublattices (see figure 2.2) and have the chemical formula of XYZ, where X, Y and Z can be chosen from a variety of elements (e.g. TiNiSn). The narrow electronic bands lead to a large effective mass, which is favorable for the Seebeck coefficient (as discussed before). The different sublattices in these systems can be doped independently, so that doping on the Sn site can modify the number of charge carriers, while adjusting the Ti and Ni site can lead to a reduction in thermal conductivity. There have been reports on $ZT$ values above unity. Usually, those materials are susceptible to oxidization at elevated temperatures, which is why measurements of their properties are usually carried out in an inert gas atmosphere [NPK06].

For the work presented in this thesis, oxide compounds have been chosen as the material class of interest. Thermoelectric oxides are materials, which are distinguished by their high-temperature stability and the fact that they are less susceptible to oxygen exchange. The compounds are usually non-toxic and are based on common transition metal elements. Well-known examples for oxide thermoelectrics are n-type $SrTiO_3$ [OOK06], ZnO [OAY09] and $CaMnO_3$ [FMF$^+$06]. For the p-type compounds, $Na_xCo_2O_4$ [TSU97], [FMN01], $Ca_3Co_4O_9$ [SF03] and $Bi_2Sr_2Co_2O_x$ [FMS00] can be mentioned. A table with values for the corresponding Seebeck coefficients, electrical and thermal conductivities and $ZT$ factors is shown below. The following section gives a short overview of the development of these materials, their transport mechanism and the influence of the Co valence on the Seebeck coefficient in p-type compounds.

| Property | $SrTiO_3$ | ZnO | $CaMnO_3$ | $Na_xCo_2O_4$ | $Ca_3Co_4O_9$ | $Bi_2Sr_2Co_2O_x$ |
|---|---|---|---|---|---|---|
| $S\ [\mathrm{\mu V\,K^{-1}}]$ | -175 | -240 | -150 | 200 | 240 | 150 |
| $\sigma\ [\mathrm{S\,cm^{-1}}]$ | 340 | 410 | 115 | 1925 | 435 | 80 |
| $\kappa\ [\mathrm{W\,m^{-1}\,K^{-1}}]$ | 3 | 4.8 | 1.6 | 5.1 | 3 | 0.9 |
| $ZT$ | 0.35 | 0.52 | 0.16 | 1.2 | 0.83 | 0.19 |
| $T\ [\mathrm{K}]$ | 1000 | 1073 | 973 | 800 | 973 | 973 |

**Table 2.1.:** Thermoelectric properties of selected oxide materials

## 2.1. History

Until the end of the 1990s, oxide materials did only play a subordinate role concerning thermoelectric compounds. The reason for that was, that most oxides show strong

ionic bonds where the small overlap of the electronic wave functions causes the electrons to be localized and to have low mobilities, therefore the electrical conductivity is much lower than in other materials. Additionally, the low effective atomic masses of the constituents lead to higher atomic vibrational frequencies as in comparable heavier compounds, thus resulting in a rather high thermal conductivity. Finally, their simple unit cell also leads to a lack of phonon scattering centers which also favors the propagation of heat. However, in 1994 first studies by M. Ohtaki on $In_2O_3$-$SnO_2$ alloys showed considerable thermoelectric properties and sparked the interest to further investigate this class of materials for these kinds of applications ($ZT = 0.04$ at $T = 1000\,\mathrm{K}$) [OOEA94]. I. Terasaki made a breakthrough discovery in 1997 on the $Na_xCo_2O_4$ system, where he could find near metallic electrical conductivity but at the same time a value of the Seebeck coefficient, which surpassed the expectations by a factor of $10$ (resulting in $ZT = 0.7$ - $0.8$ at $T = 1000\,\mathrm{K}$). A theory and reasoning for this could be found some time later and motivated by the success, several oxide compounds have been the subject of research concerning their applicability to thermoelectric materials after that.

## 2.2. The special role of the cobaltates

As mentioned in section 1.3.3, the large Seebeck coefficient of $NaCo_2O_4$ could not be explained with the models that existed up until then. In order to give a more detailed explanation of this, it is beneficial to study the structure of the cobaltates first, using $NaCo_2O_4$ as an example. In figure 2.3, the crystal structure of $NaCo_2O_4$ is shown, which crystallizes in the space group $P6_3/mmc$ and is made of planes of $CoO_2$ octahedrons, which are connected by their edges[2]. The planes are separated by lattice sites, which are partially (here half) filled by Na ions. Looking at the chemical formula, the mean valence of the Co ions can be identified to be $3.5$. Since partial valences do not make sense in a physical way, this means that on average half of the Co ions have the valence $Co^{4+}$ while the other half are in the $Co^{3+}$ state [RGN99]. Due to the octahedral crystal field from the surrounding oxygen orbitals, the 5d orbital of Co splits into two energy states, a triple degenerate orbital $t_{2g}$ with a lower energy and a double degenerate orbital $e_g$ with a higher energy [Sin00]. The Co ions distribute their electrons among those energy bands, where the total degeneracy $g = g_s \times g_o$ consists of the spin degeneracy $g_s = 2s+1$ and the orbital degeneracy $g_o$. For the low spin state, taken from figure 2.4, one can see that $Co^{3+}$ has a completely filled $t_{2g}$ band, which

---

[2]The $CoO_2$ plane is the same in many known cobaltates like $Ca_3Co_4O_9$ or $Bi_2Sr_2Co_2O_x$ and it is essentially the reason for the good thermoelectric properties of these compounds
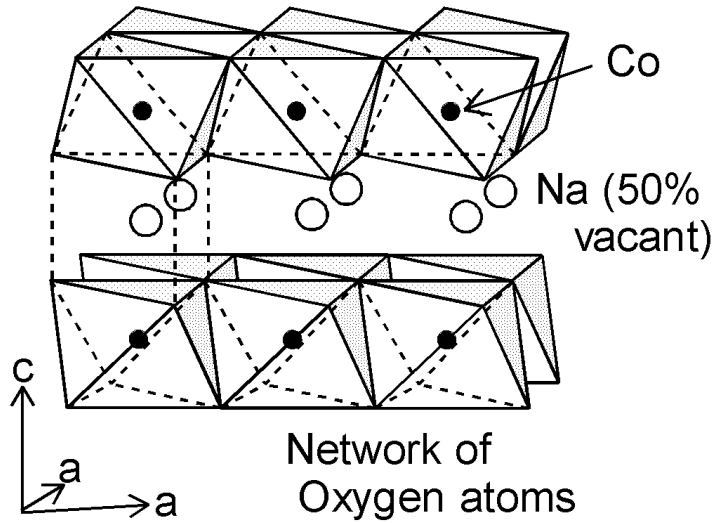
**Figure 2.3.:** Crystal structure of NaCo$_2$O$_4$, taken from [Ter03]
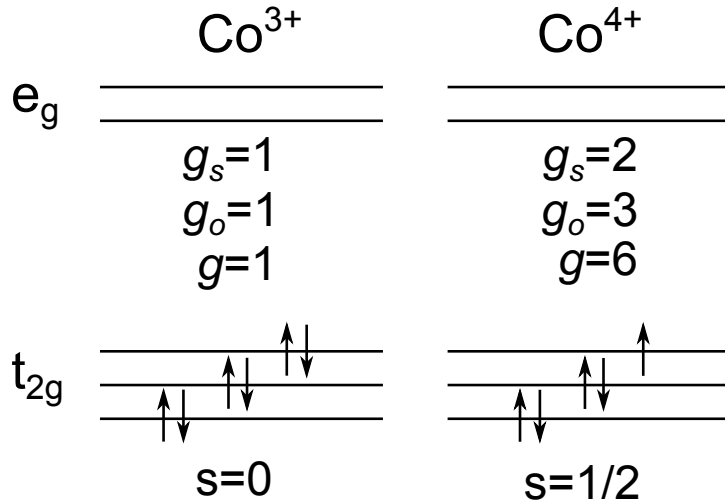


**Figure 2.4.:** Electronic degeneracy of Co$^{3+}$ and Co$^{4+}$ in the low spin state

results in a spin $s = 0$. Because there is only one distinguishable combination how the electrons can occupy the t$_{2g}$ band, the total degeneracy is $g = 1$. However, Co$^{4+}$ shows a different picture. The missing electron leads to a spin configuration of $s = \frac{1}{2}$, a triple degeneracy of the configuration in the t$_{2g}$ band and a hole for the hopping charge transport. Calculating from expression 1.55, the total degeneracy of $g = 6$ leads to a Seebeck coefficient at high temperatures of

$$S = -\frac{k_B}{e} \ln \left( \frac{1}{6} \frac{0.5}{1 - 0.5} \right) = 154 \, \mu\text{V K}^{-1} \tag{2.1}$$

This value still deviates about $20\,\%$ from the experimentally obtained Seebeck coefficients. This is due to the fact, that expression 2.1 assumes Co$^{3+}$ as well as Co$^{4+}$ to be

only in the low spin state. However, magnetic measurements suggest a transition of Co$^{4+}$ from the low spin into the high spin state at high temperatures [RGN99]. The possibility to be found in both states increases the total degeneracy of Co$^{4+}$, which leads to an increase in the factor of $g_{\text{Co}^{4+}}$ from 6 to 12. By taking this into account, the Seebeck coefficient calculated from equation 1.55 yields $S = 214\,\mu\text{V}\,\text{K}^{-1}$, which is less than $10\,\%$ off the experimental value of $S = 200\,\mu\text{V}\,\text{K}^{-1}$ (see table 2.1).

## 2.3. Defect chemistry and charge transport in Nb-doped SrTiO$_3$

Because a great part of this work deals with a glass-ceramic system with Nb-doped SrTiO$_3$ as a main crystal phase, it is beneficial to study the charge compensation and charge transport mechanism for this species of the group of perovskites. Due to SrTiO$_3$ being an insulator, its semiconducting property has to be obtained by doping with impurity ions. Commonly found dopants in this system are La doping on the Sr site as well as Nb doping on the Ti site. If, like in this work, Nb$^{5+}$ is substituted for Ti$^{4+}$ (Nb$_2$O$_5$ for 2 TiO$_2$), there has to be a way to compensate for the excess oxygen. According to [BHH$^+$08], this is done in Nb-doped SrTiO$_3$ by incorporating the oxygen into the lattice and the formation of cation vacancies in order to guarantee the electroneutrality. Using the Kröger-Vink notation[3], the stoichiometric ratio of Sr/Ti reads

$$\text{SrO} + (1-x)\text{TiO}_2 + \frac{x}{2}\text{Nb}_2\text{O}_5 \rightarrow \left(1 - \frac{x}{2}\right)\text{Sr}_{\text{Sr}}^{\text{x}} + \frac{x}{2}V_{\text{Sr}}'' + (1-x)\text{Ti}_{\text{Ti}}^{\text{x}} + x\text{Nb}_{\text{Ti}}^{\bullet} + 3\text{O}_{\text{O}}^{\text{x}} + \frac{x}{2}\text{SrO}$$
(2.2)
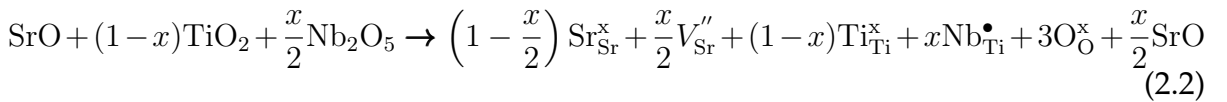
In this case, $\frac{x}{2}$ vacancies emerge on the Sr site, the excess of strontium and oxygen forms SrO as a secondary phase. If this has to be avoided, the starting composition has to be adjusted, so that a smaller amount of strontium is available for the reaction, which is shown in equation 2.3.

$$\left(1 - \frac{x}{2}\right)\text{SrO} + (1-x)\text{TiO}_2 + \frac{x}{2}\text{Nb}_2\text{O}_5 \rightarrow \left(1 - \frac{x}{2}\right)\text{Sr}_{\text{Sr}}^{\text{x}} + \frac{x}{2}V_{\text{Sr}}'' + (1-x)\text{Ti}_{\text{Ti}}^{\text{x}} + x\text{Nb}_{\text{Ti}}^{\bullet} + 3\text{O}_{\text{O}}^{\text{x}}$$
(2.3)
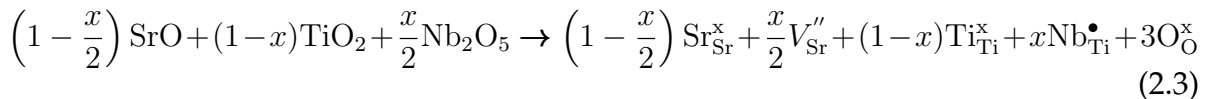
Both reactions describe the situation in an oxidizing atmosphere. Using reducing conditions, a certain amount of the secondary phase in equation 2.2 can be reduced so

---

[3]Convention to describe charges and impurities in crystal lattices, named after F. A. Kröger and H. J. Vink [KV56]. $M_S^C$ denotes the species $M$ (atoms, vacancies $V$, electrons e and holes h), the position within the lattice is described by $S$ and the electrical charge relative to the regular charge by $C$ ($\bullet$ denotes a positive, ' a negative charge and x stands for no relative change in charge)

that it reads

$$yV_{\text{Sr}}'' + y\text{SrO} \leftrightarrow y\text{Sr}_{\text{Sr}}^{\text{x}} + \frac{y}{2}\text{O}_2 + 2ye' \tag{2.4}$$
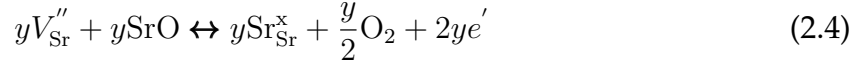
Using a reducing atmosphere changes the right hand side of expression 2.2 into

$$\left(1 - \frac{x}{2} + y\right)\text{Sr}_{\text{Sr}}^{\text{x}} + \left(\frac{x}{2} - y\right)V_{\text{Sr}}'' + (1 - x - 2y)\text{Ti}_{\text{Ti}}^{\text{x}} + 2y\text{Ti}_{\text{Ti}}' + x\text{Nb}_{\text{Ti}}^{\bullet} + 3\text{O}_{\text{O}}^{\text{x}} + \left(\frac{x}{2} - y\right)\text{SrO} \tag{2.5}$$
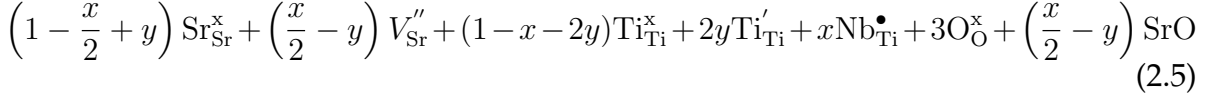
In theory, an ideal phase of $\text{SrTi}^{+\text{IV}}_{1-2x}\text{Ti}^{+\text{III}}_{x}\text{Nb}_{x}\text{O}_3$ at $y = \frac{x}{2}$ can be reached. The chemical equations assume an equilibrium state, which can be reached only in reducing atmosphere. Therefore, it is questionable, if a subsequent thermal treatment of the material from equation 2.2 under reducing conditions can really result in the long-range diffusion of cations or their respective vacancies. For the material from equation 2.3, reducing conditions lead to

$$yV_{\text{Sr}}'' + y\text{Ti}_{\text{Ti}}^{\text{x}} + 3y\text{O}_{\text{O}}^{\text{x}} \leftrightarrow \frac{y}{2}\text{O}_2 + 2ye' + y\text{TiO}_2 \tag{2.6}$$
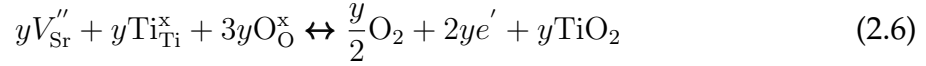
This changes the right hand side of equation 2.3 into

$$\left(1 - \frac{x}{2} + y\right)\text{Sr}_{\text{Sr}}^{\text{x}} + \left(\frac{x}{2} - y\right)V_{\text{Sr}}'' + (1 - x - 3y)\text{Ti}_{\text{Ti}}^{\text{x}} + 2y\text{Ti}_{\text{Ti}}' + x\text{Nb}_{\text{Ti}}^{\bullet} + (3 - 3y)\text{O}_{\text{O}}^{\text{x}} + y\text{TiO}_2 \tag{2.7}$$
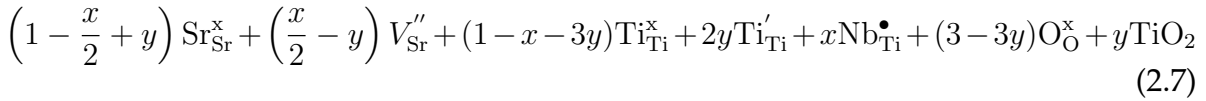
In this case, an additional Ti rich phase is formed. It is clear to see, that whether for the stoichiometric composition in equation 2.2 or the Sr reduced composition in 2.3, the charge compensation mechanism changes from Sr vacancies to an electronic compensation by $\text{Ti}^{3+}$ at low oxygen partial pressure $p_{\text{O}_2}$. This means, that the charge compensation as well as the conduction mechanism depend on the oxygen partial pressure in Nb-doped $\text{SrTiO}_3$. In a strongly reducing environment, the formation of oxygen vacancies is favored, so the charge carrier density $n$ does not only depend on the donor concentration $[\text{Nb}_{\text{Ti}}^{\bullet}]$ but also on the amount of oxygen vacancies $[V_{\text{O}}^{\bullet\bullet}]$.

$$n \approx 2[V_{\text{O}}^{\bullet\bullet}] + [\text{Nb}_{\text{Ti}}^{\bullet}] \tag{2.8}$$

In the intermediate region of $p_{\text{O}_2}$, the concentration of vacancies decreases, so the charge carrier concentration will only be dependent on the donor content.

$$n \approx [\text{Nb}_{\text{Ti}}^{\bullet}] \tag{2.9}$$

At high $p_{\text{O}_2}$, intrinsic acceptors compensate the donors, so the electroneutrality condition reads

$$[\text{Nb}_{\text{Ti}}^{\bullet}] \approx 2[V_{\text{Sr}}''] \tag{2.10}$$

# 3. Glass and glass-ceramics
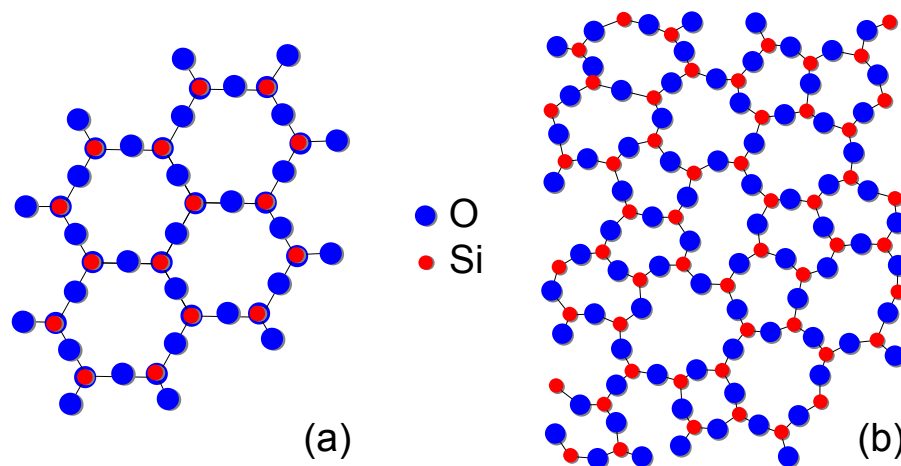


**Figure 3.1.:** Regular repeating crystal structure (a) vs. random glass network (b), redrawn from [Zac32]

Glasses, which emerged from melting and rapid cooling of rocks as a result of natural phenomena (volcanic eruptions, lightning strikes, meteorite impacts) have been around for long times. Phoenician merchants had the first unexpected contact with glass-like material in $5000\,\mathrm{BC}$, when they used nitrate blocks as cooktops and an opaque liquid formed due to the high temperatures and the sandy ground [Bou08]. The first glassy objects, which have been produced knowingly, date back to $3500\,\mathrm{BC}$ and since then, the development has progressed enormously. The Industrial Revolution brought the technologies for mass production and scientists like O. Schott started to do systematic research on the influence of chemical elements on the optical and thermal properties of glasses. This led to a deeper understanding of the physical relations and with the discovery of glass-ceramics by S. D. Stookey (1953, [Sto59]) and industrial achievements like the development of the float glass process (1959, [Pil69]), the production of glass has become a multi-million dollar business today.

# 3.1. Glass transition and structure

The glassy state and the associated glass transition are topics, which have been investigated and described for a long time. The books of W. Vogel [Vog92] and H. Scholze [Sch11] are standard references for the main aspects and basics of the glassy nature and are used for this short overview. Despite the different approaches and concepts to explain the glass transition, there is no exact microscopic theory that is able to fully describe it. It is known, that glasses can be obtained by cooling of a melt below a glass transition temperature $T_g$, if nucleation and crystal growth can be prevented until then. Below $T_g$ the melt turns into a solid material without forming a long-range crystal order. Therefore, glasses are usually characterized by the absence of a structural long-range order, whereas a short-range order, which is comparable to its crystalline equivalent, can exist [Fec95].

## 3.1.1. Supercooled liquid

The answer to the question why glasses are considered to be supercooled liquids can be given, if the process of cooling down of two melts is considered in detail (figure 3.2). If a liquid is cooled down (at a constant pressure $p$), its volume decreases and the temperature-dependent linear expansion coefficient $\gamma = \frac{1}{V} \left( \frac{\partial V}{\partial T} \right)_p$ decreases (A). Upon reaching the melting temperature $T_m$, crystallization takes place and an abrupt volume decrease, which is associated with the arrangement of atoms into the periodic lattice, can be observed - a first order phase transition takes place (B). From now on, further cooling of the materials decreases the volume with a lower temperature coefficient (C). However, if no crystallization process occurs during cooling of a second liquid at $T = T_m$ and below, the volume decreases steadily without a sharp step, while the systems finds itself in a metastable equilibrium state. The slope flattens until it reaches the glass transition temperature $T_g$ and after that it runs parallel to the line of the cooled crystal. The material is now in a glassy, non-equilibrium state. The explanation for the described glass-transition is the conflict between the molecular and experimental time scale. This means, that the atomic movements slows down so rapidly, that it is impossible for the system to assume an equilibrium state. The atoms in the liquid are hindered to occupy periodic sites by the strong increase of the viscosity $\eta$, so the arising solid retains the molecular configuration of the liquid. In order to explain, how solidification of a melt in a glassy state can be influenced, the investigations of G. Tammann concerning the crystallization behavior of supercooled liquids is usually adduced. For this, the number of crystallization nuclei per volume
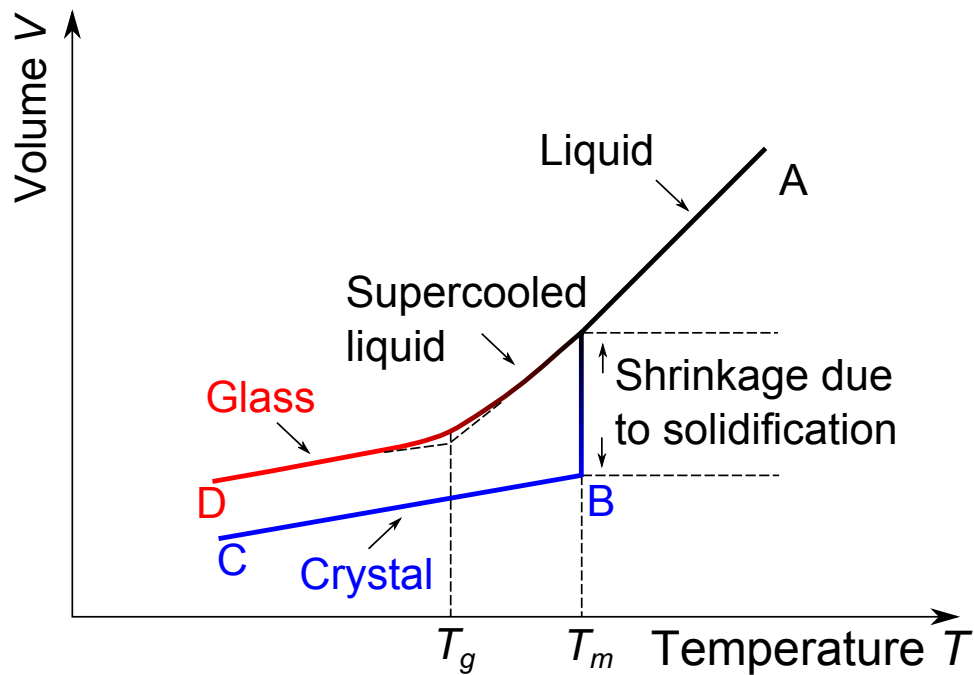
**Figure 3.2.:** Volume change of liquids at $T_m$ and $T_g$, redrawn from [Lin11]

and time $CN$ as well as the crystallization velocity $CV$ play an important role. In figure 3.3, both quantities are plotted as a function of the supercooling. The higher the values for $CN$ and $CV$ are and the more the area of their slopes overlap, the higher the probability of devitrification of the liquid becomes, because there are enough crystallization nuclei for an effective crystal growth. However, if it is possible to use fast cooling rates in the temperature region of the overlap, it is easier to receive a glass, because the main region where crystallization takes place is already passed, before the optimum nucleation zone is reached. Furthermore, a glass can be ceramized by specific heat treatment in the regions of $CN$ and $CV$, which is used when producing glass-ceramic materials.

## 3.1.2. Glass properties

The physical properties of glasses are significantly influenced by their amorphous structure and their chemical composition which determine their character. Most of the commonly used glasses contain mixtures of oxide compounds, however, some applications require fluorides and chalcogenides as components so they can also be found. A common way to describe a certain glass composition is to list their (oxide) components in mole $m_i$ [mol%] or weight fraction $w_i$ [wt%]. With the molar mass $M_i$
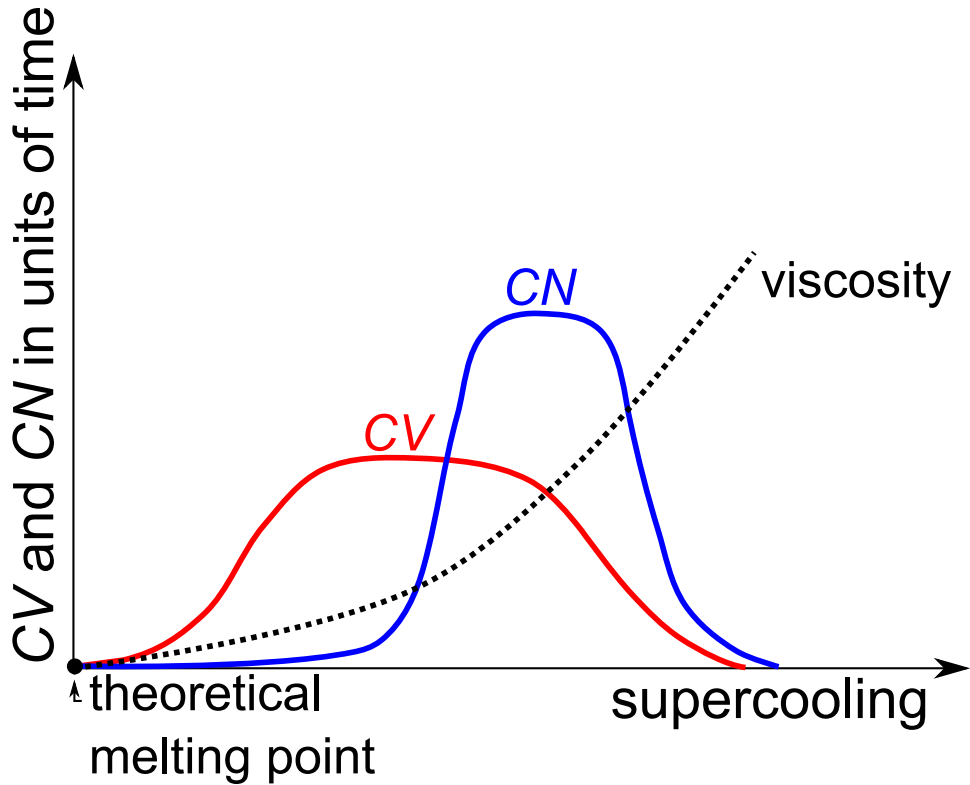
**Figure 3.3.:** Nucleation and crystal growth as a function of supercooling [Lin11]

of the component $i$, both can be converted into each other by equation 3.1 and 3.2

$$m_i = \frac{100 \times w_i}{M_i \sum\limits_{j=1}^{n} \frac{w_j}{M_j}} \tag{3.1}$$

$$w_i = \frac{100 \times m_i M_i}{\sum\limits_{j=1}^{n} m_j M_j} \tag{3.2}$$

Because of the lack of long-range order, glasses usually posses a low thermal conductivity $\kappa$. As a general rule, this thermal conductivity increases with increasing temperature, in contrast to crystalline materials, where a reverse correlation can be observed. This behavior of glasses can be explained by the constant mean free path of the phonons (see equation 1.56 in chapter 1.3.4), so the thermal conductivity is mainly influenced by the behavior of the specific heat. X-ray measurements showed, that the mean free path has the dimension of the short-range order in the glass, which is about 7 Å for silicate glasses and corresponds to the unit cell length of crystalline silicon [Kit49]. Depending on their composition, glasses can show a certain electrical conductivity $\sigma$. The electrical conductivity is usually low and has an ionic

character due to alkali ions in the composition. Increasing the alkali ion concentration and enhancing their mobility in the glass network by applying high temperatures increases the conductivity. Using high concentrations of alkali ions, conductivities of $\sigma = 10^{-3}\,\mathrm{S\,cm^{-1}}$ can be reached. Taking polyvalent ions (Ti, Co, Mo, V, ...) into account, it is also possible to produce semiconducting glasses [Tes13]. However, an ionic conductivity is not desirable in glass-ceramics which are meant for thermoelectric applications. Especially for n-type materials, the different signs of the ions and electrons as charge carriers sum up to a reduced Seebeck coefficient in total and lead to a deterioration of the material efficiency. For that reason, the use of alkali ions for the glass compositions has been excluded for this work.

The density $\rho$ of glasses is also strongly dependent on the composition and the structure of the material. Starting from fused silica glasses, which consist of highly pure $SiO_2$, with a density of $\rho = 2.21\,\mathrm{g\,cm^{-3}}$, over to soda lime glasses with $\rho = 2.52\,\mathrm{g\,cm^{-3}}$ towards optical glasses, which show densities of $\rho = 3.9$ - $6.3\,\mathrm{g\,cm^{-3}}$ due to their heavy components like lead oxide, glasses offer a wide variety concerning this property [MW06].

The refractive index $n$, which gives the ratio of the speed of light in vacuum to the speed of light in the respective medium, is also a characteristic feature in glasses. The values range from $n = 1.45$ - $2.14$, whereas they can still vary due to the dispersion (change of the refractive index with frequency), especially in the infrared spectrum [Fox12].

## 3.2. Motivation for thermoelectricity

Oxides compounds and their potential as a thermoelectric material class have been discussed in the previous chapter. It could be shown, that their unique structural features and the versatile doping possibilities can lead to favorable properties and performances, especially at high temperatures. However, among the listed advantages over other thermoelectric material classes, they have certain drawbacks like their rather high thermal lattice conductivity due to the strong bonds of their light atoms which do not provide effective phonon scattering centers. Furthermore, ceramic materials always show a residual porosity, which leads to an increase of the sample surface and makes them more susceptible to mechanical, chemical and thermal influences. As an example, there are reported studies, where the oxygen exchange at elevated temperatures led to a degradation of the electrical properties during thermal cycling experiments [KWZ+10]. The grain growth and phase formation during sintering can

sometimes be hard to control, which complicates the sample preparation for oxide materials. A legitimate consideration how to approach these disadvantages would be to introduce a secondary phase in the oxide systems, which could balance out the drawbacks while at the same time not contribute additional downsides. One way to implement this is to consider glass-ceramic materials, like shown in this thesis, which is based on glass-ceramic systems and their applicability as thermoelectric materials. Because glasses show a low thermal conductivity, a glass-ceramic system can help to suppress this property compared to its ceramic counterpart and therefore increase the efficiency of the material. Furthermore, the residual glass phase also helps to protect the embedded crystals against external influences and makes them more durable, therefore eliminating the aforementioned issue with the residual porosity of ceramics. The possibility of nucleation in a glassy precursor brings new and alternative routes concerning the conventional sintering process while fabricating the samples. However, it has to be mentioned, that an actual advantage with glass-ceramic materials over conventional ceramics can only be obtained, assuming that the range of the thermoelectric active matrix in the material is high enough to guarantee a continuous connection of the crystals inside the sample. This is demonstrated in figure 3.4. Part a) depicts the case, where the thermoelectric active crystal phase (shown in red) is distributed within the glass (shown in green). Local connections of the crystals are formed, enabling a charge transport on a short length scale but failing to establish a connected path throughout the whole material which results in a low electrical conductivity. Part b) shows the formation of an interconnected path from the left to the right side of the sample. In this case, the microscopic crystals are merged to form a macroscopic conduction path for the material, in which case the electrical conductivity is high. This relation is discussed in more detail in the following chapter.
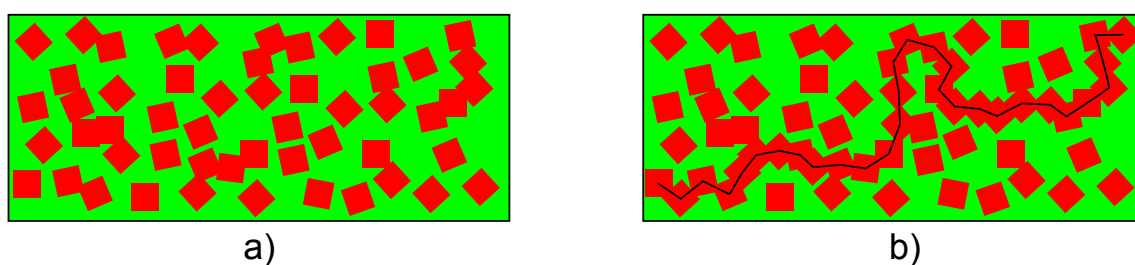


a)                                                            b)

**Figure 3.4.:** Illustration of glass-ceramic material, red squares: crystals, green area: residual glass phase

# 4. Theoretical considerations

This part of the thesis is supposed to give a short introduction to mode-coupling theory after [Sch00], explain the basics of percolation as well as the respective models and relate them to glass-ceramic systems. Furthermore, the concept of electron localization in a disordered solid (Anderson localization) is discussed and its applicability to glass-ceramic systems is shown. The "Rietveld plus internal standard" X-ray method of determining the amount of amorphous and crystalline parts in multi-phase samples is explained and an estimation of its accuracy is made. Finally, a theoretical consideration of reaching the percolation threshold in the investigated samples is proposed and described, which can be used to assess the possibility to receive percolating paths in the glass-ceramic materials.

## 4.1. Mode-coupling theory

A more recent approach to describe the dynamics of supercooled liquids and the related phenomenon of the glass transition is the so called mode coupling theory (MCT) [Göt08], which essentially is based on the assumption that at low temperatures, the nonlinear feedback mechanisms in the microscopic dynamics of the particles become so strong, that they lead to the structural arrest of the system. Fundamental aspects of the glass transition can be obtained from MCT via the evolution equations derived from the Mori-Zwanzig projection formalism. Here, the classification of all observables in relevant and irrelevant quantities gives an exact, strongly nonlinear and generally not solvable differential equation for the relevant observable $G_n(t)$

$$\frac{\partial G_n(t)}{\partial t} = \sum_m \left\{ \Xi_{nm} G_m(t) - \int_0^t K_{nm}(t') G_m(t-t') \mathrm{d}t' \right\} + f_n(t) \tag{4.1}$$

The first part of the sum on the right hand side contains the frequency matrix $\Xi$ which is based on mean values of the relevant observables in thermal equilibrium. The forces $f_n$ and the memory kernel $K_{nm}(t) = F(G_n, G_m, G_n G_m, G_n G_n, ...)$, which is a complicated nonlinear function of the observables, are still dependent on the

irrelevant observables. These Mori equations can be used as a starting point to make approximations for the memory kernel and to derive equations of motion of the correlation functions of relevant observables. Considering density and longitudinal current density, the evolution of the density autocorrelation $\Phi(t) = \langle \rho(0)\rho(t) \rangle$ can be described by

$$\left[ \frac{\partial^2}{\partial t^2} + \gamma_R \frac{\partial}{\partial t} + \Xi^2 \right] \Phi(t) + \int_0^t K(t-t') \frac{\partial \Phi(t')}{\partial t'} \mathrm{d}t' = 0 \qquad (4.2)$$

where $\gamma_R$ is a damping coefficient. In equation 4.2, the residual forces $f_n$ are implicitly accounted for in the memory kernel $K(t)$. A reasonable approximation for this memory kernel via the correlation function $\Phi$ can now lead to a self-consistent equation. The most simple model systems for $K$ which essentially preserve the underlying bifurcation scenario are $K = 4\lambda\Phi^2$ or $K = v_1\Phi + v_2\Phi^2$. If the coupling parameters $(\lambda, v_1, v_2)$ are large enough, a non-ergodic phase emerges, where the correlation function $\Phi$ does not converge to the equilibrium value $\Phi_\infty = 0$ but instead reaches finite value of $\Phi_\infty > 0$, so the glass transition occurs now as a bifurcation scenario of the nonlinear differential equation. The temperature dependence of the coupling parameters is responsible for the existence of a critical temperature $T_c$ at which the system undergoes a transition from ergodic to non-ergodic. Depending on the interpretation, this dynamic transition can be considered as a kind of phase transition.

## 4.2. Percolation

Percolation theory is a mathematical framework, which is used in physics, chemistry and materials science when describing disordered systems. In general, it deals with the formation of locally connected areas on randomly occupied lattices. With percolation models, transport mechanisms in multi-phase compounds as well as the properties of complex composite materials can be described. The fundamental principles, on which the description in this section is based upon, can be found in [SA94] and [BK05].

### 4.2.1. Percolation models

The basic terms needed to discuss percolation can be explained by looking at the so-called site percolation as an example. For that, a square lattice with the size of $n \times n$
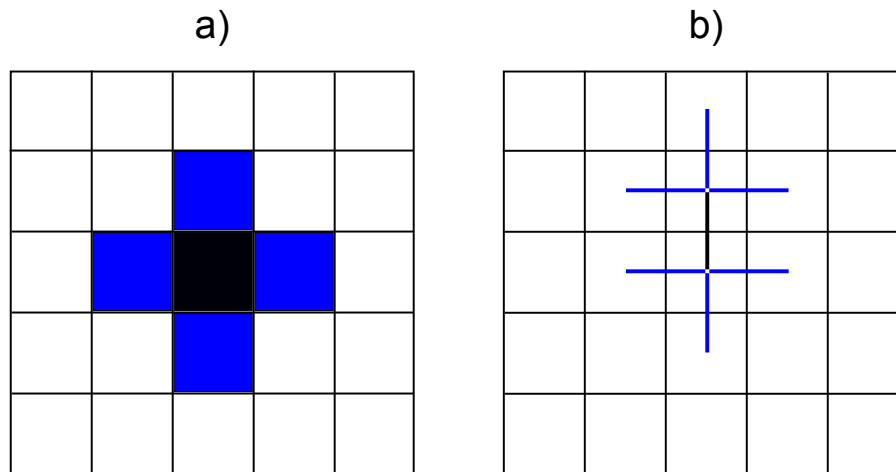
a)                  b)

**Figure 4.1.:** Site percolation (a) vs. bond percolation (b), black: occupied site/vertex, blue: nearest neighbors

is considered, where the lattice sites $i$ are occupied with a probability of $p$. The occupancy or the vacancy of a given site is only dependent on this occupation probability, so there is no interaction between the separate sites. The lattice is assumed to be infinitely extended, which is why boundary effects are negligible. An occupied site on the lattice can now be linked to a physical property, which is the electrical conductivity $\sigma$ in this case. An occupied site corresponds to an electrical conductor, whereas a vacancy on the lattice represents an insulator. A charge transport can only occur between neighboring sites. Depending on the occupation probability $p$, random distributions of occupied and vacant sites take place on the lattice, whereas neighboring occupied sites form so-called clusters. For a low occupation probability $p$, there are no clusters of conducting sites, which span from one site of the lattice to the opposite site. This makes the system behave like an insulator. With increasing occupation probability $p$, the size of the forming clusters grows. Upon reaching a critical threshold $p_c$, the cluster size has grown so much, that it is extended through the whole lattice. This is called a percolation of the system, the quantity $p_c$ is called percolation threshold. In this case, the system shows an electrical conductivity. In the limiting case of $p = 1$, all sites are occupied and belong to a single, large percolating network. In comparison to thermal phase transitions, which are characterized by certain temperatures, percolation can be understood as a geometrical phase transition, which is characterized by the critical occupation probability $p_c$.

A similar consideration of the randomized occupation is the so called bond percolation. In this case, all lattice sites are assumed to be occupied and the connections of the sites and their neighbors are considered. Here, $p$ describes the probability, that a

connecting path from one site to its neighboring site is opened. In this consideration, $p_c$ denotes the critical probability, at which enough opened connections between the sites exist, so that percolation through the whole network across the lattice is possible. Transferred to the glass-ceramic, it can be considered as follows: An occupation of a lattice site represents the existence of a thermoelectric active region, a vacant site stands for the insulating, residual glass phase. If the system is below the percolation threshold, only a very low electrical conductivity can be reached (e.g. high energy barriers for the hopping process between two non-neighboring sites, residual glass phase effectively hinders the charge transport). In the critical area around $p_c$, a strong increase of the conductivity can be observed, because a connected path is formed, which is used for the charge transport. An increase of the crystal ratio above this threshold leads only to a comparably small further increase of the conductivity.

The exact value of the percolation threshold is dependent on the dimensionality and the shape of the respective lattice, as well as the considered model. It is obvious, that a $d$-dimensional lattice $N^d$ can always be embedded into a ($d$+1)-dimensional lattice $N^{d+1}$. Therefore, the existence of a percolating cluster in $N^d$ always implies its existence in $N^{d+1}$. That leads to the relation $p_c(d+1) \leq p_c(d)$ between the percolation thresholds of these lattices. Furthermore, the percolation threshold in the site percolation model is higher than in the bond-percolation model, since the number of next neighbors in the latter case (while keeping the same lattice) is higher. An example of this is shown in figure 4.1, which shows the site and bond percolation of a two-dimensional square lattice. An occupied site in the site percolation model has four next neighbors, while a connection between two sites in the bond percolation model has the possibility to access six neighboring sites. Usually, analytic expressions for the percolation threshold can only be given for the one-dimensional case and for a few, two-dimensional exceptions. Table 4.1 shows percolation threshold values $p_c$ for some frequently used lattices. Another important quantity, which is needed to describe percolation phenomena, is the probability $P$, that an arbitrary site on the

| lattice type | $p_c$ site | $p_c$ bond |
|---|---|---|
| 1D chain | 1 | 1 |
| 2D square | 0.593 | 0.5 |
| 2D triangle | 0.5 | 0.347 |
| 3D sc | 0.312 | 0.249 |
| 3D bcc | 0.246 | 0.180 |
| 3D fcc | 0.198 | 0.119 |

**Table 4.1.:** Percolation threshold values for different lattices and models [SA94]

lattice belongs to the percolation cluster. This quantity can be expressed by

$$P \propto (p - p_c)^{\beta} \tag{4.3}$$

Below $p_c$, this probability is $P = 0$, because no percolating cluster exists. Above $p_c$, $P$ approaches a value of 1, because a complete occupation of the lattice means, that every site is part of the infinite cluster. Likewise, the mean size of the finite clusters $\chi$ can be defined by

$$\chi \propto |p - p_c|^{-\nu} \tag{4.4}$$

This correlation length $\chi$ characterizes the mean distance between two occupied sites on the same finite cluster. In the region near $p = p_c$, the expression obtained from 4.4 diverges, since the finite size of the finite cluster merges into the infinite cluster. After that, $\chi$ decreases again, since occupied sites can now be part of the infinite cluster, which lowers the probability of large finite regions with increasing occupation probability $p$. The quantities $\beta$ and $\nu$ stand for universal constants, which are solely dependent on the dimension of the respective system. In the case of three dimensions, these can only be obtained numerically and the result is for $\beta = 0.417 \pm 0.003$ and $\nu = 0.875 \pm 0.008$ [BH12]. Figure 4.2 shows the slope of both quantities with their corresponding exponents. Figure 4.3 shows a two-dimensional square lattice with
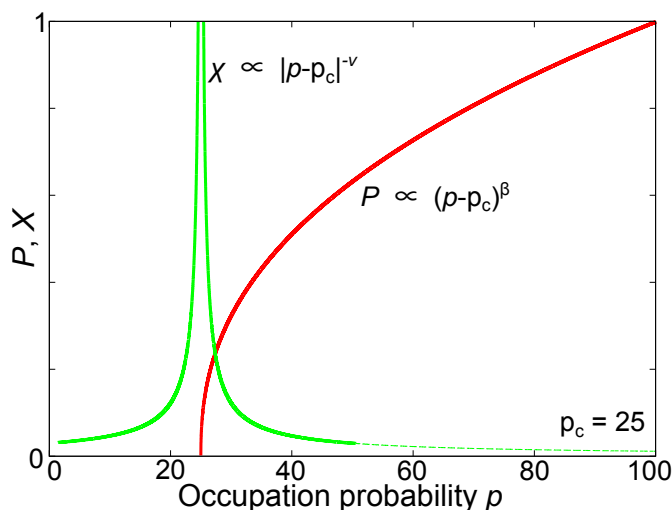


**Figure 4.2.:** Infinite cluster probability $P$ and correlation length $\chi$ on a 3D lattice

different occupation probabilities $p$. The importance of the percolation threshold is demonstrated by the values of $p$ and the occupied sites before and after the percolation threshold $p_c = 0.593$. Below this value, there is no connecting cluster across the whole lattice (finite cluster in blue), above the critical condition, the infinite cluster (depicted in green) extends from each site of the lattice to the opposing ends.
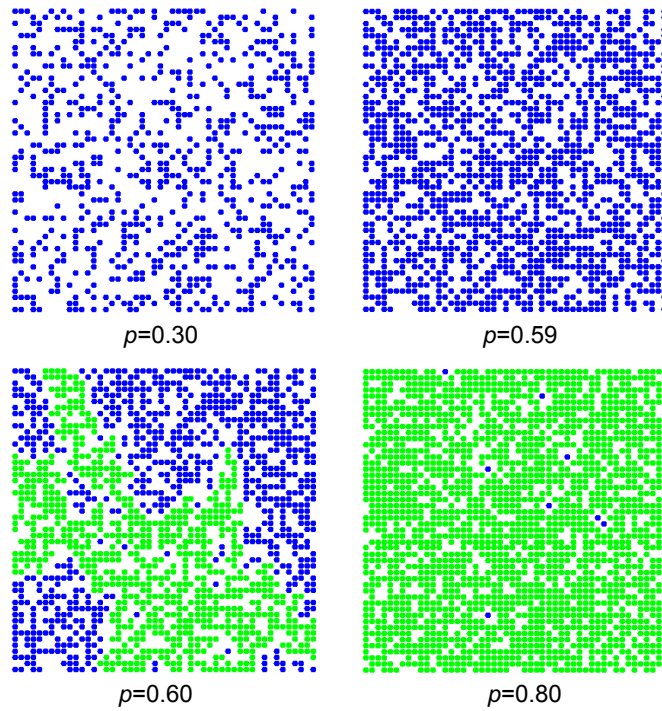
**Figure 4.3.:** Simulation of different occupation probabilities $p$ on a $50 \times 50$ 2D square lattice, $p_c = 0.593$, empty sites are white, occupied sites are blue, spanning clusters are shown in green [Gon]

In the vicinity of the percolation threshold, on length scale smaller than $\chi$, the finite as well as the infinite cluster are self-similar. This means, that the received structure from a magnification of a small section on the cluster can not be distinguished from the original section itself. As a consequence of this self-similarity, the clusters can be characterized by a so-called fractal dimension, which is smaller than the Euclidean dimension $d$ of the embedding lattice.

The fractal dimension can be defined under theoretical aspects via the expression of the Hausdorff dimension. This can be understood in a simplified way (not valid for spatially varying iteration depth), using an extended, finite point set in three dimensional space. Considering the amount of spheres $N$ with radius $r$, which are required to cover the point set, this is a function $N(r)$. If the radius decreases, more spheres are needed to cover the existing points. The Hausdorff dimension $D$ can be determined by the exponent of $r$, when $N(r)$ grows like $\lim\limits_{r \to 0}$.

$$N(r) \propto \frac{1}{r^D} \qquad (4.5)$$

From this it follows that

$$D = \lim_{r \to 0} \frac{\log N}{\log r} \tag{4.6}$$

The Hausdorff dimension $D$ can be expressed for the special case of an object, which consists of $n$ disjoint partial objects, which can be seen as a smaller copy of the original with a scale of 1:$m$.

$$D = \frac{\log n}{\log m} \tag{4.7}$$

For a square, which consists of four identical squares with half the side length of the original, the dimension can be calculated as $D = \frac{\log 4}{\log 2} = 2$. Considering the Koch curve, which consists of four smaller copies with a scale of 1:3, the dimension reads $D = \frac{\log 4}{\log 3} = 1.2618$. This concludes, that the Hausdorff dimension does not necessarily
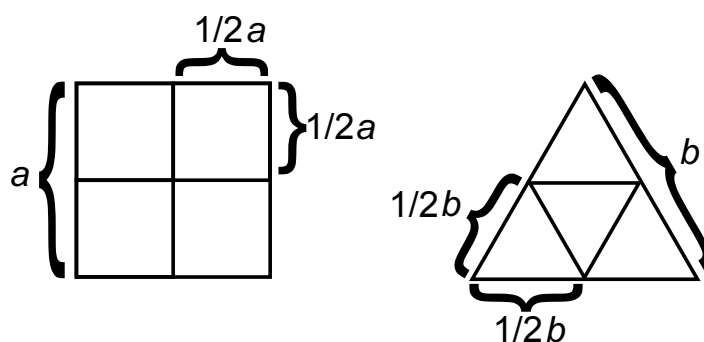


**Figure 4.4.:** Geometrical subdivisions of a square and a triangle

match the Euclidean dimension $d$ and can assume rational or irrational values in fractal dimensions [Sch88].

The mean mass $M$ of a cluster, within the radius of $r$ being below the correlation length $\chi$, increases with the fractional exponent $d_f$. On length scales of $r$ greater than $\chi$, the mass $M$ increases with the exponent being the dimension of the lattice $d$.

$$M(r) \propto \begin{cases} r^{d_f} & \text{for } r \ll \chi \\ r^d & \text{for } r \gg \chi \end{cases}$$

It can be shown, that the fractal dimension $d_f$ can be expressed by the critical exponents of equation 4.3 and 4.4. For this, the expression for the mass of the infinite cluster $M$ on an infinitely extended lattice $L^d$ is considered. In this case, the relation $M \propto L^d P$ holds, because the mass is proportional to the product of lattice size and probability $P$ to belong to the infinite cluster. Likewise, the mass is proportional to the product of the number of unit cells $\left(\frac{L}{\chi}\right)^d$ and the mass of the unit cell $\chi^{d_f}$ itself.

Using the expressions for $P$ and $\chi$ from equation 4.3 and 4.4 yields

$$M \propto L^d P \propto L^d (p - p_c)^\beta \propto \left(\frac{L}{\chi}\right)^d \chi^{d_f} \propto L^d (p - p_c)^{\nu d - \nu d_f} \tag{4.8}$$

By comparing the exponents, this leads to

$$d_f = d - \frac{\beta}{\nu} \tag{4.9}$$

Using the numerical values for $\beta$ and $\nu$, for $d = 3$ a fractal dimension of $d_f = 2.52$ can be calculated, which is universal for three dimensional systems.

Considering a fractal cluster, it contains several substructures. Upon applying an external voltage, a current flows as soon as the system shows a percolating path. However, a majority of the paths within the percolating cluster do not contribute to the charge transport. That means, that the cluster can be considered as containing a main line, on which the charge carriers flow and side arms, that do have a connection to the main line but are not important for the charge transport (see figure 4.5). Because the majority of the percolating cluster's mass is located in these side arms, the fractal sub-dimension of the main line $d_m$ is even smaller than the fractal dimension of the cluster $d_f$ and has a numerical value of around $d_m = 1.86$ in three dimensions.

$$M(r) \propto \begin{cases} r^{d_f} & \text{for } r \ll \chi, \text{cluster} \\ r^{d_m} & \text{for } r \ll \chi, \text{backbone} \end{cases}$$

Because the electrical conductivity is proportional to the amount of charge carriers and therefore to the amount of mass on the main line, the fractal dimension of the path of the charge carrier transport can be interpreted as an effectively reduced dimension of the conductivity. In conclusion, the charge transport in a percolating system takes place at a lower dimension than the host lattice's, which is why from a simple geometrical point of view, the conductivity should be smaller as in the non-fractal case. However, for a more precise consideration, the exact charge carrier mechanism has to be studied and the electronic density of states near the Fermi energy has to be taken into account. The publications of M. Dresselhaus ([HD93a], [HD93b]) showed, that a low dimensional transport in semiconducting materials can actually be favorable for thermoelectric systems, because the density of states near the band edges is enhanced, when the dimension of the electronic movement is confined, which increases the Seebeck coefficient.
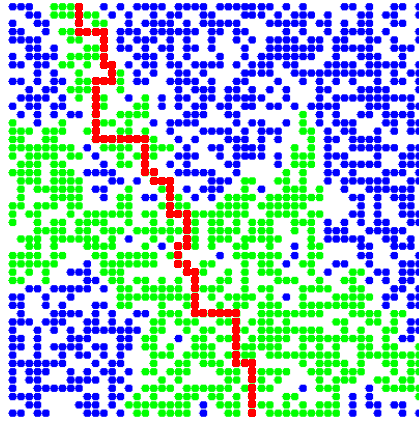
**Figure 4.5.:** 2D percolating cluster (green) with backbone path (red)

## 4.3. Anderson localization

In the previous section it could be shown, that a metal-insulator transition can not only be reached by adjusting external parameters like the composition, temperature, pressure [BSB99] or magnetic fields [LW91] but also by an increasing random occupation of lattice sites. Furthermore, the transition can be driven by the increase of disorder in a crystal, which is noticeable by the enhanced disturbance of the periodic lattice potential. This description is know as the Anderson localization and named after P. W. Anderson, who studied crystal lattices where the periodic potential is subjected to statistical variations [And58]. From a classical point of view, localization can be understood as the state, where the particle energy inside a potential is not sufficient to overcome the potential barrier, thus confining it within its boundaries. Quantum mechanics offers the possibility of tunneling, which is why the term has to be rephrased here, especially since Anderson localization can also occur, if the particle energy is higher than the potential barrier. Therefore, localization in this context can be understood as the case, when the wave function $\Psi$ decreases fast enough from a center $r_0$ as

$$|\Psi(r)| \propto \exp - \left( \frac{|r - r_0|}{\chi} \right) \tag{4.10}$$

Here, a small correlation length $\chi$ leads to a faster decrease of the function $\Psi$. In order to visualize the localization, it is beneficial to recall some basic insights on the quantum mechanical description of ideal and disturbed crystals. In an ideal crystal with a periodic potential $V$, the translation invariance leads to Bloch waves for the solution of Schrödinger's equation. Those are wave functions with a periodic amplitude, which are delocalized across the whole crystal within an energy band $B$. If the Fermi energy of the system is in the conduction band, the electrons are
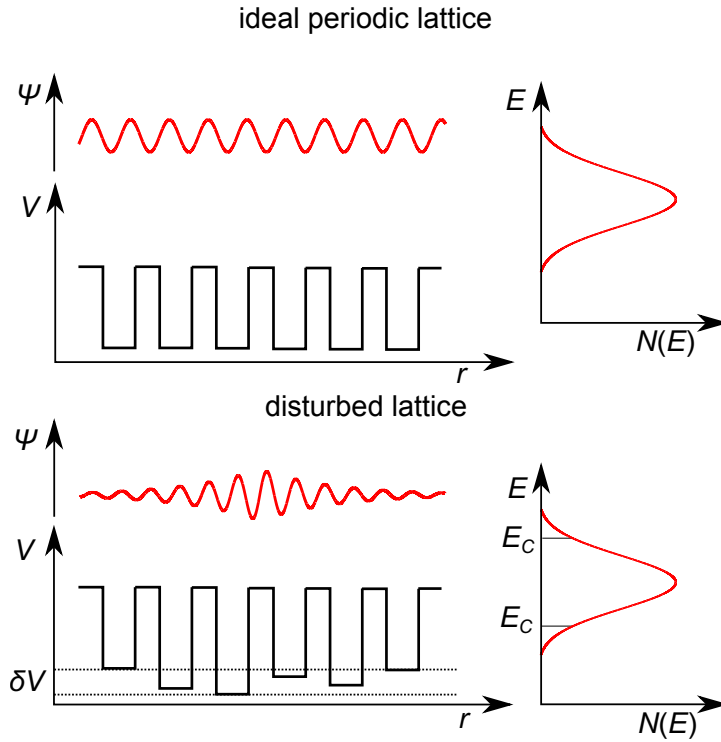
ideal periodic lattice



disturbed lattice

**Figure 4.6.:** Wave function $\Psi$, potential $V$ and corresponding density of states $N(E)$ for electrons in an ideal and disturbed crystal

free to move and an electrical transport is possible [Kit99]. Impurities in the ideal configuration lead to a symmetry break and render the Bloch waves insufficient for solving Schrödinger's equation. For a strong disorder, it is not sufficient to treat the periodic potential with methods of perturbation theory. The wave functions must be considered for a periodic potential with statistical fluctuations $\delta V$, which leads to a partial or complete reversion of the delocalization. The Anderson localization can be described using an example of the charge carrier movement [Pet10]. Considering the probability $W(\text{A,B})$, which applies to the movement of a particle from impurity site A to site B, the sum of all possible paths $\Gamma$ the particle can chose on its way from A to B has to be accounted for. For this consideration, the particle is only scattered at the impurity sites and experiences a free movement in between those (no electron-electron interaction).

$$W(\text{A}, \text{B}) = \left| \sum_{\Gamma} P(\Gamma) \right| \tag{4.11}$$

The single probability amplitudes are described by $P(\Gamma) = p_{\Gamma} e^{i\phi_{\Gamma}}$, where $\phi_{\Gamma}$ denotes the phase angle which depends on the path and the potential, which has been passed. An example for this is shown in figure 4.7 a, where two different paths to move from A to B are depicted. A particle can be considered as localized, if after passing through
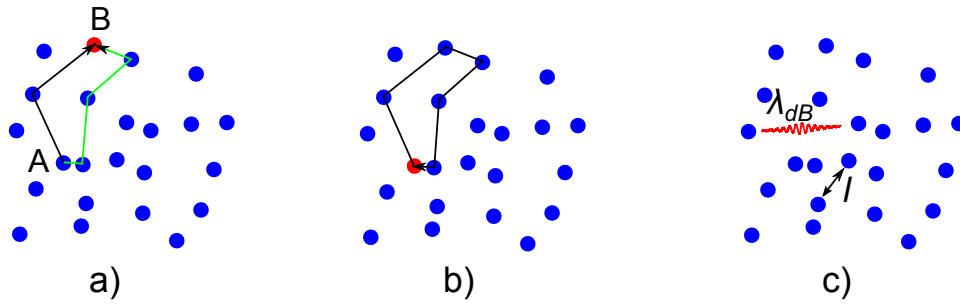
**Figure 4.7.:** Illustration of scattering paths in the Anderson-model

the impurities on a certain path, it is relocated at its original site, which corresponds to a probability $W(A,A)$ (see figure 4.7 b). For an arbitrary closed path $\Gamma$, it is also possible going in the opposite direction $-\Gamma$, where the phase shift is $\phi_\Gamma = \phi_{-\Gamma}$ because of the same path. If the density of scattering centers inside the material is high, there are many closed paths with a high amplitude, which leads to a high probability to remain at site $A$, due to the coherent phase difference. In this consideration, two quantities are important for the discussion of the localization. The properties of the charge carriers are represented by the de-Broglie wavelength $\lambda_{dB} = \frac{h}{p}$, while the mean free path $l$ characterizes the properties of the random potential (mean distance between two impurities) and can therefore be understood as a degree of distortion (see figure 4.7 c). A. F. Ioffe [IR60] showed, that the boundary condition for the localization in three dimensions can be expressed by

$$l < \lambda_{dB} \tag{4.12}$$

This limitation leads to so-called mobility edges $E_C$, because only particles with a momentum of $p > \frac{h}{l}$ can move freely in this picture. The free motion is therefore limited to particles, where the energy is in between the boundaries of the mobility edges in the density of states (see figure 4.6). With increasing disorder, the mobility edges move together and starting from a critical degree of disorder, all states are localized and the band will not contribute to the conductivity at $T = 0\,\text{K}$.

Apart from the Anderson insulator, there are other models, that explain the insulating character of a material. Among those are the ones, which describe the electron inter-action with an ideal periodic potential (Bloch-Wilson band insulators), the electronic interaction with a periodically modulated lattice potential (Peierls insulators) as well as the electron-electron interaction as in the Mott-insulators. This classification is rather theoretical, because in real systems, there is never a single mechanism, which completely describes the material. An insulator is therefore characterized by the dom-

inating scattering mechanism, with the possibility of having mixed cases. An example for this is the Mott-Anderson insulator, where the electron-electron interaction as well as the impurity scattering cause the insulating behavior.

Transferred to the glass-ceramic, this means, that crystallizing of electrically conductive crystals can not only be understood within the percolation model but also within the scope of Anderson localization. By crystallizing, the amorphous, disordered and therefore insulating system can be transferred into a system, where the mobility edges in the density of states can be shifted outwards in order to convert a part of the localized wave functions into a delocalized part.

## 4.4. Approximation for a synthesis to phase content correlation

In order to be considered as electrically conductive materials, the amount of thermo-electric crystals inside glass-ceramics has to overcome the percolation threshold $p_c$ as described in section 4.2. Since the actual contribution to the electrical conductivity correlates with the amount of batch powder of the crystal phase forming oxides, it is crucial to make sure, that this initial amount of crystal-forming oxides in the batch powder mix suffices to provide the necessary quantity requirements for the formation of a percolating path. For that, knowledge of the densities and weight fractions of crystal phase and residual glass phase is needed. Since Archimedes' principle only yields a total, mean density of the material, no information of the individual densities can be obtained by a measurement. In order to give an approximate value for those, a different approach has to be chosen, which is similar to the linear relation of weight fraction and thermal properties investigated by A. Winkelmann and O. Schott [WS94]. The present approach, which establishes a correlation between density and volume fraction based on the weight ratios and individual densities from literature, is demonstrated using a composition, which has been extensively used in this thesis (VSM 39972, shown in table 4.2). Since a glass-ceramic material consists of a crystal phase and a residual glass phase, both have to be considered separately for estimating their density. Starting with the residual glass phase, $SiO_2$ and $B_2O_3$ as well as $Y_2O_3$ and $Sb_2O_3$ are completely incorporated into the residual glass phase[1]. For $SiO_2$ and $B_2O_3$, the densities of their amorphous modifications can be taken from literature ($SiO_2$ $\rho = 2.19\,\mathrm{g\,cm^{-3}}$, $B_2O_3$ $\rho = 1.83\,\mathrm{g\,cm^{-3}}$). Comparing these densities with their

---

[1]This could be shown by methods of X-ray diffraction and energy dispersive X-ray spectroscopy on sample VSM39972, as described in the experimental part of this work

| Component | mole fraction [%] | weight fraction [%] |
|---|---|---|
| $SiO_2$ | 16.90 | 10.84 |
| $B_2O_3$ | 11.54 | 8.58 |
| $Y_2O_3$ | 1.76 | 4.24 |
| $Sb_2O_3$ | 0.1 | 0.31 |
| SrO | 35.61 | 39.41 |
| $TiO_2$ | 30.30 | 25.85 |
| $Nb_2O_5$ | 3.79 | 10.76 |

**Table 4.2.:** Composition of VSM 39972

respective crystalline modifications, a ratio of about ³/₄ can be found. In the absence of available data for the other components, the crystalline densities of $Y_2O_3$ and $Sb_2O_3$ will be scaled by this factor, to estimate a hypothetical amorphous density of these compounds. The values are summarized in table 4.3. In a second step it is assumed,

| Component | $\rho$ amorphous [$g\,cm^{-3}$] | $\rho$ crystalline [$g\,cm^{-3}$] | wt% normalized |
|---|---|---|---|
| $SiO_2$ | 2.19 [Röm96] | 2.65 [Röm96] | 45.2 |
| $B_2O_3$ | 1.83 [HWW07] | 2.56 [HWW07] | 35.8 |
| $Y_2O_3$ | 3.76 [c] | 5.01 [Eag94] | 17.7 |
| $Sb_2O_3$ | 4.23 [c] | 5.7 [Lid10] | 1.3 |
| SrO | - | 5.0 [SJ81] | 51.8 |
| $TiO_2$ | - | 4.24 [Sam73] | 34.0 |
| $Nb_2O_5$ | - | 4.55 [GW64] | 14.2 |

**Table 4.3.:** Densities of glass components, [c] = calculated

that the volume of the glass phase can be additively expressed by the individual volumes of the amorphous phases, so the individual densities $\rho_i$ of those components, scaled with their weight percentage, can be reciprocally added to an effective total density $\rho$ as expressed by equation 4.13.

$$\frac{1}{\rho} = \sum_i \left( \frac{wt\%_i}{\rho_i} \right) \tag{4.13}$$

From the initial composition, the individual weight percentages of the glass-forming oxides are normalized. The total glass density $\rho_G$ can now be calculated from the normalized weight percentages as well as the approximated individual densities from table 4.3 using equation 4.13. This yields $\rho_G = 2.21\,g\,cm^{-3}$. Using the same principle but with the crystal-forming oxides, the density of the crystal phase $\rho_C$ can be calculated from the individual densities of the crystal-forming oxides as well as their normalized weight percentages wt%. This results in $\rho_C = 4.65\,g\,cm^{-3}$. Using the weight percentage fraction of the glass and crystal and the calculated densities

$\rho_G$ and $\rho_C$, the density of the glass-ceramic can now be estimated. This was also done using equation 4.13 and it yielded $\rho_{GC} = 3.68\,\mathrm{g\,cm^{-3}}$, which reproduces the experimentally obtained value of $\rho_{GC_{\mathrm{exp}}} = 3.71\,\mathrm{g\,cm^{-3}}$ (Archimedes' method) with less than one percent deviation. From the ratio of glass density $\rho_G$ to glass-ceramic density $\rho_{GC}$, scaled with the fraction of weight percentage, the volume percentage $\mathrm{vol\%}$ of the glass $V_G$ can now be approximated. Likewise, the ratio of crystal phase density $\rho_C$ to glass-ceramic density yields the volume percentage of the crystal phase $V_C$.

$$\frac{\rho_i}{\rho_{GC}} = \frac{\frac{m_i}{V_i}}{\frac{1}{1}} \rightarrow V_i = m_i \frac{\rho_{GC}}{\rho_i} \tag{4.14}$$

The calculated density $\rho_C = 4.65\,\mathrm{g\,cm^{-3}}$ of SrTiO$_3$ from equation 4.13 does not match the literature value ($5.11\,\mathrm{g\,cm^{-3}}$ undoped, $5.28\,\mathrm{g\,cm^{-3}}$, 20 % Nb, calculated via Powdercell software) which shows that the method of obtaining a mean density from the individual densities of the components might not be very accurate for crystalline materials. A second calculation for the volume fraction has been carried out, using $5.28\,\mathrm{g/cm^3}$ as the density $\rho_C$ for SrTiO$_3$. The density of the residual glass phase has been left at the same value, in the absence of a reference value. Using both densities for the phase SrTiO$_3$, the calculation yields a crystal phase amount of 53 - 60 %, for the given composition. Assuming a total error of $\approx 20\,\%$ (which is quite reasonable considering the amount of approximations which have been used), a crystal phase content of 42 - 48 vol% can be achieved in the worst case scenario. Upon completely crystallization of the components SrO, TiO$_2$ und Nb$_2$O$_5$, a crystal phase content of $\approx 45\,\mathrm{vol\%}$ of SrTiO$_3$ would be possible, which is well above every three dimensional percolation threshold (which has been considered in table 4.1, $p_c$ = 12 - 31 %) regardless of the considered percolation mechanism (site/bond percolation) or the respective lattice type (sc, bcc, fcc, ...). However, it has to be mentioned, that a complete crystallization of a crystal phase in a glass-ceramic is usually not viable, because the field of crystallization in the phase diagram is limited and upon crystallization, the remaining glass composition shifts to compositional regions, where the crystallization of secondary phases is more favored. Taking this into account, assuming a complete crystallization of the desired components, according to this approximation, the annealing of a glassy sample with the mentioned composition should lead to a sufficiently high phase content and to a percolating system. If the individual crystals posses a high electrical conductivity, the macroscopic conductivity should not be deteriorated too much from the residual glass phase under the presented conditions.

## 4.5. Determination method for the amorphous/crystalline amount in glass-ceramics

In order to receive information on the amorphous content of glass-ceramic sample to estimate the crystal phase content, there are a variety of experimental possibilities and procedures to obtain this information. If an X-ray measurement on a sample with a known amount of amorphous content is carried out, the Rietveld refinement can help to quantify the intensity and position of the amorphous glass-hump. Using these parameters, this measurement can be taken as a standard and other samples can be measured and their amorphous content can be obtained by comparing the ratios. However, this does only work as long as the composition of the amorphous fraction is unchanged, because otherwise the changed position and height of the parameters would render this method useless [RCF98].

A more flexible method [Wes07] adds a known amount of crystalline standard $c_{\text{standard}}^m$ to the powdered sample material $c_{\text{sample}}^m = c_{\text{amorphous}}^m + c_{\text{crystalline}}^m$ and both powders are thoroughly mixed. After the X-ray measurement, the ratio of standard phase to crystalline phase can be calculated by means of Rietveld refinement. Because the absolute amount of standard is known, is is possible the determine the crystalline amount. The amorphous amount can be obtained from the difference to the total amount of the sample. This method is feasible for samples with different compositions, but sensible to errors during sample preparation and homogenizing. It is based on the fact, that the ratio of the mixture of crystalline part $c_{\text{crystalline}}^m$ to the amount of weighed in standard $c_{\text{standard}}^m$ is not changed by the Rietveld refinement.

$$c_{\text{crystalline}}^m : c_{\text{standard}}^m = c_{\text{crystalline}}^R : c_{\text{standard}}^R \tag{4.15}$$

The amorphous part of the mixture $c_{\text{amorphous}}^m$ is calculated by

$$c_{\text{amorphous}}^m = 100\% - c_{\text{crystalline}}^m - c_{\text{standard}}^m \tag{4.16}$$

$$= 100\% - \frac{c_{\text{standard}}^m}{c_{\text{standard}}^R} \times c_{\text{crystalline}}^R - c_{\text{standard}}^m \tag{4.17}$$

$$= 100\% - \frac{c_{\text{standard}}^m}{c_{\text{standard}}^R} \times (100\% - c_{\text{standard}}^R) - c_{\text{standard}}^m \tag{4.18}$$

$$= 100\% \left(1 - \frac{c_{\text{standard}}^m}{c_{\text{standard}}^R}\right) \tag{4.19}$$

Equation 4.19 only describes the amorphous amount in the mixture $c_{\text{amorphous}}^m$, in order to calculate the amorphous amount in the sample $c_{\text{amorphous}}^0$, the standard has to be

subtracted

$$c_{\text{amorphous}}^0 = \frac{100\%}{c_{\text{sample}}^m} \cdot c_{\text{amorphous}}^m \tag{4.20}$$

$$= \frac{100\%}{100\% - c_{\text{standard}}^m} \times c_{\text{amorphous}}^m \tag{4.21}$$

$$= \frac{100\%}{100\% - c_{\text{standard}}^m} \times 100\% \left(1 - \frac{c_{\text{standard}}^m}{c_{\text{standard}}^R}\right) \tag{4.22}$$

An example would be a glass-ceramic with a single crystal phase, where a standard of $c_{\text{standard}}^m = 50$ wt% ZnO has been added. Assuming the Rietveld analysis yields a fraction of $c_{\text{standard}}^R = 70$ wt% ZnO to $30$ wt% main crystal phase, equation 4.22 gives an amorphous content of $c_{\text{amorphous}}^0 = 57.14$ wt% and therefore a crystalline fraction of $c_{\text{crystalline}}^m = 42.86$ wt%. Because equation 4.22 gives a non linear relationship of amorphous phase content $c_{\text{amorphous}}^0$ and weighed-in standard $c_{\text{standard}}^m$, there are certain limitations to its applicability concerning the accuracy of this method. Figure 4.8
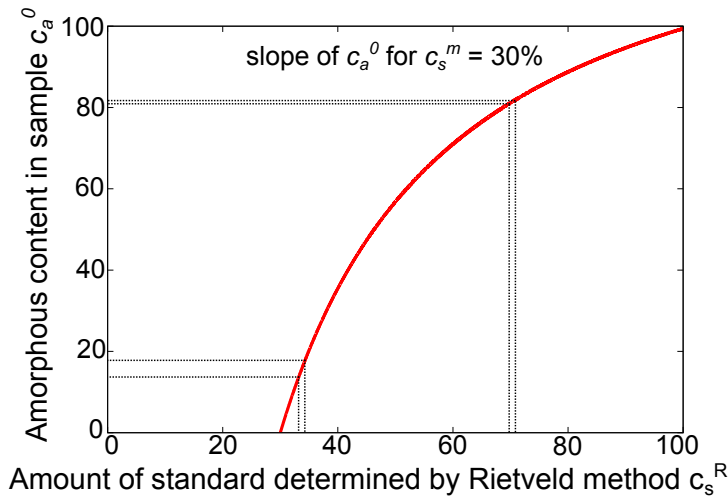


**Figure 4.8.:** Uncertainty intervals for the amorphous content in the sample

shows a plot of equation 4.22 depending on $c_s^R$. Is is obvious from looking at the slope of the curve, that the determination method yields more accurate results, if the amorphous content in the sample is high. Therefore, it is not only necessary to chose a standard material, which has a similar X-ray absorption than the investigated crystal phase but also to adjust the amount of weighed-in standard to the expected ratio of amorphous to crystalline substance. If a large amount of standard is weighed in, this leads to a bigger uncertainty according to figure 4.8 and equation 4.22. This has to be kept in mind when evaluating the experimental data and taken into account, when comparing the outcome to results from other determination methods.
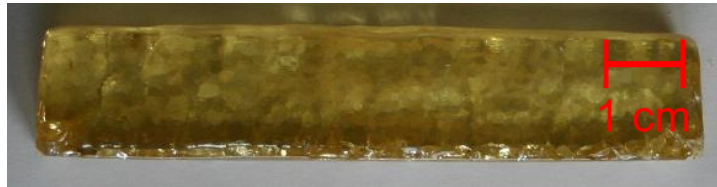
# 5. Experimental work



**Figure 5.1.:** SrTiO$_3$ glass 39972 before ceramization

This part of the thesis describes the development of the glass-ceramic materials, which this work is based upon and depicts the methods and measurements that have been used and carried out in order to characterize them. For this experimental description, a glass-ceramic system containing Nb-doped SrTiO$_3$ as a main crystal phase (n-type) is discussed in detail and a short overview on the development of a glass-ceramic with Bi$_2$Sr$_2$Co$_2$O$_x$ as the main phase (p-type) is presented. Their thermoelectric properties are evaluated and reported in the following sections. A different approach to obtain glass-ceramic samples from a sintering process of a semi-crystalline powder rather than a conventional melt and subsequent annealing is also presented. Eventually, both glass-ceramic materials from the conventional melt process are meant to be implemented in a thermoelectric module, which is why the last section of this chapter reports on the fabrication process and the properties of said module. All of this is preceded by a section that introduces and explains the characterization methods which have been employed.

## 5.1. Characterization

When working with functional materials, from a physical point of view and especially during the development of thermoelectric samples, it is inevitable to be concerned with the different characterization methods to obtain information on phase formation, microstructure as well as electric and magnetic properties. The principles of the most important methods will be explained in the following sections and related to the respective context of this work.

## 5.1.1. Differential thermal analysis

The differential thermal analysis (DTA) is a thermal screening process for the analysis of materials and their phase formation and transition in particular. It utilizes the fact, that all substances show a characteristic enthalpy change $\Delta H$ during phase transformations. For a DTA measurement, the concerning sample is put into a small crucible while a second, identical crucible is filled with a reference material. This reference sample is chosen in a way, that it does not show any phase transitions in the concerning temperature range. Both samples are heated up simultaneously, while the sample temperature $T_S$ and the reference temperature $T_R$, or rather their temperature difference $\Delta T = T_S - T_R$, are measured by thermocouples and plotted against the absolute temperature $T$. A phase transition taking place in the investigated sample (crystallization, crystal phase transformation, melting) is indicated by the signal of the temperature-difference $\Delta T$. In an endothermic reaction (positive enthalpy change $\Delta H > 0$), which is observed at the melting points of the material or the crystal phases or upon reaching the glass transition temperature $T_g$, the sample temperature $T_S$ stays lower than the temperature of the reference. This is, because the energy from the heating process is needed to break the atomic bonds and can therefore not be used to increase the temperature of the sample. This results in a negative temperature difference as defined above and the signal shows a dip in this region. Conversely, crystallization taking place leads to an increase in sample temperature $T_S$, due to the released heat of crystallization, which is added on top of the sample temperature itself. The temperature difference $\Delta T$ is positive and a peak can be observed. All of this is shown exemplarily in figure 5.2 which depicts the dips and peaks for a
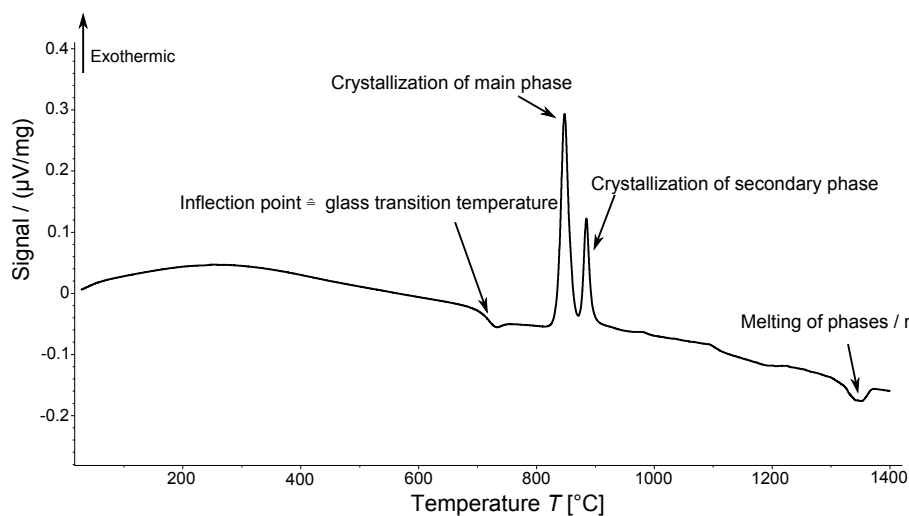
**Figure 5.2.:** Example of a DTA with characteristic peaks, $\Delta T \propto$ voltage signal

glass-ceramic material. Ideally, the peaks should rise linearly from the moment of the onset of the phase transition [Hai95]. Because the DTA is a dynamic measurement, where heat is exchanged between sample, sample holder and thermocouples during the whole measurement, the temperature distribution is hardly ever completely homogeneous, so an ideal linear increase will usually not be observed. After the maximum of the peak is reached, the peak flank of the temperature difference $\Delta T$ drops exponentially with the constant $A$.

$$\frac{\mathrm{d}\Delta T}{\mathrm{d}t} + A\Delta T = 0 \tag{5.1}$$

The area under an endothermic or exothermic peak corresponds to the change in enthalpy $\Delta H$ for the respective thermal process [Bro02].

The applied heating rate during the measurement influences the time or rather the temperature, that characterizes the maximum of the phase transition. In glass-ceramics, the position of the peak maximum in the DTA corresponds to the maximum of crystallization rate from the viscous liquid to the crystal [Kis56]. In a system where the crystal phase shows a different composition than the amorphous phase, the rate of crystallization is influenced by two factors. One of those is the diffusion rate through the liquid while the other quantity is the number of crystallization nuclei, which can be reached by the diffusion. If the number of nuclei is large (which is the case for a slow heating rate), the maximum of the DTA peak occurs at lower temperatures, where the viscosity of the material is rather high. If there are less crystallization nuclei, the maximum of the crystallization rate is only reached at higher temperatures (and lower viscosities) [NAS05]. Additionally, the geometric effects of the sample and the heating chambers play a role, because fast heating rates oftentimes result in an inhomogeneous temperature distribution within the sample material. For the DTA measurements in this thesis, a fixed heating rate of $h_r = 10\,\mathrm{K\,min^{-1}}$ has been used and $250\,\mathrm{mg}$ of an $Al_2O_3$ standard material was weighed in. The measurement device was a NETZSCH DSC 404 F1 Pegasus.

## 5.1.2. X-ray diffraction

X-ray diffraction (XRD) is a method to determine the identity, phase content, crystal size and stress or strain of phases in crystalline or semi-crystalline compounds. In a crystal, the atoms occupy periodically arranged positions on the lattice with an interatomic distance of around $\approx 1\,\text{Å}$. In order to investigate such materials, the wavelength of electromagnetic radiation used to analyze said structures should be
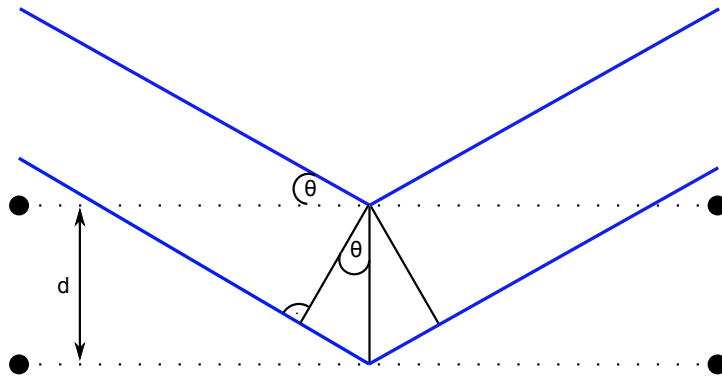
**Figure 5.3.:** Bragg condition for constructive X-ray interference

equal or smaller than this distance. Based on equation 5.2

$$\hbar\omega = \frac{hc}{\lambda} = \frac{hc}{10^{-10}\mathrm{m}} \approx 12.3 \times 10^3 \, \mathrm{eV} \tag{5.2}$$

it can easily be seen that energies, like they can be found in characteristic X-rays, fall into that category, which is the reason why they are used to resolve atomic structures. When monochromatic X-rays of a known wavelength hit the specimen to be investigated, its electrons begin to oscillate harmonically. This emits secondary radiation with the same frequency than the one from the penetrating X-rays. Since every atom in the lattice plane that gets hit by the X-rays acts as a scattering center, this leads to interference of the radiation. Constructive interference can only occur, if the path difference $2d\sin(\Theta)$ between X-rays is an integral multiple of the wavelength $n\lambda$, with $d$ being the distance between two neighboring planes. Subsequently, this leads to a condition for constructive interference and is described by Bragg's law in equation 5.3.

$$n\lambda = 2d\sin(\Theta) \tag{5.3}$$

The equation implies, that the reflex of the first order occurs at a certain angle $\Theta$ for a fixed lattice plane distance $d$ and a known wavelength $\lambda$. In order to acquire diffraction data across a broad angle area, an X-ray diffractometer can be used. It consists of an anode (mostly made of copper or molybdenum), which acts as the X-ray source. The radiation runs though a monochromator and a collimator and hits the sample material. Here, the X-rays are diffracted and the resulting radiation is measured by a mobile detector. The measurement result is a diffraction pattern with reflexes of the corresponding hkl planes in the crystal. The measured reflex intensity is cross referenced with the JCPDS (Joint Committee on Powder Diffraction Standards) database of the ICDD (International Center for Diffraction Data). By

comparing the experimental data to the reference, it is possible to obtain information on the crystal phases inside the sample material. The position of the angle dependent maxima, the reflex height and width can be iteratively fitted to a theoretical model, by minimizing the squares of the deviations of the measured and calculated intensities. This Rietveld refinement gives information on the ratio of crystal phases inside the sample. Since the X-ray diffraction is based on the diffraction on lattice planes, it is obvious, that materials or phases without a long range order (amorphous samples) will only contribute a strongly broadened peak instead of a distinguishable sharp reflex and are therefore not suitable for identification. In a glass-ceramic, which consists of one or more crystal phases and a residual glass-phase, the addition of an internal standard can be used to determine the exact crystal phase fraction using the relative ratios of the diffraction reflexes as described in section 4.5. It is important to make sure, that the main reflex of the weighed in standard does not superimpose the investigated phase as well as to chose a similar X-ray absorption as the phase of interest. In this work, a Siemens D5000 X-ray diffractometer has been used for the diffraction measurements.

### 5.1.3. Scanning electron microscopy

Scanning electron microscopy (SEM) is an examination method which allows to resolve the structure of samples which have proportions smaller than the wavelength of visible light. For this, a highly energetic electron ray is used, which runs in horizontal direction across the sample while it is slowly shifted in vertical direction. A vacuum in the machine is necessary because the filament of the cathode can be oxidized at high currents and the electron beam is supposed to reach the samples without interaction on its path. When the beam hits the sample, the electrons interact with the atoms of the sample surface. The produced signals can be read by a detector and transformed into images by a computer. When the electron beam reaches the sample, there are three main interactions that can occur. If the sample surface is scanned, highly energetic electrons hit the valence electrons of the sample. These are removed from their respective atoms and are emitted from the sample surface. These electrons, which have energies below $50\,\mathrm{eV}$, are called secondary electrons (SE). They usually originate from regions of the samples surface and the volume of a few $\mathrm{nm}$ below, which is the reason why SE detectors are suitable for depicting the sample topography with a resolution up to $1$ - $2\,\mathrm{nm}$. The second interaction method is characterized by so called backscattering electrons (high energies of several keV). If the electron beam hits the atomic nuclei in the material, the electrons are scattered inelastically, lose some of

their energy and some of them are backscattered from the sample into the detector. For that reason, they are called backscatter electrons (BSE). Backscattered electrons usually come from deeper regions of the samples than the secondary electrons. The number of backscattered electrons depends on the atomic number $Z$ of the atoms in the sample, which is why BSE detectors can give more information on the composition and chemistry of the investigated material. The interaction volume of the electron beam increases with increasing accelerating voltage $U$ and decreases with the atomic number $Z$. Because the cross section of the interaction volume in the material is always larger than the cross section of the incoming electron beam, the resolution is lower than its dimension. For the third interaction, most measurement devices offer the possibility to be equipped with an energy dispersive X-ray (EDX) detector, which is used to determine the composition of certain points on the sample. The energy of X-ray photons emitted from the sample is measured and its signal intensity is depicted depending on its energy. The combination of EDX and SEM offers the possibility to investigate the compositional details while receiving information on the structure and morphology of the sample.

### 5.1.4. SQUID

The SQUID (**S**uperconducting **QU**antum **I**nterference **D**evice) magnetometer is an effective and precise device, which is used to determine the magnetic properties of a substance. SQUID magnetometers are based on the Josephson effect and consist of a superconducting ring, which is interrupted by one (rf-SQUID) or two (dc-SQUID) insulating or regular conducting contacts. The ring is fed by a dc current $I$ (bias current) and an external magnetic flux $\Phi_a$ is passed through it due to an applied magnetic field $\vec{H} = \vec{B}/\mu_0$. From Schrödinger's equation for two weakly coupled systems $\Psi_1$ and $\Psi_2$, the supercurrent $I_s$ through the ring can be derived. It reads

$$I_s = I_1 + I_2 = I_{c1}\sin(\gamma_1) + I_{c2}\sin(\gamma_2) \tag{5.4}$$
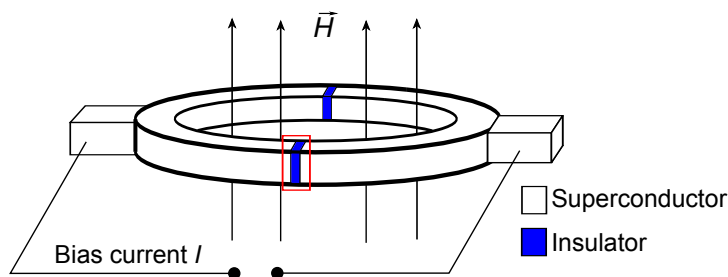


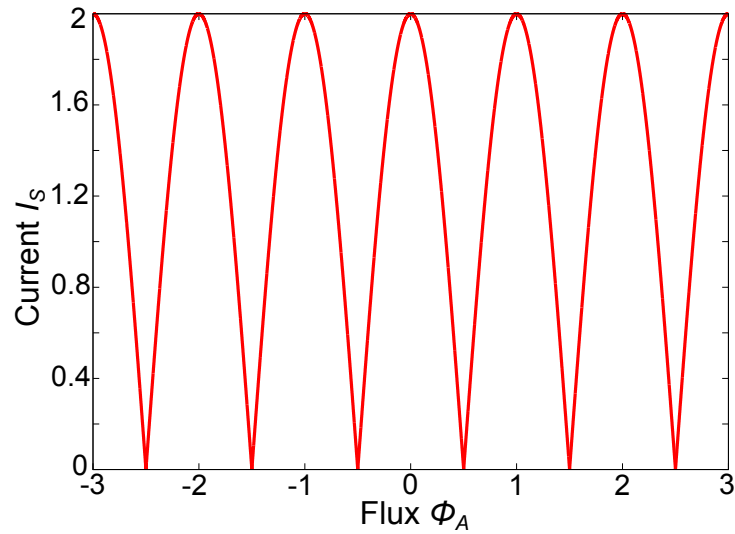**Figure 5.4.:** Schematic representation of a dc-SQUID

**Figure 5.5.:** Modulation of the maximum current in the SQUID

where $I_i$ (with $i = 1$, 2) denotes the currents through the respective arms, $I_{ci}$ the critical currents (assumed to be identical here) and $\gamma_i$ the phase shift. By choosing the right closed integration path across both Josephson junctions, an expression for the difference of the phase shifts can be obtained.

$$\gamma_2 - \gamma_1 = \frac{2\pi}{\Phi_0} \Phi_{\text{ges}} = \frac{2\pi}{\Phi_0} \left( \int B \, df + LJ \right) = \frac{2\pi}{\Phi_0} \left( \Phi_a + \underbrace{\Phi_i}_{\approx 0} \right) \tag{5.5}$$

with the flux quantum $\Phi_0 = \frac{h}{2e}$ and the enclosed flux in the ring $\Phi_{\text{ges}}$, which consists of the external flux $\Phi_a$ and the flux $\Phi_i = LJ$ generated by ring current. Assuming a small ring inductance and therefore a negligible contribution of the self induced field, trigonometric relations and the auxiliary phase $\delta = \gamma_1 + \frac{\pi \Phi_a}{\Phi_0}$, the supercurrent can be rewritten as

$$I_s = 2I_c \sin \left( \frac{\gamma_1 + \gamma_2}{2} \right) \cos \left( \frac{\gamma_1 - \gamma_2}{2} \right) = 2I_c \sin(\delta) \cos \left( \frac{\pi \Phi_a}{\Phi_0} \right) \tag{5.6}$$

The maximum of this current depending on $\delta$ reads

$$I_s = 2I_c \left| \cos \left( \frac{\pi \Phi_a}{\Phi_0} \right) \right| \tag{5.7}$$

so that the maximum supercurrent oscillates periodically with the external flux density $\Phi_a$. By this method and with the appropriate geometries, magnetic fluxes

of $\approx 10^{-6}\, \Phi_0$ can be detected by SQUIDs [1]. Dividing by the SQUID area, this corresponds to a field resolution of about $10^{-15}\, \mathrm{T/Hz^{1/2}}$ but it has to be kept in mind, that the SQUID area can not be arbitrarily enhanced, because the inductive effects of the ring would have a negative influence. For this thesis, measurements were carried out on a rf-SQUID in order to study the magnetic character in the $\mathrm{Bi_2Sr_2Co_2O_x}$ samples, which is caused by the low spin configuration in $\mathrm{Co^{4+}}$.

### 5.1.5. Thermoelectric parameters

This section will shortly discuss the derivation of the thermoelectric coefficients from Onsager's reciprocal relations after [GSZ+11]. After that, the experimental measurement techniques for the three central thermoelectric properties are presented and explained.

As already mentioned in the first chapter, thermoelectric effects are based on materials connected to reservoirs in different thermodynamic states, which induce charge and energy flow to establish a new thermodynamic equilibrium of the whole system. This is the reason why thermoelectricity has to be considered as a non-equilibrium phenomenon. However, for small differences between the states of the reservoirs, a stationary situation with finite currents is established after a short time. This implies that the intrinsic local time constants are much smaller than the time evolution of the macroscopic system itself. Based on this condition, Onsager developed a formalism which showed that for thermoelectric materials, each small but macroscopic volume $\Delta V$ can be characterized by local thermodynamic parameters. From the general concept of conservation of energy and matter the following expression for the total energy flux per unit area $J_E$ can be introduced

$$J_E = J_Q + \mu J_N \tag{5.8}$$

where $J_Q$ is the heat flux, $\mu$ the electrochemical potential and $J_N$ the particle flux per unit area. Each of these fluxes is caused by a force $F$ which can be defined by a potential gradient $\nabla\phi$. Since the corresponding potentials for the energy flux and particle flux are $\frac{1}{T}$ and $-\frac{\mu}{T}$, respectively, the currents $J_i$ for those can be expressed by a kinetic coefficient matrix

$$\begin{bmatrix} J_N \\ J_E \end{bmatrix} = \begin{bmatrix} L_{NN} & L_{NE} \\ L_{EN} & L_{EE} \end{bmatrix} \begin{bmatrix} -\nabla\left(\frac{\mu}{T}\right) \\ \nabla\frac{1}{T} \end{bmatrix} \tag{5.9}$$

---

[1] Assuming a signal integration of $t = 1\,\mathrm{s}$. The noise of the components decreases proportional with $\sqrt{(t)}$ which is why the flux resolution is oftentimes given in units of $\mathrm{flux/Hz^{1/2}}$ [Kle06]

Since the principle of minimum entropy has to be fulfilled, this requires the matrix to be symmetric ($L_{NE} = L_{EN}$). Focusing on thermoelectric quantities, the particle current and the energy current should be substituted by the heat current $J_Q$ and the charge current $J_C$ in equation 5.9. The connection between charge current and particle current are given by $J_C = e J_N$ and the link between energy current, heat current and particle current is shown in equation 5.8. By using $\nabla \frac{1}{T} = -\frac{1}{T^2} \nabla T$, the matrix changes to

$$\begin{bmatrix} J_C \\ J_Q \end{bmatrix} = \begin{bmatrix} L_{11} & L_{12} \\ L_{21} & L_{22} \end{bmatrix} \begin{bmatrix} -\nabla\left(\frac{\mu}{e}\right) \\ -\nabla T \end{bmatrix} \tag{5.10}$$

with

$$L_{11} = \frac{e^2}{T} L_{NN} \tag{5.11}$$

$$L_{12} = \frac{e}{T^2}(L_{NE} - \mu L_{NN}) \tag{5.12}$$

$$L_{21} = \frac{e}{T}(L_{NE} - \mu L_{NN}) \tag{5.13}$$

$$L_{22} = \frac{1}{T^2}(L_{EE} + \mu^2 L_{NN} - \mu L_{NE} - \mu L_{EN}) \tag{5.14}$$

In equation 5.10 the off-diagonal entries are linked by $L_{12}T = L_{21}$: Since the fluxes are not expressed as a function of their corresponding thermodynamic potentials this is not violating the requirement of symmetry. Furthermore, equation 5.10 now provides the connection between the coefficients $L_{nm}$ and the thermoelectric properties $\sigma$, $S$ and $\kappa$. Since the electric field $E$ and the chemical potential $\mu$ are related by $E = -\frac{\nabla\mu}{e}$, the case of $\nabla T = 0$ gives the following expressions from equation 5.10

$$J_C = L_{11}E \tag{5.15}$$

$$J_Q = L_{21}E \tag{5.16}$$

With $L_{11} = \sigma$, equation 5.15 represents Ohm's law. Combining equation 5.15 and 5.16 yields

$$J_Q = \frac{L_{21}}{L_{11}} J_C \tag{5.17}$$

This describes the Peltier effect, if the quantity $\frac{L_{21}}{L_{11}}$ is identified as the Peltier coefficient $\Pi$. If zero current is assumed ($J_C = 0$), then equation 5.10 gives

$$0 = L_{11}E + L_{12}(-\nabla T) \tag{5.18}$$

$$J_Q = \left(L_{22} - \frac{L_{12}L_{21}}{L_{11}}\right)(-\nabla T) \tag{5.19}$$

61

| Thermoelectric coefficient | Transport parameter |
|:---:|:---:|
| $\sigma$ | $L_{11}$ |
| $S$ | $\frac{L_{12}}{L_{11}}$ |
| $\Pi$ | $\frac{L_{21}}{L_{11}}$ |
| $\kappa$ | $L_{22} - \frac{L_{12}L_{21}}{L_{11}}$ |
| $\kappa_0$ | $L_{22}$ |

**Table 5.1.:** Comparison of TE coefficients and transport parameters

From the definition of the Seebeck coefficient, it can be deduced that $S = \frac{E}{\nabla T} = \frac{L_{12}}{L_{21}}$. Finally, equation 5.19 depicts Fourier's law, if $\kappa$ is associated with $L_{22} - \frac{L_{12}L_{21}}{L_{11}}$. With this, the matrix coefficients and their corresponding thermoelectric properties can be summarized in table 5.1 where $L_{22}$ was named $\kappa_0$ for reasons of convention. By having derived these relationships, equation 5.10 can be expressed by

$$\begin{bmatrix} J_C \\ J_Q \end{bmatrix} = \begin{bmatrix} \sigma & \sigma S \\ \sigma \Pi & \kappa_0 \end{bmatrix} \begin{bmatrix} E \\ -\nabla T \end{bmatrix} \tag{5.20}$$

Since $L_{12}T = L_{21}$, the relation between $S$ and $\Pi$ can be easily obtained as $ST = \Pi$ in accordance with equation 1.19. This gives an intuitive interpretation of the effects, since the Peltier coefficient can be considered as the average heat per charge carrier, whereas the Seebeck coefficient can be interpreted as the average entropy per charge.

**Electrical resistivity**

The resistivity $\rho$ is an intrinsic property which describes how a material opposes the electrical current. It is usually given in units of $\Omega$cm. Its reciprocal value is the electrical conductivity $\sigma$ which characterizes the possibility to conduct a current. To measure the conductivity, the sample is contacted and a current $I$ is sent through to measure the voltage drop $U$. This can be done using two or four contacts, whereas the advantage of four-terminal sensing is the elimination of the contact resistance (see figure 5.6 and 5.7). By separating the current and voltage measurement (assuming an infinite internal resistance of the voltmeter), the voltage drop across the contact resistances is negligible, the measured voltage signal is therefore a direct measure for the sample resistance without external influences of the contacts. This method is favorable if the measured samples show a small resistance, because for those the contact resistance has the strongest impact. In this work, the four-terminal sensing method was used for most samples.
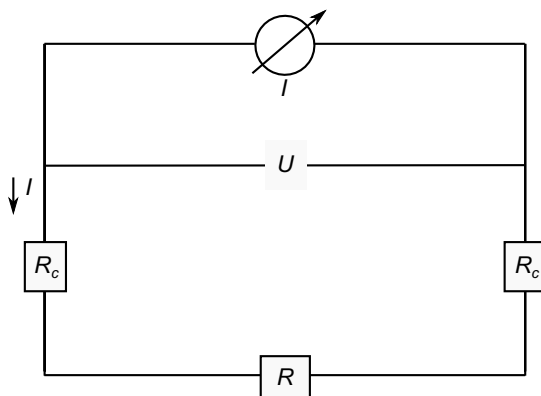
$$U = R \cdot I + 2R_c \cdot I$$
$$\Rightarrow R_{total} = 2R_c + R$$

**Figure 5.6.:** Resistance measurement 2-contacts
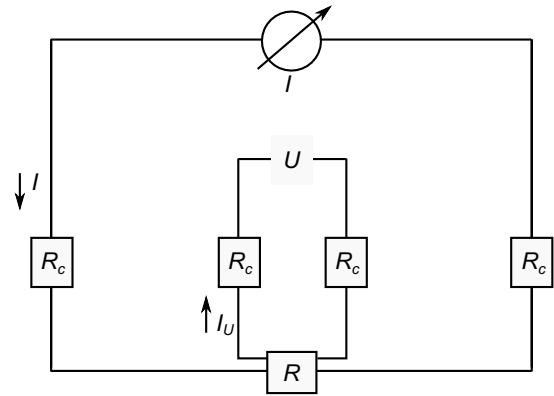
$$U = R \cdot I + 2R_c \cdot I_U, \ I_U \ll I$$
$$\Rightarrow R = U/I$$

**Figure 5.7.:** Resistance measurement 4-contacts

**Seebeck coefficient**

When measuring the Seebeck coefficient, it is of great importance to measure the Seebeck voltage $U_S$ as well as the applied temperature difference $\Delta T$ accurately. For that, the sample is contacted with thin Pt-Pt/Rh thermocouples (see also chapter 5.4.1) and fixed in a holder within a glass bulb using a spring. Using a pressure pump, a flow of air is brought on one side of the sample. The temperature in the glass bulb with the sample can be increased with a heating chamber, while the airflow maintains a temperature gradient $\Delta T$ across the sample. The temperature $T$ as well as the voltage $U_S$ can be measured via the thermocouples on the sample sides. For each measurement point, at least four different temperature gradients with $\Delta T = 3 - 8\,\mathrm{K}$ are generated, the Seebeck coefficient can be obtained from a fit of the thermopower across the respective temperature difference. It is important to note, that the Seebeck effect also occurs in the thermocouples during the measurement. Therefore, the measured voltage signal can not be directly related to the Seebeck coefficient of the sample but rather to the sum $S_{\mathrm{sample}} + S_{\mathrm{contact}}$ of sample and thermocouple. The Seebeck coefficient of the Pt-Pt/Rh thermocouple has to be taken into account and subtracted during the analysis of the data.

**Thermal conductivity**

The thermal properties of material can be determined, if a boundary value problem with heat flux is simulated in the experiment. By solving the theoretical equations and measuring the necessary temperatures, the thermal quantity can be obtained by comparison. In order to measure the thermal conductivity $\kappa$, a stationary, linear

heat flux across the material can be generated and treated by means of the Fourier equation. This method is rather time-consuming and prone to errors, if the boundary conditions can not be recreated precisely. Especially for bulk materials, it is more meaningful to measure the thermal diffusivity $\alpha$ by the laser flash method (developed by W. Parker et al. [PJBA61]), in order to eliminate the necessary stationary condition by measuring a $T - t$ signal instead. In this method, a short laser pulse heats up the upper side of a thin, parallel sided sample (see figure 5.8). The time for the heat to
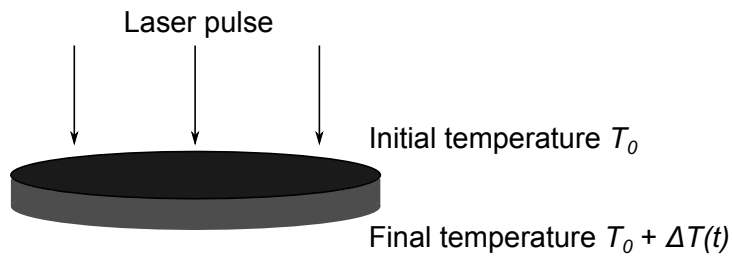


**Figure 5.8.:** Schematic illustration of the laser flash method

propagate through the sample and to cause a rise in temperature on the opposing side can be used to calculate the diffusivity $\alpha$ and finally the thermal conductivity $\kappa$ by using equation 5.21, if the density $\rho$ and the specific heat $c_p$ are known.

$$\kappa = \alpha \, c_p \, \rho \tag{5.21}$$

A typical laser flash signal is shown in figure 5.9. At the beginning, the sample's
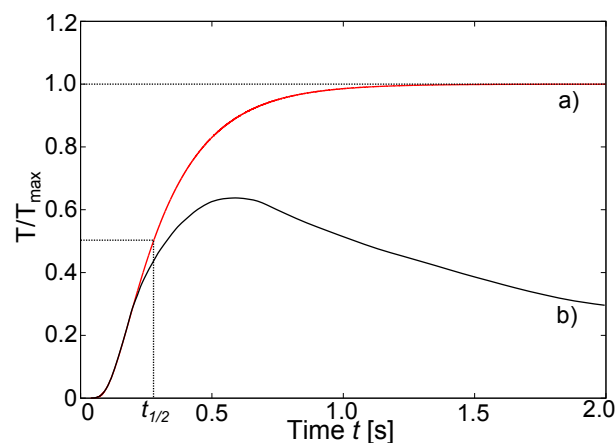


**Figure 5.9.:** Laser flash signal, a) ideal, loss-free slope / b) real slope

environment has a homogeneous temperature distribution. After the laser flash, the front side of the sample has a higher temperature than its back side. Because the sample is designed to be very thin and largely extended, the resulting heat flux can be assumed to be parallel to the laser and one-dimensional. If it is assumed that no heat

loss occurs, the time-dependent temperature increase can be obtained from equation 5.22

$$T(d,t) = T_{max} \left( 1 + 2 \sum_{n=1}^{\infty} (-1)^n \exp \left( -\frac{n^2 \alpha \pi^2 t}{d^2} \right) \right) \tag{5.22}$$

and the thermal diffusivity from equation 5.23, whereas $d$ and $t_{1/2}$ denote the sample thickness and the time, until the sample's back side has reached 50% of its maximum temperature.

$$\alpha = \frac{0.139 \, d^2}{t_{1/2}} \tag{5.23}$$

The specific heat $c_p$ can also be determined by the flash method, if the rise in temperature of the sample is compared with the temperature increase of a reference with a known specific heat (under equal conditions).

$$c_p = \frac{Q}{m \Delta T} \tag{5.24}$$

Assuming the absorption of the laser pulse is the same for both samples, the heat can be expressed as

$$Q_{\text{Laser}} = (m c_p \Delta T)_{\text{ref}} = (m c_p \Delta T)_{\text{sample}} \Rightarrow c_p = \frac{(m c_p \Delta T)_{\text{ref}}}{(m \Delta T)_{\text{sample}}} \tag{5.25}$$

For each measurement point, several laser flashes are used, so it can be assumed, that the deposited heat energy in the sample and in the reference is the same on average. For this work, laser flash devices of Netzsch (LFA 457) (EMPA, Switzerland and Johannes Gutenberg-Universität, Mainz) as well as ULVAC (TC-9000) (AIST, Ikeda) have been used.

## 5.2. Glass-ceramics

In order to conceptualize a development of glass-ceramic materials for thermoelectric purposes, it is important to be aware of the fact, that even in an ideal case, a material will be obtained, which consists of two different phases. One of those phases will be the desired crystal phase, which determines the thermoelectric properties and should therefore have a high phase content. On the other hand, a certain amount of amorphous, residual glass phase will remain, which is only supposed to reduce the thermal conductivity and increase the chemical durability. This is the ideal case and in practice, the synthesis of a new system is much more complex. In the diploma thesis of [Lin11], first glass-ceramic materials for thermoelectric applications, based on

a $SiO_2$-$Al_2O_3$-$B_2O_3$ system with a main phase of Nb-doped $SrTiO_3$, have been studied and characterized concerning their thermoelectric properties (figure 5.1). It could be demonstrated, the these samples reach a high Seebeck coefficient $S$, a low thermal conductivity $\kappa$ and a desirable temperature cycling. The obtained values for two n-type $SrTiO_3$ containing glass-ceramic systems, which have been developed, are listed in table 5.2. Unfortunately, these samples could only be obtained in small quantities

| Sample | Temperature $T$ [K] | $S$ [µV K$^{-1}$] | $\sigma$ [S cm$^{-1}$] | $\kappa$ [W m$^{-1}$ K$^{-1}$] |
|---|---|---|---|---|
| TE10-13 | 897.15 | -508 | $1 \times 10^{-2}$ | 1.85 |
| TE62 | 897.15 | -480 | $8 \times 10^{-2}$ | 1.60 |

**Table 5.2.:** Thermoelectric parameters of glass-ceramic samples

($V \approx 30\,\mathrm{ml}$ each) due to difficult meltability of the glasses, which led to insufficient homogeneity. Aluminum containing crystalline secondary phases and an insufficiently high amount of the main crystal phase made it impossible to reach a good electrical conductivity $\sigma$ for thermoelectric purposes. New motivation to continue to work on this system came from density functional theory (DFT) calculations on different supercells of single crystal $SrTiO_3$. These band structure calculations could show, that a certain amount of oxygen vacancies in the material leads to a significant increase of the electrical conductivity and has an even bigger influence on its enhancement than heterovalent doping on the Sr or Ti site (see comparable results in [BRRM$^+$14]). Therefore, the goal of this thesis was to target those challenges and to develop a more homogeneous system, which can be optimized by different ceramization experiments, so that a single phase glass-ceramic with favorable thermoelectric properties can be obtained. As the starting point for the sample preparation, phase diagrams of the systems have been used to assess the compositional areas for easy glass formation.
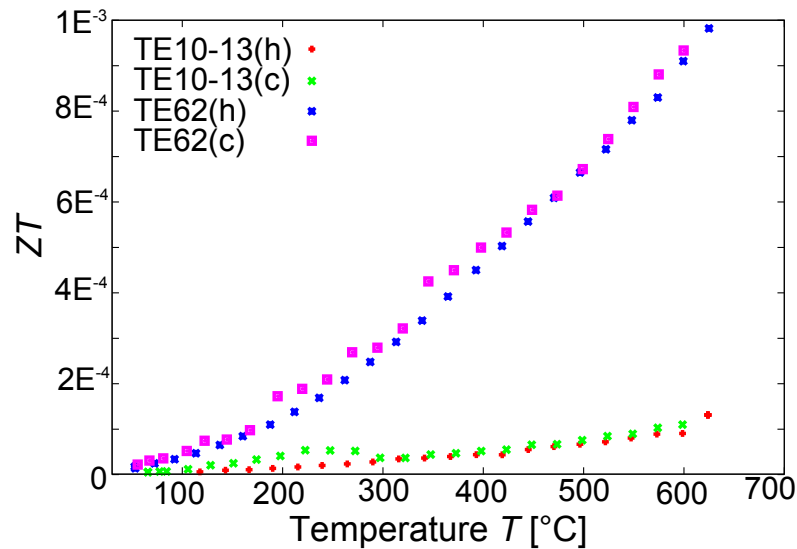
**Figure 5.10.:** *ZT* comparison of initial (TE10-13) and improved (TE62) glass-ceramic
material [Lin11], (h)=heating, (c)=cooling

## 5.2.1. Phase diagrams

In order to get an idea of the expected meltability of a glass in a certain compositional
range, it is beneficial to study the phase diagrams of the respective systems. A phase
diagram illustrates the correlation between physical quantities like temperature $T$
and pressure $p$ and the state of the material in a broad compositional range. Strictly
speaking, the phase diagram is only applicable to states of thermal equilibrium,
which is not possible in glasses due to their nature. However, by using extrapolated
eutectic lines and points in the diagram, it is at least possible to make a reasonable
assumption, which composition is most likely to avoid devitrification of the melt in
the experiment, since eutectic points symbolize areas of low melting temperature. An
example for such a phase diagram is shown in figure 5.11. The treated system is
SrO-TiO$_2$-B$_2$O$_3$, which has been the basis of the n-type glass-ceramic development.
Binary phases of the system can be found at the sides of the diagram, while the glass
forming area on the SrO-B$_2$O$_3$ rich side of the diagram can be seen within the glass
formation border on the right side. It has to be kept in mind, that this is a rather
simple system which consists only of three components. Adding more components
makes the system become more complex and less clear, since additional axes have to
be added to account for them. If additional components behave similarly to one of
the available components in the phase diagram (e. g. Nb$^{5+} \,\hat{=}\,$ Ti$^{4+}$), they are treated
as if their respective amount can be added to the concerning compound. By doing
this, a rough estimate of the area in complex systems, where experimental melts can
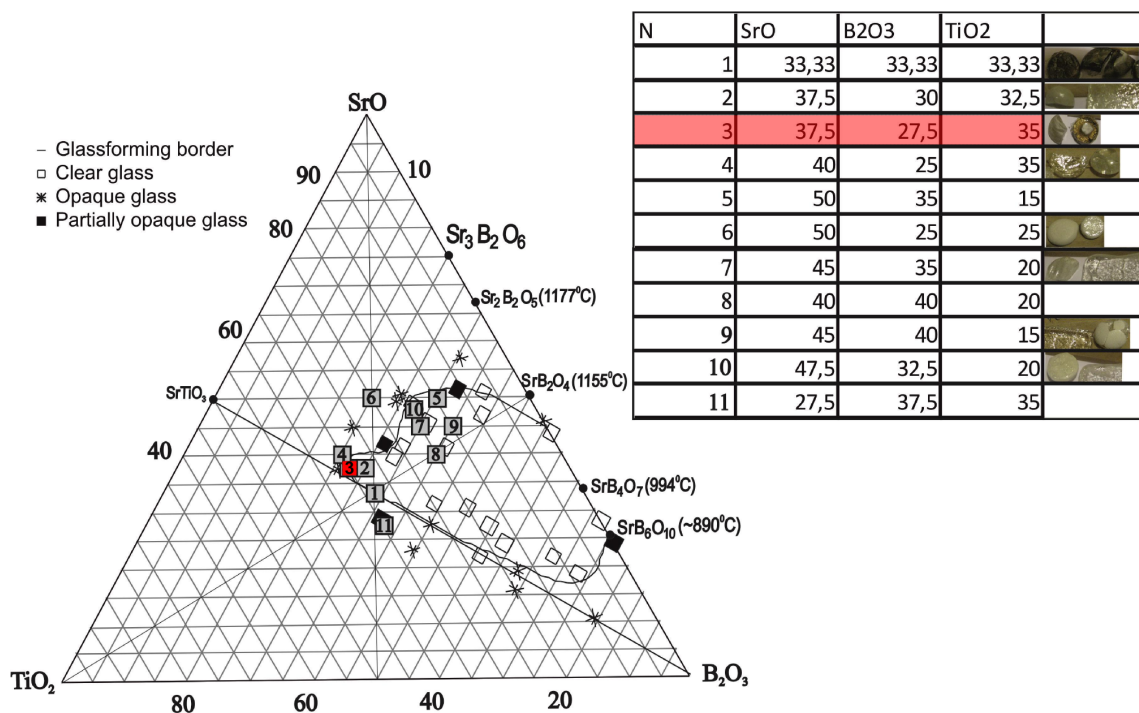be carried out and analyzed, can be made.

| N | SrO | B2O3 | TiO2 | |
|---|---|---|---|---|
| 1 | 33,33 | 33,33 | 33,33 | |
| 2 | 37,5 | 30 | 32,5 | |
| 3 | 37,5 | 27,5 | 35 | |
| 4 | 40 | 25 | 35 | |
| 5 | 50 | 35 | 15 | |
| 6 | 50 | 25 | 25 | |
| 7 | 45 | 35 | 20 | |
| 8 | 40 | 40 | 20 | |
| 9 | 45 | 40 | 15 | |
| 10 | 47,5 | 32,5 | 20 | |
| 11 | 27,5 | 37,5 | 35 | |

**Figure 5.11.:** Phase diagram SrO-TiO$_2$-B$_2$O$_3$ system, composition in mol% [Hov11]

## 5.2.2. Suppression of secondary phases

As it could be shown in [Lin11], unwanted secondary phases in glass-ceramic systems can lead to severe deterioration of the material properties. For electrically conductive systems this can lead to a decrease in conductivity, because the secondary phases usually had insulating properties. Because the phase formation is generally preceded by a nucleation process, the dynamics of the reaction can allow to quickly pass the nucleation region and therefore to suppress the secondary phase formation. Furthermore, the variation of the composition can help to adjust the content, so certain components of the secondary phases decrease or stop being available at all, which inhibits their formation. For the development of a single phase SrTiO$_3$ glass-ceramic system, both mechanisms are applied.

## 5.2.3. SrTiO$_3$ as an n-type system

In [Lin11] the decision to choose SrTiO$_3$ as the main crystal phase for a thermoelectric, n-type glass-ceramic system was made, because SrTiO$_3$ is one of the most popular and promising ceramic n-type oxide systems. Choosing SrTiO$_3$ for the glass-ceramic is therefore suited, because it can act as a model system and be compared with its ceramic equivalent. At room temperature, SrTiO$_3$ has a cubic unit cell with the space group Pm3m (221), a lattice constant of $a = 0.3901\,\text{nm}$ and a density of $\rho = 5.118\,\text{g\,cm}^{-3}$.
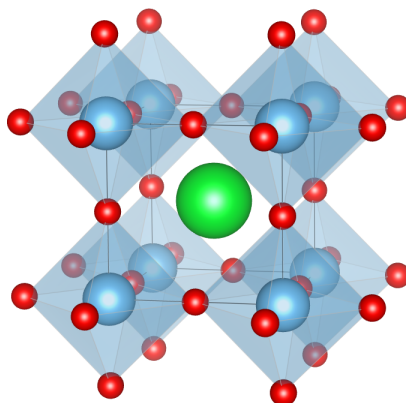
**Figure 5.12.:** Unit cell of $SrTiO_3$, Sr (green), O (red), Ti (blue), image created with *VESTA* [MI11]

It is an isolator with a band gap of $E_g = 3.2\,eV$ [vBEF01]. Heterovalent doping with impurities on the Sr or Ti site can shift the Fermi energy towards the conduction band, which enables the transition to a semiconductor (see 5.13 and 5.14 redrawn from [Lin11]). An alternative attempt to develop a different single phase glass-ceramic system with a high content of ZnO as a main crystal phase was not successful, because the glass forming region in the phase diagram of $SiO_2$-$Al_2O_3$-ZnO [HZHJ05] was too small to yield clear glasses. Therefore, this work focused solely on $SrTiO_3$ concerning the n-type leg.
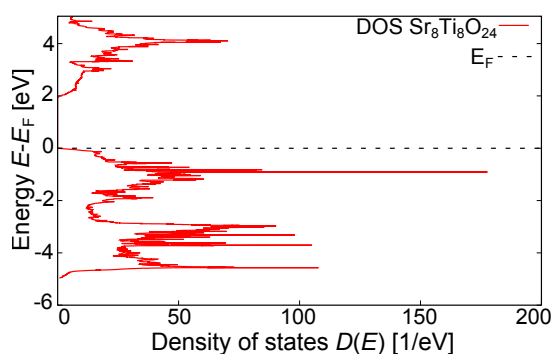


**Figure 5.13.:** Density of states of $Sr_8Ti_8O_{24}$ (undoped)
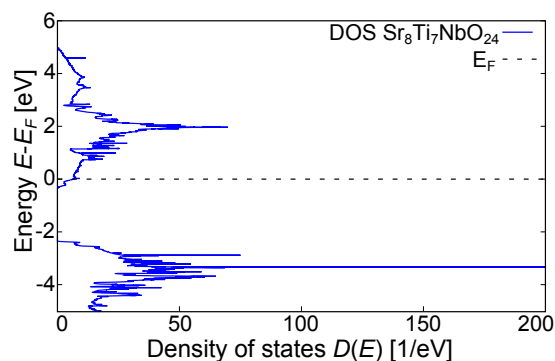


**Figure 5.14.:** Density of states of $Sr_8Ti_7NbO_{24}$

**Modification of the basic composition**

The literature as well as the obtained data of the former $SiO_2$-$Al_2O_3$-$B_2O_3$ glass-ceramic suggested, that even small amounts of $Al_2O_3$, which were added to modify the glass structure to improve its meltability, led to the development of the secondary phase $SrAl_2Si_2O_8$. Not only does this phase have less desirable electrical properties

than SrTiO$_3$, it also hinders some of the weighed-in Sr to be available for the formation of the main phase. In order to make the first step towards the new development in this work, a modified glass composition had to be found, which did not contain any Al$_2$O$_3$ but which had the possibility to obtain SrTiO$_3$ as a main phase. Based on a series of experiments from [Hov11], a region in the system of SrO-TiO$_2$-B$_2$O$_3$ could be found where it was possible to obtain glassy samples. As stated before, the work of [Hov11] presented a ternary phase diagram, which had to be modified to account for the correct doping of the main phase (e.g. doping of Nb on the Ti site and an attempt to dope Y on the Sr site).

Based on this system (see red mark in figure 5.11), a first series of melting experiments was started, in which B$_2$O$_3$ was the only glass former. The content of B$_2$O$_3$ was varied and it was tried to receive a glass with a low content of glass forming oxides (and therefore high content of SrTiO$_3$). The compositions of the main two melts in this system are shown in table 5.3 These glasses could be melted in a Pt-

| Component | 38685 [mol%] | 38688 [mol%] |
|---|---|---|
| B$_2$O$_3$ | 27.5 | 27.5 |
| TiO$_2$ | 31.1 | 35 |
| SrO | 37.5 | 35.7 |
| Nb$_2$O$_5$ | 3.9 | 0 |
| Y$_2$O$_3$ | 0 | 1.8 |

**Table 5.3.:** Composition of B$_2$O$_3$ glasses

Ir crucible (30 ml) at $T = 1600\,°C$ and casted without devitrification and were chosen for further characterization. Glasses with a B$_2$O$_3$ fraction of under $27.5\,mol\%$ showed strong bulk crystallization and were not considered furthermore. After the controlled cooling of the glass samples, a differential thermal analysis was carried out on these samples. The obtained data from the measurements is presented in figure 5.15 and 5.16. Besides the inflection point in sample 38685, there is a clear exothermic peak at
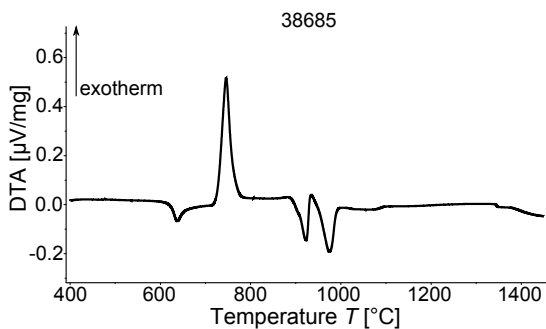
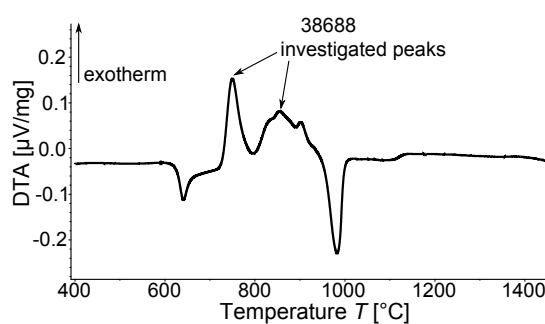

**Figure 5.15.:** DTA of glass 38685
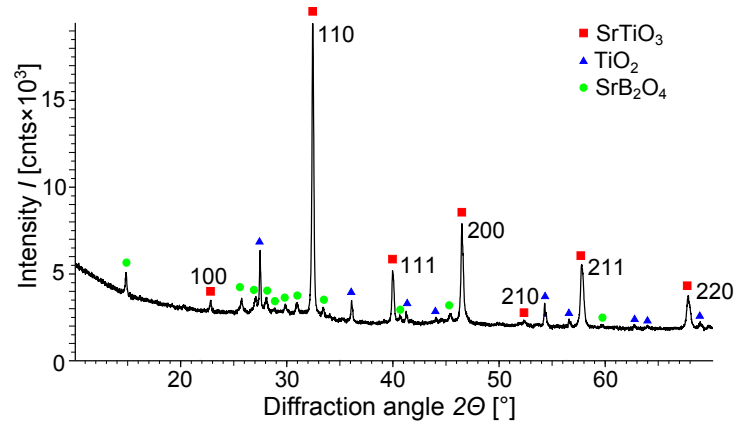


**Figure 5.16.:** DTA of glass 38688

**Figure 5.17.:** X-ray diffractogram of TE85 (glass 38688, ceramized at second temperature peak)

$T = 746\,°C$. At higher temperature, there are two different, endothermic dips. Because these temperatures are too low to be associated with the melting temperature of the glass itself, they denote temperatures, where some of the existing crystal phases are decomposing. Because the temperatures are separated far enough from each other, it is assumed that they characterize two different crystal phases and the growth of one of those did not show up as an exothermic peak before. In sample 38688, an exothermic peak in the lower temperature regime ($T = 750\,°C$) as well as a broadened peak at higher temperatures ($T = 855\,°C$) can be observed. Since it is known from comparable systems of [Lin11], that in this temperature region the crystallization of the main phase $SrTiO_3$ takes place, the ceramization temperature for sample 38685 was chosen to be the same as the one where the single peak appeared. One piece of sample 38688 was ceramized at a temperature corresponding to the first peak in figure 5.16, a second piece at a temperature corresponding to the second peak. After the ceramization, the brownish, transparent glass changed its color to white and became opaque. X-ray measurements on the samples showed the diffraction reflexes of different, crystalline phases in the material (exemplarily shown in figure 5.17). As a result of this, in all three samples a main phase of $SrTiO_3$ (JCPDS 35-0734) could be found. However, in all cases there was at least one secondary phase in addition to the remaining amorphous content. In sample 38685, the Sr rich phase $Sr_5Nb_4O_{15}$ (JCPDS 48-0421) could be found, while the secondary phase in 38688 could not be determined for the first ceramization. In the ceramization on the second peak, the resulting secondary phase was $SrB_2O_4$ (JCPDS 84-2175, compare to phase diagram in figure 5.11).

Even though the X-ray diffraction measurements suggested a strong inhomogeneity, samples were prepared from the materials, which were measured concerning their

electrical conductivity. The resulting values were around $\sigma = 4\times10^{-10}\,\mathrm{S\,cm^{-1}}$, so the conductivity was far from any desired values. It can be speculated, that the relatively high content of $B_2O_3$ as well as the secondary phases in the material had a strong insulating influence on the overall electrical properties. Since the boron-containing secondary phase showed a separate ceramization temperature compared to the aluminum-containing secondary phase of [Lin11], the basic idea of a boron-containing composition was kept and tried to optimize by a variation of the glass formers.

**Glass-ceramic with a single phase and heating variations**

In order to implement the previous conclusion in the next experiments, $SiO_2$ was added as an additional glass former to the composition to support the disorder and promote the glass forming ability as well as to be able to reduce the $B_2O_3$ content and still receive a clear glass. For this, the former $\sim 28\,\mathrm{mol\%}$ of $B_2O_3$ were redistributed with a ratio of 60/40 to $SiO_2$ and $B_2O_3$. This ratio was chosen, based on a phase diagram from [FAC], because it showed a liquidus temperature around $1000\,^\circ C$ which is well below the regular casting temperature of $1600\,^\circ C$ and should reduce the probability of an early devitrification. From this altered batch, composition number 38690 was melted (see table 5.4) which yielded a clear glass. The DTA showed a broad, exothermic peak at $T = 910\,^\circ C$ (see figure 5.18). After ceramization, X-ray diffraction measurements as well as conductivity measurements on the samples were carried out. The result was, that the modification of the batch composition led to a system, in which it was possible to obtain a single-phase (see figure 5.19) glass-ceramic. Small amounts of $SiO_2$ (JCPDS 33-1161) could be identified, which are thought to be residuals from the sample preparation. Concerning the electrical conductivity measurement, a value of $\sigma = 10^{-5}\,\mathrm{S\,cm^{-1}}$ could be reached which is a great improvement compared to the previous results but still too far from values of

| Component | 38690/39972 [mol%] |
|---|---|
| $SiO_2$ | 16.90 |
| $B_2O_3$ | 11.54 |
| $TiO_2$ | 30.30 |
| $SrO$ | 35.61 |
| $Sb_2O_3$ | 0.10 |
| $Nb_2O_5$ | 3.79 |
| $Y_2O_3$ | 1.76 |

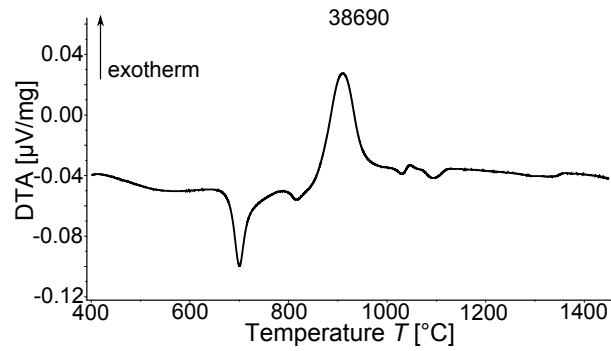**Table 5.4.:** Composition of glass 38690 ($30\,\mathrm{ml}$) and 39972 ($1\,\mathrm{l}$)

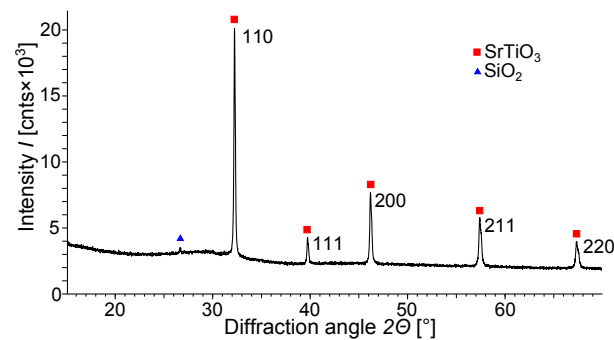**Figure 5.18.:** DTA of glass 38690



**Figure 5.19.:** X-ray diffractogram of TE92 (glass 38690)

comparable ceramic equivalents. However, the success to be able to obtain a glass-ceramic material with a single, main phase was a motivation to continue to enhance the system's properties. The next thought was to upscale the melting volume in order to receive larger amounts of material, which would enable systematic ceramization experiments to study the influence on the properties. Additionally, the formerly used crucibles of $30\,\mathrm{ml}$ lacked the possibility of stirring during the melting down, which hindered the homogenization. For this reason, composition 38690 was remelted in a crucible with a volume of $V = 1470\,\mathrm{ml}$ (sample 39972). This up-scaling process did not show any differences in melting behavior and larger amounts of glass could be obtained as intended.

The electrical conductivity of the glass itself was measured, to determine the starting point for the following improvements of the conductivity. The fit to the data in figure 5.20 shows the expected power law correlation between frequency $f$ and conductivity $\sigma$ for glasses according to the hopping model (see [PP72]).

$$\sigma_{AC}(f) = \sigma_{DC} + \sigma_0 f^s \tag{5.26}$$

Here, $\sigma_{DC}$ denotes the direct current part of the conductivity while $\sigma_0$ and $s$ are a pre-exponential factor and the exponent of the dispersion part of the conductivity.
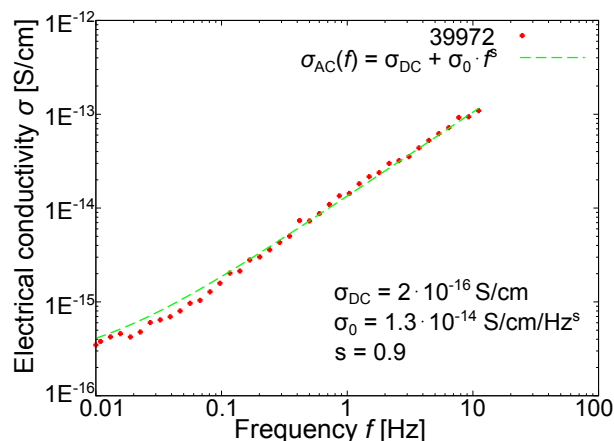
**Figure 5.20.:** Electrical conductivity of glass 39972 with fit according to [Jon77]

The hopping model describes the charge transport as a thermally activated hopping or quantum mechanically tunneling of the localized charge carriers in the material between different impurity sites. The hopping probability depends on the height of the energy barrier and the hopping distance between the sites. At high frequencies, the movement of the charge carriers is only happening between two close neighboring sites because of the limited time for this process. With a decrease in frequency, the time for the charge carriers to go in one direction increases and so does the probability to encounter a high energy barrier, which lowers the hopping probability which subsequently lowers the electrical conductivity.

The DTA of 39972 showed a nearly identical slope as 38690 (figure 5.18), which had to be expected, because the composition was the same. Because of the abundance of the material, first experiments to determine the influence of the ceramization on the electrical conductivity were carried out. Subsequently, glass samples of composition 39972 were subjected to different heating programs in a muffle furnace. It was thought that a fast heating rate would lead to bigger crystals, because sharp heating rates decrease the amount of crystallization nuclei. This should correlate with the electrical conductivity, because it is expected to be higher in larger crystals (see [Fu00]). As can be seen from the diffractograms in figure 5.21 and 5.22, the heating rate does not significantly influence the resulting phases in the XRD. All 7 samples show main reflexes of $SrTiO_3$ (JCPDS 35-0734) and a small reflex of $SiO_2$ (JCPDS 33-1161), which is again an impurity from the sample preparation. Measurements of the electrical conductivity on samples KTE8 - KTE14 could not show the expected trend of increasing conductivity with increasing heating rate (see figure 5.23). The conductivity increased only incrementally with increasing heating rate and due to inhomogeneities and measurement uncertainties, the error is estimated to be around

| Sample | $h_1$ [K min$^{-1}$] | $T_1$ [°C] | $h_2$ [K min$^{-1}$] | $T_2$ [°C] | $dt$ [h] | $\sigma$ [S cm$^{-1}$] |
|--------|------|------|------|------|------|------|
| KTE-8  | 50 | 700 | 5  | 895 | 1 | 5.9E-4 |
| KTE-9  | 50 | 700 | 10 | 895 | 1 | 5.2E-4 |
| KTE-10 | 50 | 700 | 15 | 895 | 1 | 4.4E-4 |
| KTE-11 | 50 | 700 | 20 | 895 | 1 | 1-0E-3 |
| KTE-12 | 50 | 700 | 30 | 895 | 1 | 1.5E-3 |
| KTE-13 | 50 | 700 | 40 | 895 | 1 | 1.3E-3 |
| KTE-14 | 50 | 700 | 50 | 895 | 1 | 1.4E-3 |

**Table 5.5.:** Program of the first ceramization run, $h_i$ = heating rate, $dt$ = dwell time, $\sigma$ = electrical conductivity
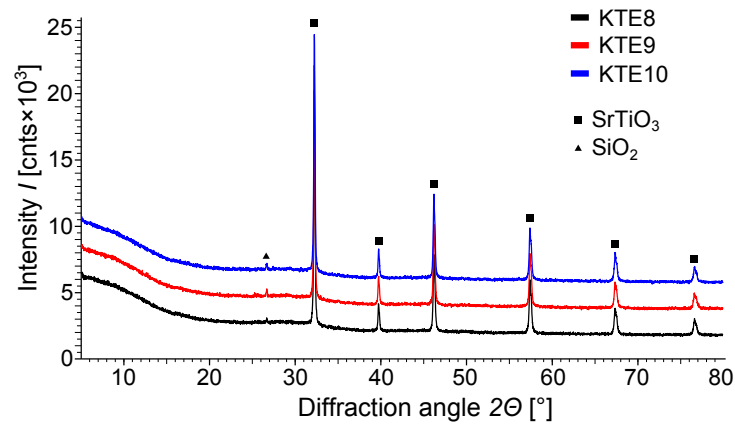


**Figure 5.21.:** X-ray diffractogram of KTE8, KTE9 and KTE10

20 % which is too high in order to make a clear statement to the question if there is a real connection. Sample KTE11 was measured temperature dependently, which is shown in figure 5.24. Assuming the conductivity in the glass-ceramic systems can be described by a hopping of electrons between localized states (see [Mot68]), the conductivity can be expressed by equation 5.27.

$$\sigma = \underbrace{\frac{\nu_0 e^2 C(1-C)}{k_B T R} \exp(-2\alpha R)}_{\sigma_0 \frac{1}{T}} \exp\left(-\frac{E_A}{k_B T}\right) \tag{5.27}$$

In this, $\nu_0$ is the characteristic phonon frequency, $\alpha$ is the rate of decay of the wave function, $C$ is the ratio of ions in the low valence state to the total concentration of transition metal ions, $R$ is the average hopping distance and $E_A$ the activation energy for the hopping process. Using the Arrhenius equation 5.28

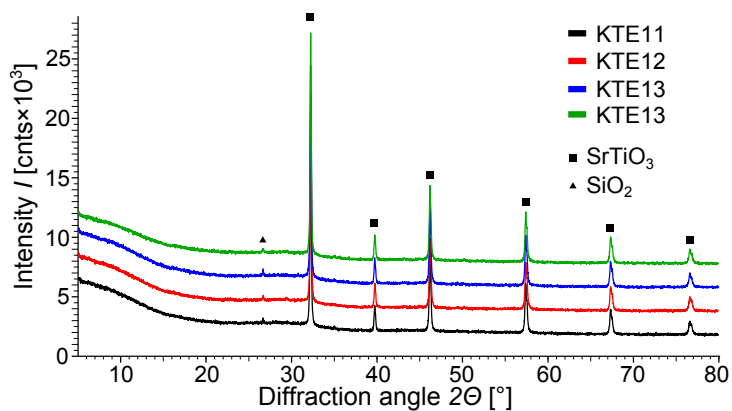$$\sigma T = \sigma_0 \exp\left(-\frac{E_A}{k_B T}\right) \tag{5.28}$$

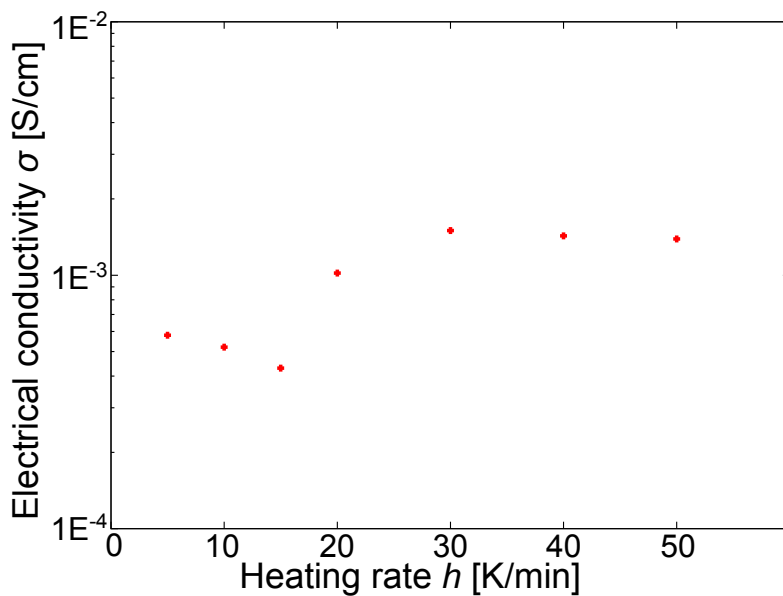**Figure 5.22.:** X-ray diffractogram of KTE11, KTE12, KTE13 and KTE14



**Figure 5.23.:** Correlation of heating rate $h$ and electrical conductivity $\sigma$ in glass-ceramic samples
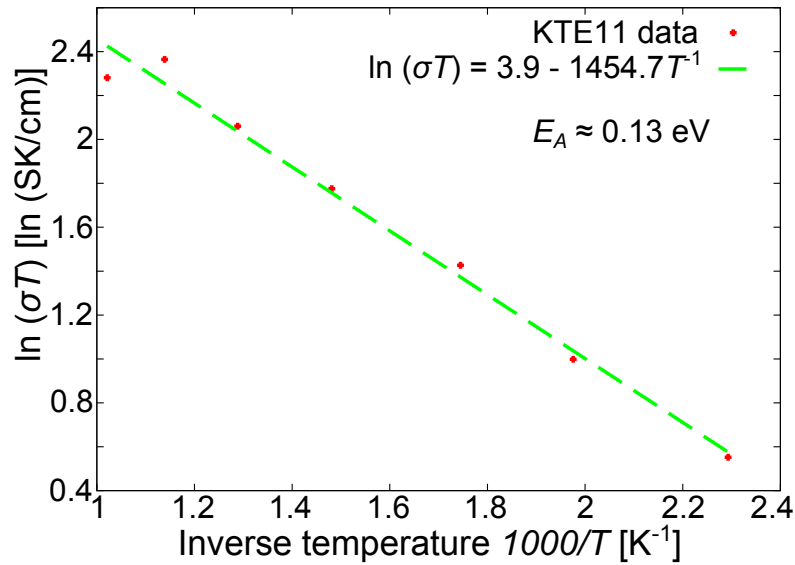
**Figure 5.24.:** Temperature-dependent electrical conductivity $\sigma$ of sample KTE11 with Arrhenius Fit

the data was fitted in order to calculate the activation energy $E_A$ in this material using the Boltzmann constant $k_B$. The fit yielded an activation energy of $E_A = 0.13\,\text{eV}$, which is rather low and comparable to solid electrolytes ($\beta$-alumina $E_A = 0.15\,\text{eV}$ [Bru97]). The measurement showed an increase of the conductivity with increasing temperature, but the maximum conductivity of $\sigma \approx 0.01\,\text{S}\,\text{cm}^{-1}$ at $T = 900\,\text{K}$ was still below the expectations.

**Reducing atmosphere during melting**

Since the heating rate seemed to have only a subordinate influence on the electrical conductivity, it was tried to create reducing conditions during melting in order to incorporate oxygen vacancies into the material thus increasing its conductivity. This assumption was (amongst others) based on density functional theoretical calculations of the density of states of different supercells of $SrTiO_3$ [Lin11]. Using a high temper-
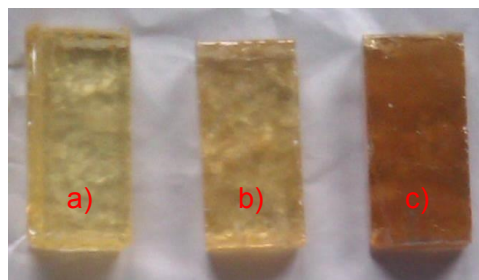


**Figure 5.25.:** Glass 39972 (a), 41972 (b) and 42073 (c) before ceramization

ature approximation and the assumption of parabolic bands, it could be shown, that the electrical conductivity increased, when oxygen defects were simulated compared to heterovalently doped cells. In order to generate these conditions, the melting of the former glass was repeated but with an addition of $0.1\,\mathrm{wt\%}$ graphite (41972) and at elevated temperatures around $T = 1680\,^\circ\mathrm{C}$ (42073). The resulting glasses for 41972 and 42073 showed a distinguishable color difference compared to the original glass 39972, most likely due to an enhanced $Ti^{3+}$ content. In the case of 42072 this was also due to the used crucible material of Pt-Rh (which was needed because of the high temperatures), where Rh traces could be found in the glass afterward.

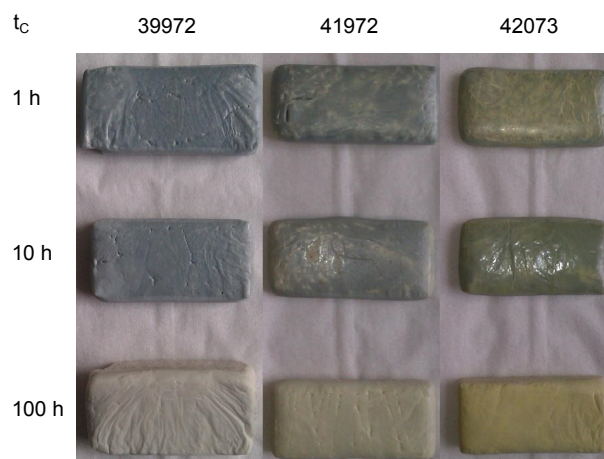It was now investigated, in how far the ceramization time had an influence on the



**Figure 5.26.:** Glass-ceramic samples after different ceramizations at different dwell times $t_c$

conductivity of the samples. The result was an optical brightening with increasing ceramization time as well as that all three versions showed a worse electrical conductivity at prolonged dwell times, which can be seen from figure 5.26 and table 5.6. A heating rate of $8\,\mathrm{K\,min^{-1}}$ was chosen, because this was the maximum rate the now used furnaces could run, also figure 5.23 did not show a distinct dependence on the heating rate as mentioned before. However, it was quite astonishing, that the electrical conductivity of the basic composition 39972 from this experimental run was round about 3 orders of magnitude lower than the values of the previous run. Among the samples from this experimental run, the samples produced in a reducing atmosphere showed a higher electrical conductivity than the ones prepared from 39972, as expected.

Using X-ray diffraction and an internal standard (method described in chapter 4.5), the amount of $SrTiO_3$ in the samples KTE24, KTE25 and KTE26 was determined. The
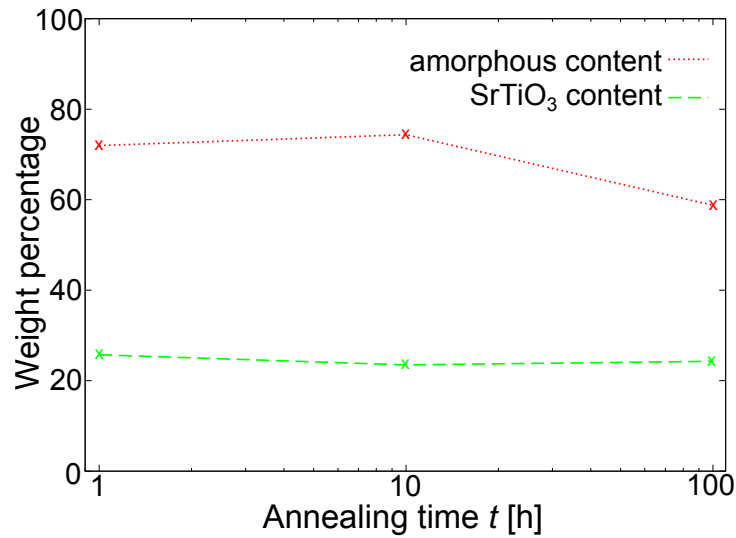
**Figure 5.27.:** Correlation of dwell time and phase content in glass-ceramic samples of glass 39972

result was, that the amount of $SrTiO_3$ was not really influenced by the dwell time and showed values around $24$ - $25\,wt\%$. However, with increasing dwell time, the amorphous content, especially when comparing $t = 10\,h$ to $t = 100\,h$ decreased (see figure 5.27), because additional secondary phases started to grow after $10\,h$. Sample KTE24 (dwell time $1\,h$) and KTE25 (dwell time $10\,h$) contained $SrTiO_3$ (JCPDS 00-035-0734) as a main phase and traces of $TiO_2$ (JCPDS 01-082-0514). KTE26 (dwell time $100\,h$) did contain additional $SrB_2Si_2O_8$ (COD 96-900-4837), $Y_4Nb_4Ti_4O_{24}$ (COD 96-901-1435) and $Sr_8Ti_{10}Si_8O_{44}$ (COD 96-900-5565). The formation of secondary phases is considered to be the main reason behind the deterioration of the electrical conductivity with increasing dwell time.

The formation of these phases can also be seen in the SEM image in figure 5.28. With increasing ceramization time, a small crystal growth of the $SrTiO_3$ can be observed

| Sample | $h$ [$K\,min^{-1}$] | $T_1$ [°C] | $dt$ [h] | $\sigma$ [$S\,cm^{-1}$] |
|---|---|---|---|---|
| KTE-24 | 8 | 895 | 1 | 4.8E-6 |
| KTE-25 | 8 | 895 | 10 | 5.4E-6 |
| KTE-26 | 8 | 895 | 100 | 5.2E-9 |
| KTE-27 | 8 | 895 | 1 | 2.8E-3 |
| KTE-28 | 8 | 895 | 10 | 5.5E-4 |
| KTE-29 | 8 | 895 | 100 | 6.8E-7 |
| KTE-30 | 8 | 895 | 1 | 2.3E-4 |
| KTE-31 | 8 | 895 | 10 | 2.1E-5 |
| KTE-32 | 8 | 895 | 100 | 9.4-10 |

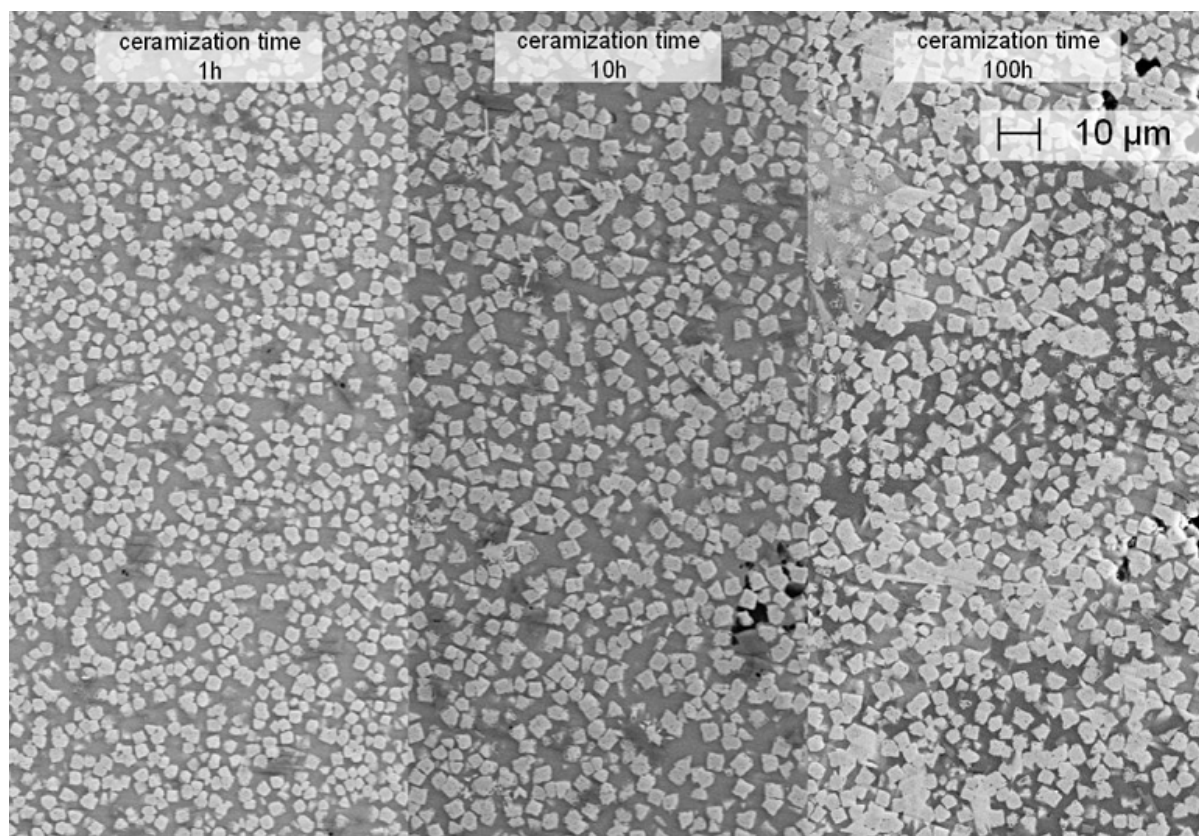**Table 5.6.:** Program of the second ceramization experiment

**Figure 5.28.:** Change in microstructure from KTE24, KTE25 to KTE26

(from $3$ - $4\,\mu m$ to $5$ - $6\,\mu m$, see figure 5.28) but especially after $100\,h$ of dwell time, a lot of inhomogeneous areas containing several secondary phases were formed. It would be expected, that the increased crystal size in KTE25 compared to KTE24 would lead to a higher electrical conductivity but the difference is too small to prove this assumption (see table 5.6). Moreover, the crystals in the SEM images show holes, which is often a sign for too fast crystal growth (see figure 5.29). The insufficient conductivity can be explained by the low phase content of $SrTiO_3$ in the glass-ceramic.

In figure 5.30 of KTE24, connected clusters which are bigger or equal to an area of $A = 500\,\mu m^2$ are colored. One can see, that there are local contacts and connections of the crystals but the amount of crystal phase is not enough to overcome the percolation threshold in the macroscopic picture. Both glasses 41972 and 42073, which have been prepared under reducing atmosphere, show a similar behavior concerning the electrical conductivity, with increasing ceramization time. Like in the previous case, they show a deterioration of the conductivity with time, which is also linked to formation of a secondary phase. Because their electrical conductivity is several orders of magnitude higher than that of KTE24, it is assumed that not only the phase content but also the oxygen partial pressure during melting plays an important role in the
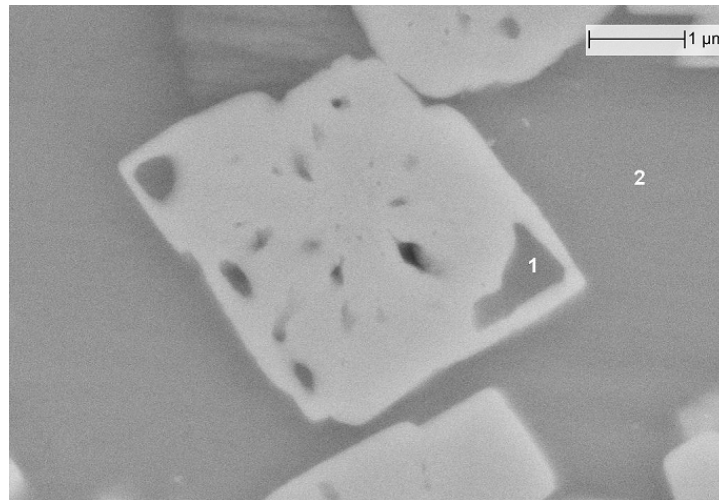
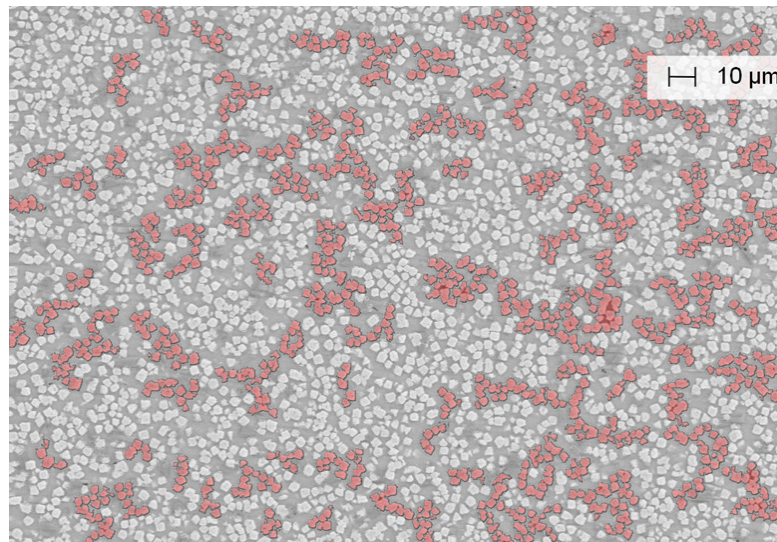**Figure 5.29.:** SrTiO$_3$ crystal in KTE24 with holes (1) and residual glass phase (2)



**Figure 5.30.:** SEM of KTE24 with cluster size $A \geq 500\,\mu\text{m}^2$, determined by ImageJ

determination of their electrical properties.

Via EDX, the chemistry of sample KTE24 was investigated. An overview across a large portion of the sample showed, that there was a small deviation between the content of the synthesis and the sample, which was about $5\,\%$. Only B$_2$O$_3$ showed a major deviation of nearly $20\,\%$. This might be, because the sample did not melt down homogeneously enough so a part of the sample will not be representative for the whole sample. Furthermore, it is not possible to determine the amount of B$_2$O$_3$ directly via EDX due to its weak signal. It could also be seen, that the regions of residual glass phase did not only consist of the network forming SiO$_2$ and B$_2$O$_3$, Sb$_2$O$_3$ and Y$_2$O$_3$ but also parts of SrO, TiO$_2$ and Nb$_2$O$_5$ could be found, which could not
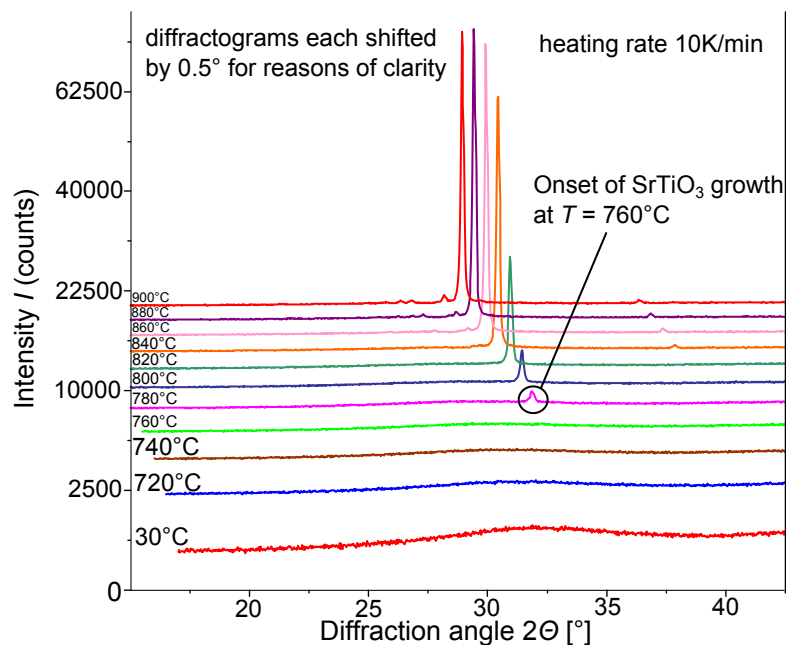
**Figure 5.31.:** High-temperature XRD of glass 39972

be matched to any crystalline phase. This leads to a reevaluation of the calculated theoretical density of the residual glass phase $\rho_G$ which had to be modified according to these findings. It now yields $\rho_G = 2.5\,\mathrm{g\,cm^{-3}}$. Figure 5.31 shows a high-temperature XRD on sample 39972 and reveals, that the crystallization of $SrTiO_3$ takes place at much earlier temperatures than assumed from the DTA. The sample shows the onset of crystallization of $SrTiO_3$ (JCPDS 00-035-0734) at $T = 780\,°C$. At $T = 860\,°C$, the first secondary phase ($TiO_2$, JCPDS 01-082-0514) starts to grow. Therefore, it should be investigated, if a ceramization at lower temperatures near the onset of the peak flank in the DTA can be beneficial for the crystal growth.

**Variation of the ceramization temperature**

In order to check for the influence of the aforementioned effect of earlier crystallization onset, the ceramization temperature was adjusted in a way, that the dwell temperature in the heating programs was set back by $50\,°C$ before the peak obtained from the DTA. By doing this, the early onset of phase formation as seen in the high-temperature XRD should be accounted for and also the crystallization speed should be slowed down in order to avoid the holes in the crystals as they showed up in the SEM image 5.29. The adjusted ceramization programs are shown in table 5.7 Unfortunately, no significant difference in the electrical conductivity could be seen when comparing the properties of the material from the third experimental run to the second one. Only samples from melt number 42073 (KTE41-KTE44) could show a slight increase of about one order of

| Sample | $h$ [K min$^{-1}$] | $T_1$ [°C] | $dt$ [h] | $\sigma$ [S cm$^{-1}$] |
|---|---|---|---|---|
| KTE-33 | 8 | 850 | 1 | 1.8E-6 |
| KTE-34 | 8 | 870 | 1 | 1.7E-6 |
| KTE-35 | 8 | 850 | 10 | 2.4E-6 |
| KTE-36 | 8 | 870 | 10 | 5.5E-6 |
| KTE-37 | 8 | 850 | 1 | 1.8E-3 |
| KTE-38 | 8 | 870 | 1 | 3.6E-3 |
| KTE-39 | 8 | 850 | 10 | 1.1E-3 |
| KTE-40 | 8 | 870 | 10 | 1.3E-3 |
| KTE-41 | 8 | 850 | 1 | 3.4E-5 |
| KTE-42 | 8 | 870 | 1 | 2.4E-4 |
| KTE-43 | 8 | 850 | 10 | 1.3E-4 |
| KTE-44 | 8 | 870 | 10 | 2.8E-5 |

**Table 5.7.:** Program of the third ceramization experiment

magnitude. Since the results did not show a significant influence of the ceramization temperature on the desired properties, no further measurements have been carried out on these samples.

**Influence of a nucleation step**

One last experimental run was carried out in these systems in order to investigate the effect of nucleation before the actual ceramization. For this, the temperature was kept slightly above $T_g$ for about $t = 2$ h before a ceramization temperature at the DTA peak flank was targeted (see table 5.8). This run showed a substantial difference between

| Sample | $h_1$ [K min$^{-1}$] | $T_1$ [°C] | $dt_1$ [h] | $h_2$ [K min$^{-1}$] | $dt_2$ [h] | $\sigma$ [S cm$^{-1}$] |
|---|---|---|---|---|---|---|
| KTE-45 | 8 | 750 | 2 | 850 | 1 | 1.7E-4 |
| KTE-46 | 8 | 750 | 2 | 870 | 1 | 2.8E-3 |
| KTE-47 | 8 | 750 | 2 | 850 | 1 | 1.0E-4 |
| KTE-48 | 8 | 750 | 2 | 870 | 1 | 1.3E-3 |
| KTE-49 | 8 | 750 | 2 | 850 | 1 | 4.1E-7 |
| KTE-50 | 8 | 750 | 2 | 870 | 1 | 3.2E-6 |

**Table 5.8.:** Program of the forth ceramization experiment

the nucleated and the non-nucleated sample for the base composition 39972, the electrical conductivity could be improved to be on the same level as variation 41972 which was melted under reducing atmosphere. The influence of nucleation on samples from this batch however did not show any change in conductivity whether a nucleation took place or not. Concerning sample 42073 it actually showed a degradation of the electrical conductivity when it was subjected to an additional nucleation step. SEM
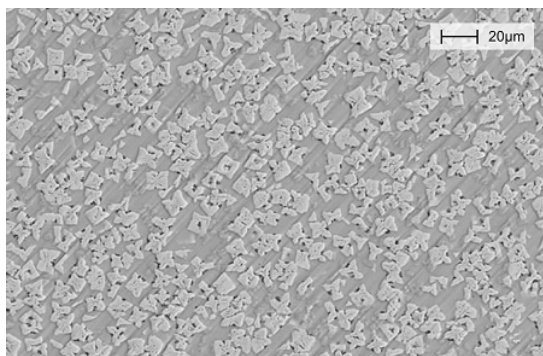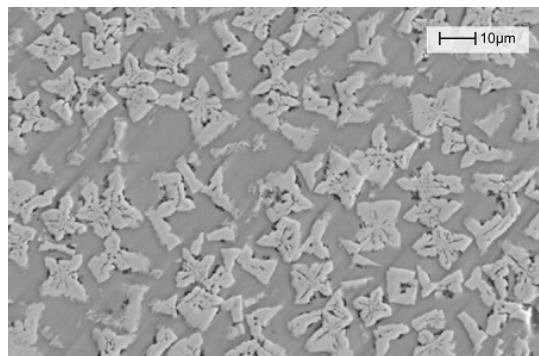
**Figure 5.32.:** SEM image KTE45



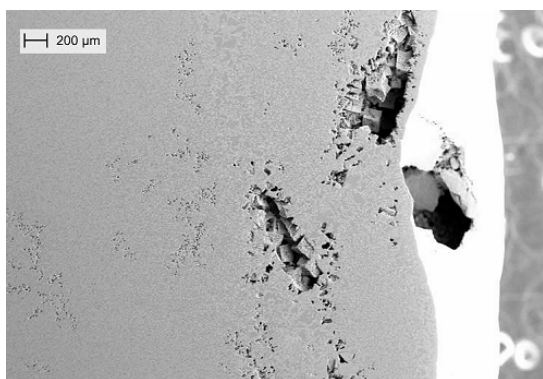**Figure 5.33.:** SEM image KTE46



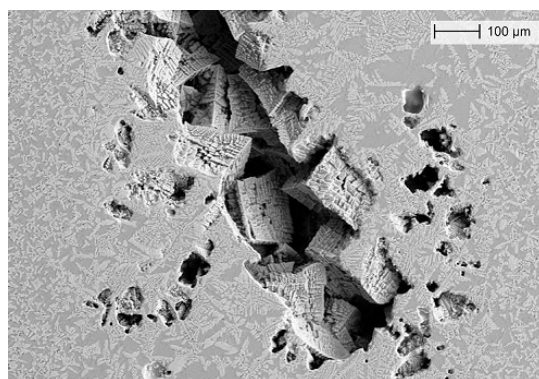**Figure 5.34.:** Zoomed SEM image KTE46



**Figure 5.35.:** Zoomed SEM image KTE46 2

images were taken to get information on the difference in micro structure between the nucleated and non-nucleated case of the samples from 39972. It can be seen, that the samples show a change in microstructure after the nucleation step and their crystal size is enhanced to $\varnothing$ 10-15 $\mu$m (compare the left side of figure 5.28 to figure 5.32 and 5.33). This would support the assumption, that an increased crystal size leads to an enhanced electrical conductivity. Another remarkable feature could be observed, because the $SrTiO_3$ crystals seemed to have formed cubic macro-crystals in the material ($\varnothing$ 150 - 250 $\mu$m, see figure 5.36). This is not completely understood, since it seems that those macro-crystals grew from each of their corners to the center (see the aligned orientation here) so that the overall structure formed a larger cubic crystal. In order to investigate the correlation of the enhanced electrical conductivity in samples KTE45 and KTE46 with their respective amount of $SrTiO_3$, the phase content was determined using a Rietveld refinement with $50 \, wt\%$ of ZnO standard addition. The refinement showed, that the content of $SrTiO_3$ could be increased by a small amount compared to the non-nucleated reference of KTE24.
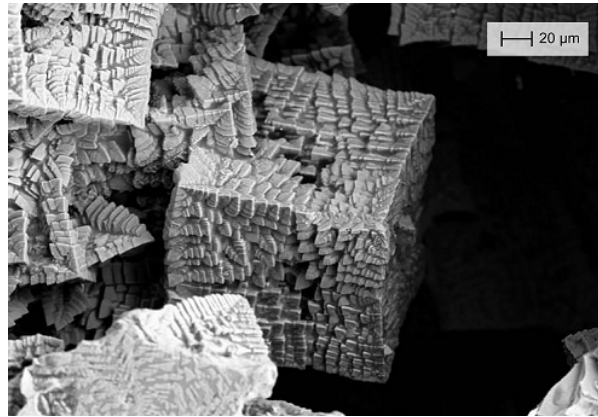
**Figure 5.36.:** Zoomed SEM image KTE46 3

| Sample | wt% SrTiO$_3$ | vol% SrTiO$_3$ |
|--------|---------------|----------------|
| KTE-24 | 27.2 | 15.0 |
| KTE-45 | 28.9 | 16.1 |
| KTE-46 | 30.7 | 17.3 |

**Table 5.9.:** SrTiO$_3$ content in sample KTE24, KTE45 and KTE46

Assuming that the increase in electrical conductivity is really due to the enhanced phase content of SrTiO$_3$, so that this can be described with a percolation mechanism, a fit to the obtained data with the following equations

$$\sigma_l = b(p_c - x)^{-s} \tag{5.29}$$

$$\sigma_h = a(x - p_c)^t \tag{5.30}$$

where $b$, $s$, $a$ und $t$ are fit parameters, was done. For this, the conductivity value of the unceramized glass from figure 5.20, the three values from table 5.9 and a value from literature for the pure phase were used and the fit is shown in figure 5.37. The strong increase of conductivity in the region around $\approx 15\,\mathrm{vol}\%$ may constitute that the system can be characterized by a 3d-percolation threshold which was presented in table 4.1.

In conclusion it can be said, that with the help of compositional variations and different annealing programs it was tried to crystallized Nb-doped SrTiO$_3$ as a single main phase in a glass-ceramic. This could be achieved as XRD data could prove. However, the phase content and the correlated electrical conductivity of the material could not be significantly improved compared to [Lin11]. The phase content $p_m$, which was determined by the XRD using an internal standard could not surpass values of $p_m = 30\,\mathrm{wt}\%$. Since on average, the additional residual glass phase has a lower weight than the crystal phase, this means that the volume fraction of SrTiO$_3$ is even below
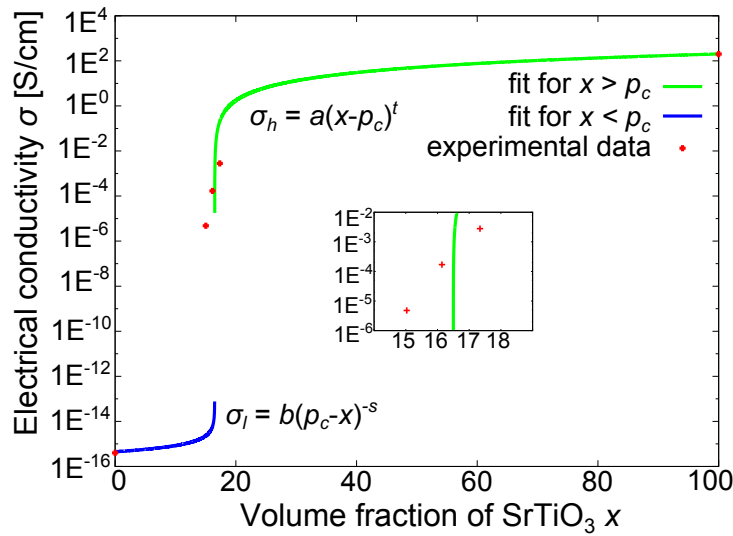
**Figure 5.37.:** Percolation in SrTiO₃ glass-ceramic with fit functions

that, which can be seen in table 5.9. It has to be kept in mind though, that the values were determined by a method that relies on a precise sample homogenization and right choice of a standard, which makes it prone to errors. Using an image analysis software like ImageJ on the SEM images of the glass-ceramic samples, the crystal phase and the residual glass phase can be separated by their different colors and the fractions can be assigned accordingly. KTE24 shows a $SrTiO_3$ surface fraction of $A_A = 45.79\%$, while KTE45 shows $A_A = 40.83\%$ and KTE46 has $A_A = 32.27\%$. Taking the stereological theory into account, which directly relates the surface fraction of a cross section to the volume fraction of the sample ([Del48]), the value of $p_v$ obtained from the SEM images is much higher than the one from the X-ray diffraction refinement.

Among the investigated n-type glass-ceramics, the ones from variation 41972 which had been melted under a reducing atmosphere, showed the highest electrical conductivity. Therefore, those were chosen to be used as an n-type material in the setup of a thermoelectric module which is described in chapter 5.4.

### 5.2.4. $Bi_2Sr_2Co_2O_x$ as a p-type system

Since a thermoelectric module consists of an n-type and a p-type material, a corresponding p-type glass-ceramic material was also investigated and characterized in this work. This was an $Al_2O_3$ based glass containing a crystal phase of $Bi_2Sr_2Co_2O_x$, which was based on a patent of [Fun03] and was further investigated by [Jos12]. The details of the synthesis, the characterization and the material properties can be found
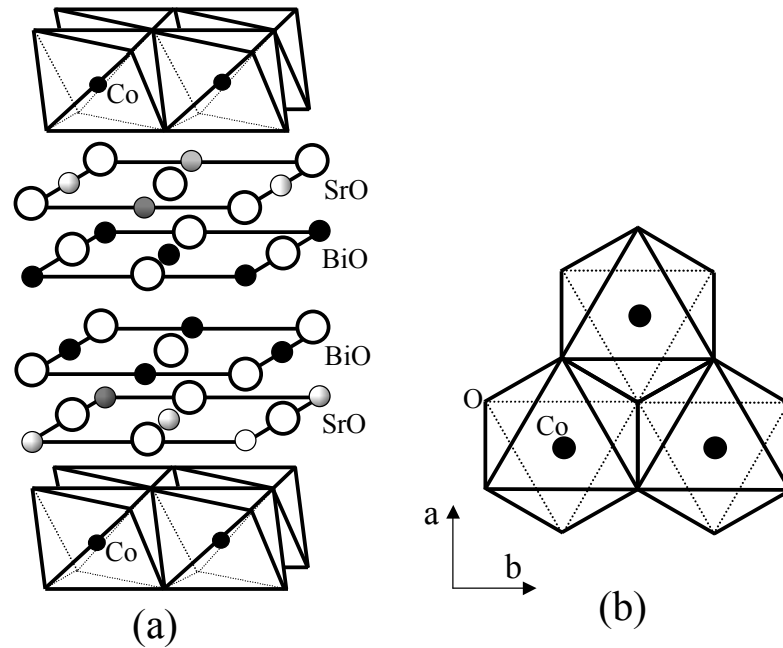
**Figure 5.38.:** $Bi_2Sr_2Co_2O_x$ structure after [YUT02]

in said work. The next pages will give a short summary of the essential insights and gained knowledge for this material. The basic idea behind the diploma thesis of M. Jost [Jos12] was to develop a p-type glass-ceramic material as a counterpart to the already existing n-type glass-ceramic $SrTiO_3$ system. Since the cobaltate materials have been known to offer promising thermoelectric properties (see chapter 2), the first idea was to use a $SiO_2$-$Al_2O_3$-$B_2O_3$ glass-system with a main crystal phase of $Ca_3Co_4O_9$. For that, a ternary phase diagram of $CaO$, $CoO$ und $SiO_2$ was chosen ($SiO_2$ acts as a place holder for all used glass formers in the diagram) and compositions for melting close to the extrapolated eutectic points were chosen. This was done as for the n-type system with the hope of receiving well meltable batches due to the low melting temperature in this region (see figure 5.39). The material melted down easily at temperatures around $T = 1500\,°C$ and had a very low viscosity. However, it crystallized almost instantly upon casting so it was impossible to receive a clear glass which could be treated by a subsequent ceramization step. The electrical conductivity was measured but is was much too low for thermoelectric requirements having values of around $\sigma = 10^{-8}\,S\,cm^{-1}$, so no further measurements were done in this system. Several experiments with modified compositions to obtain a glass and subsequently a single phase glass-ceramic were not successful. By completely removing $B_2O_3$ from the composition, it was possible to receive a glass but due to several different phases in the ternary diagram it was not possible to obtain a single, main thermoelectric phase. X-ray measurements after the ceramization process showed several Co rich
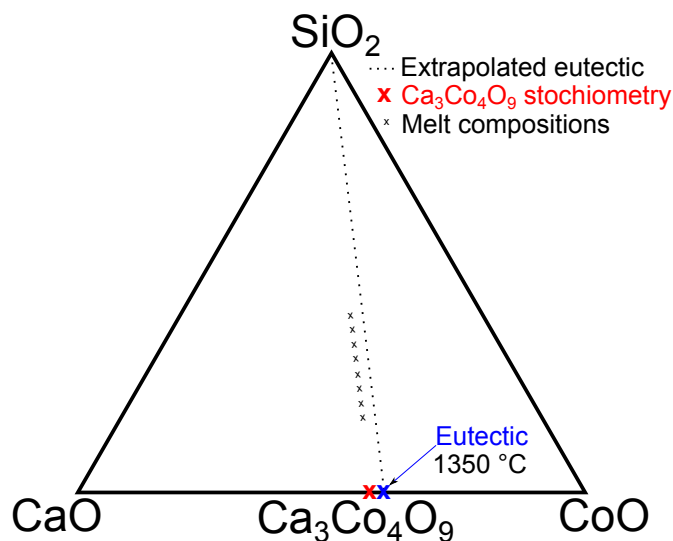
**Figure 5.39.:** Phase diagram $SiO_2$-CaO-CoO system, compositions in mol-% [Jos12]
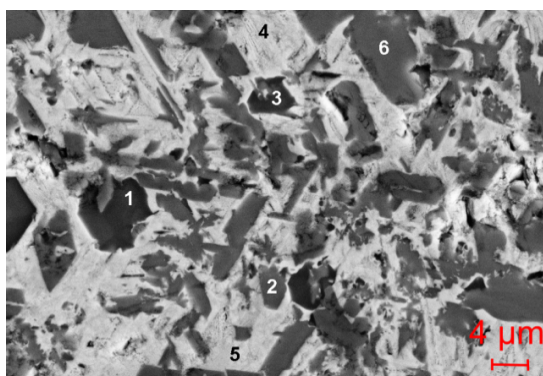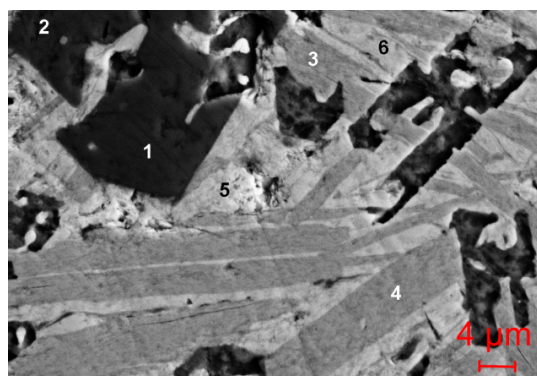


**Figure 5.40.:** SEM image of sample BSCO-1



**Figure 5.41.:** SEM image of sample BSCO-2

phases but the desired $Ca_3Co_4O_9$ could not be obtained. For that reason, the electrical conductivity of the glass-ceramic systems from this experimental run was too small for thermoelectric purposes. Since the patent literature [Fun03] reported on a glass-like system with good thermoelectric properties, where a single crystal could be obtained from extremely slow cooling of a liquid, an experiment was started to adapt this basic idea. It was a Bi-Sr-Co containing melt with a small addition of $Al_2O_3$. Again, the components showed a good melting down behavior and the melt had a low viscosity, but again the melt crystallized upon casting. The X-ray diffraction showed, that the first sample BSCO-1 was very inhomogeneous containing several phases. In an SEM image (figure 5.40) this could be confirmed. Regions 4 and 5 contained $Bi_8Sr_8Co_4O_{25}$ and $Bi_2Sr_2Co_4O_x$, while 1-3 and 6 showed $CaSrBi_2O_5$, CoO und $Ca_3Al_2O_6$. The thermoelectric properties of this material were reasonably good (see table 5.10), even if they did not reproduce the reported values from [Fun03]. Another
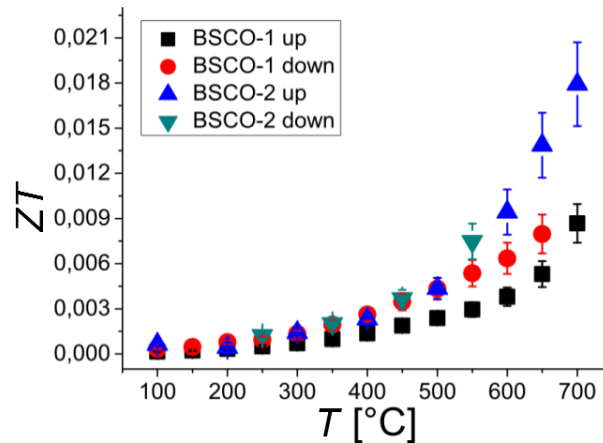
**Figure 5.42.:** $ZT$ values of BSCO-1 and BSCO-2

experiment was started, where $Al_2O_3$ and $CaCO_3$ were removed from the batch. This was done, since a lot of Al and Ca containing secondary phases were determined by XRD and SEM which deteriorate the electrical properties. The resulting material BSCO-2 showed inhomogeneities due to the formation of several phases again. X-ray diffraction measurements and SEM imaging could identify CoO (1 + 2), $Bi_2Sr_2Co_2O_x$ (3 + 4) and $SrBi_4O_7$ (5 + 6) as can be seen in figure 5.41. The materials ZT factor could be improved by a factor of 2 compared to the previous material (see figure 5.42). For the p-type side, a glass-ceramic material was found which showed considerable thermoelectric properties (see table 5.10).

| Sample | $\sigma\,[\mathrm{S\,cm^{-1}}]$ | $S\,[\mathrm{\mu V\,K^{-1}}]$ | $\kappa\,[\mathrm{W\,m^{-1}\,K^{-1}}]$ |
|---|---|---|---|
| BSCO-1 | 16 | 80 | 1.3 |
| BSCO-2 | 4 | 230 | 1.4 |

**Table 5.10.:** Thermoelectric parameters at $T = 700\,^{\circ}\mathrm{C}$

## 5.3. Sinterglass-ceramic

An alternative method to synthesize glass-ceramics is the so called sinter glass-ceramic. Compared to conventional glass-ceramics, the powder composition of the material is sintered in order to form the desired crystal phase. An advantage of that method is the suppression of secondary phases but the disadvantage is the fact, that there is a residual porosity in the samples. This section shows the synthesis and characterization of a $Bi_2Sr_2Co_2O_x$ sinter glass-ceramic (also shown in [LCF$^+$15]) in order to compare it to the existing glass-ceramic specimen BSCO-2. Because the exact growth mechanism of the phase especially from a melt has not been investigated
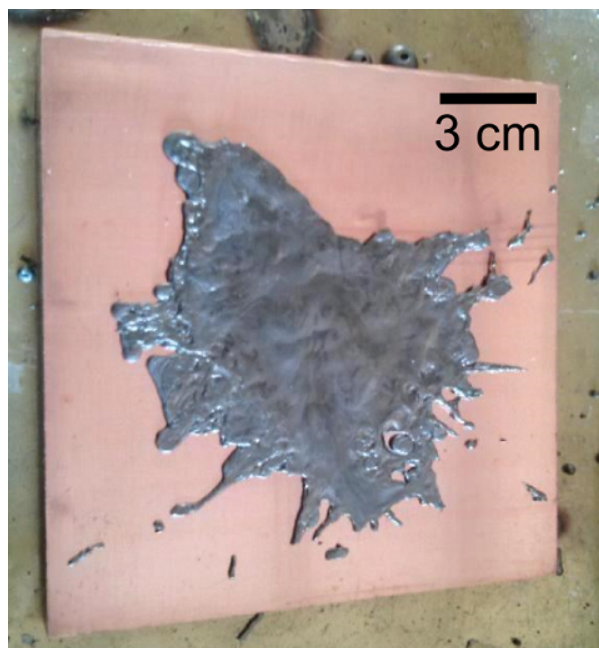
**Figure 5.43.:** Casted and quenched sample BSC222

yet and in order to complete the picture of the already established synthesis routes, this work shows the preparation and characterization of a sintered glass-ceramic material, starting from a complete melt. For this a partly amorphous precursor material undergoes an annealing process during which the desired $Bi_2Sr_2Co_2O_x$ phase is formed and verified.

### 5.3.1. Experimental steps

To obtain a glassy precursor, powders of $SrCO_3$, $Bi_2O_3$ and $Co_3O_4$ were mixed in batches of $50\,g$ with the stoichiometry of $Bi_2Sr_2Co_2O_x$ (BSC222), $Bi_{1.8}Sr_2Co_2O_x$ (Bi1.8) and $Bi_2Sr_2Co_{1.7}O_x$ (Co1.7). They were milled in an automatic agate mill twice for $t = 20\,min$ at 300 rpm. The three stoichiometries were chosen this way to compensate for potential inhomogeneities emerging during or after the subsequent melting process. The powder batch was then put in an aluminum oxide crucible and heated in a high temperature furnace to $T = 1473\,K$. After a dwell time of $t = 30\,min$ the completely liquefied mixture was taken out of the furnace, casted onto a copper plate and immediately quenched from the top with a second copper plate. This way, a partly amorphous precursor material was obtained (see figure 5.43) which was checked by energy-dispersive X-ray spectroscopy (EDX) for its cationic distribution.

Just as expected there was a deviation between the starting compositions and measured cation ratio after the casting (shown in table 5.11). This was due to the fact

that the melt was in contact with the crucible material and therefore an unknown amount of Al was dissolved and changed the overall composition. Sediment inside the crucible could also be observed because when taken out of the furnace, the melt at the bottom solidified too quickly to cast the complete content onto the copper plate. By this, the homogeneity of the precursor material was changed during the melting process as well. In the interest of simplification, the amount of Al content (2-3 mol %) coming from the dissolving alumina crucible was neglected during the EDX scan. It has to be kept in mind though, that a certain amount of Al is inside each sample. It is assumed that this has helped to form the amorphous structure of the material.

It can be seen from table 5.11 that the amount of Co in the casted glassy samples is much higher than in the earlier powder synthesis of said specimen. This is due to the fact that the Co ions tend to stay in the lower viscosity regions of the melt. Therefore they can be found in larger amounts in the casted sample than in the solidified residual at the bottom of the crucible. The reason for that to happen is that Cobalt has the lowest specific weight within the melt, which in return results in the heavier Bismuth being found at the bottom of the crucible while the Cobalt amount is higher at the top. During casting, the Cobalt rich portion comes in contact with the quenching copper plates faster, than the rest of the melt. This effect is enhanced by the absence of convection because stirring inside the crucible was not possible in our case.

Subsequently the quenched glassy samples were crushed and then pulverized in an automatic agate mortar. After that, the powders were pressed on glass substrates and checked for initial crystal phases by X-ray diffraction (XRD) measurements. The rest of the powders was pressed into pellets of $3\,g$ each ($\varnothing = 16\,mm$) using a uniaxial press with a force of $F = 20\,kN$. Then the pressed pellets were put on a gold sheet which was lying on an aluminum shuttle. They were annealed in a muffle furnace under ambient pressure and atmosphere at $T = 1133\,K$ for $15\,h$. A separate calcination step was not considered since all organic remains were assumed to have vanished during the melting process.

After cooling down, the annealed samples were examined via X-ray diffraction (pow-

| Sample name | Bi | Sr | Co |
|---|---|---|---|
| Sample 1 BSC222 | 2/1.8 | 2/1.7 | 2/2.5 |
| Sample 2 Bi1.8 | 1.8/1.7 | 2/1.9 | 2/2.4 |
| Sample 3 Co1.7 | 2/2.1 | 2/1.8 | 1.7/2.1 |

**Table 5.11.:** Cationic content before/after sintering obtained by EDX

der) and scanning electron microscopy (SEM, bulk samples). Because of the lack of applied pressure during the annealing step and therefore during the phase formation in the material, it was not expected that there would be a distinct parallel alignment of the layers but that they would form rather disordered within the sample. Thus it was also not expected that there would be a significant difference of the electrical and thermal properties depending on whether the measurement was done in parallel or perpendicular to the original pressing direction of the pellet. For reasons of simplicity, the electrical measurements were carried out parallel towards the pressing plane.

The samples were cut into rectangular bars and the resistivity $\rho$ was determined using a DC four-probe method. Then the thermovoltage $U$ at a known temperature difference $\Delta T$ was measured and by taking the absolute Seebeck values of the thermocouples into account, the Seebeck coefficient $S$ was calculated. For the contacts on the samples silver paste in combination with Pt and Pt-Rh thermocouples were used. These measurements were done in air atmosphere from room temperature up to $T = 873\,\text{K}$. The thermal diffusivity $\alpha$ and the specific heat $c_p$ were measured with a laser flash apparatus on rectangular thin samples coated with graphite spray for optimized laser absorption. The density of the samples was measured using the Archimedes method to be around $\rho = 6.3\,\text{g}\,\text{cm}^{-3}$ ($\approx 92\,\%$ theoretical density).

In order to correlate the thermoelectric measurement results with the magnetic properties of the material, the temperature dependent susceptibility $\chi$ was measured using a SQUID magnetometer. For that, small sample specimens ($\approx 200\,\text{mg}$) were put in a plastic capsule and the capsule with the sample inside was measured at a field of $H = 1000\,\text{Oe}$ from room temperature down to $T = 2\,\text{K}$. $Co^{3+}$ is expected to be in a low spin (LS) state and to have a completely filled $t_{2g}$ band therefore not contributing to the overall magnetization. $Co^{4+}$ in the LS state has an unfilled band and contributes with S = ½ plus an electronic degeneracy of $g_{Co^{4+}} = 6$ [WRCO03].

A measurement of an empty capsule was done in order to check for the diamagnetic influence of the capsule material on the result. The contribution was well below $10\,\%$ of the result with a sample inside. Because the measurements were primary targeted at showing the relative differences in susceptibility between the samples, the small capsule influence was neglected during measurement and treated as a systematic error. However, a temperature independent parameter $\chi_0$ was obtained from the fit of the Curie-Weiss law to the measurement data later on.
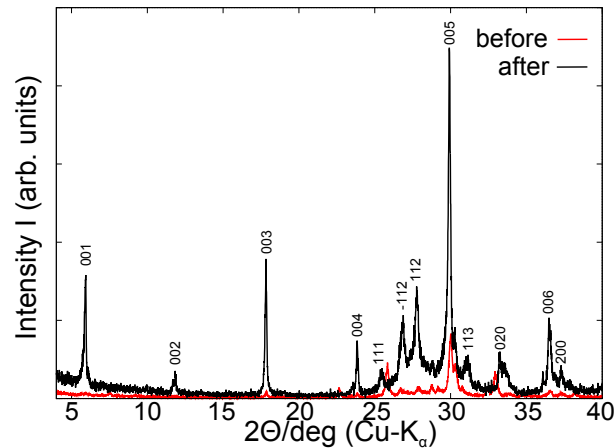
**Figure 5.44.:** XRD of powdered BSC222 before/after annealing
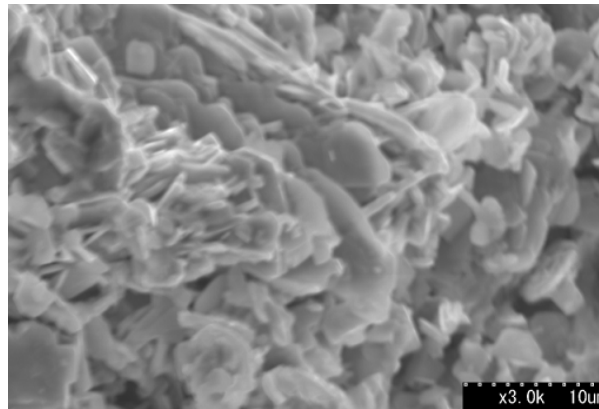


**Figure 5.45.:** SEM image of bulk BSC222 annealing

## 5.3.2. Results

Because the X-ray measurement was done on powdered sample material, there was no specific preferred direction observed in the diffraction image as it could be found in [FMS00]. When comparing the diffraction data of the sample before and after the annealing step, the formation of the $Bi_2Sr_2Co_2O_x$ phase can be clearly observed. Minor unknown crystal phases in the semi-amorphous material vanish during annealing in favor of the desired phase of the sinter glass- ceramic material. This is indicated by the Miller indices of $Bi_2Sr_2Co_2O_x$ in figure 5.44, with peak positions taken from reference [STC$^+$12]. The layered structure of the material which was discussed and shown in reference [FMS00] is less distinctive in the sinter glass-ceramic material as expected. It is noticeable in the SEM picture even though not as aligned and evenly distributed. The grain sizes differ between 2 and $10\,\mu m$. Concerning the measurement results of the electrical resistivity, it is observable that there are some differences between the three samples. The temperature characteristic of sample BSC222 and Co1.7 is quite
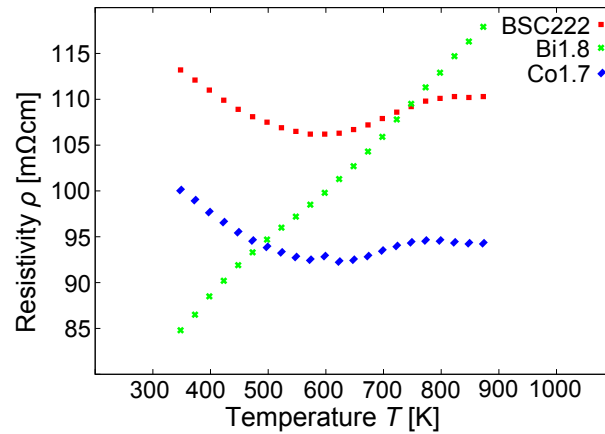
93

**Figure 5.46.:** Temperature dependent resistivity of BSC samples

flat so it is difficult to tell if a semiconducting or a metallic conductivity mechanism is dominating. However both samples show a small decrease of resistivity until $T = 600\,\text{K}$, above that temperature the resistivity increases again. A similar behavior was found in [FMS00] where the increase of resistivity started at $T = 750\,\text{K}$ though. Sample Bi1.8 shows a rather metallic conductivity with the resistivity increasing with increasing temperature across the whole range. This can be explained by a classical Drude type conduction mechanism where the resistivity increases linearly with $T$. An interesting observation is the fact that the Bi1.8 sample shows the overall lowest resistivity $\rho$ of all the samples at room temperature but changes to have the highest resistivity at maximum temperature. In [FMS00], the different slopes of the resistivity measurements were attributed to the different valence states of Co in the samples. Since in this case the cationic composition before and after the melting process differs so much and also the exact oxygen deficiency is unknown, it is impossible to calculate the Co valence to explain the results. If, however, the resistivity and the conduction mechanism are defined by the valence state and the carrier concentration one might assume, that the BSC222 and Co1.7 sample show a similar valence in contrast to Bi1.8. Additionally the hole concentration in Co1.7 should be higher than in BSC222 because of its lower resistivity. It can be observed that the Bi/Sr ratio is $> 1$ at those samples while it is $< 1$ in the Bi1.8 sample. However, no clear possibility is seen how this can explain the metallic conductivity. It might be connected with the oxygen content in the final melt. In figure 5.47 the Seebeck coefficient of the three samples is shown. All measured Seebeck coefficients are positive which indicates a hole-conduction mechanism as expected. With increasing temperature the values of all three samples increase which confirms the resistivity data at least from $T = 600\,\text{K}$ because for metals an increase of the Seebeck coefficient with increasing temperature is expected ($S \propto T$)
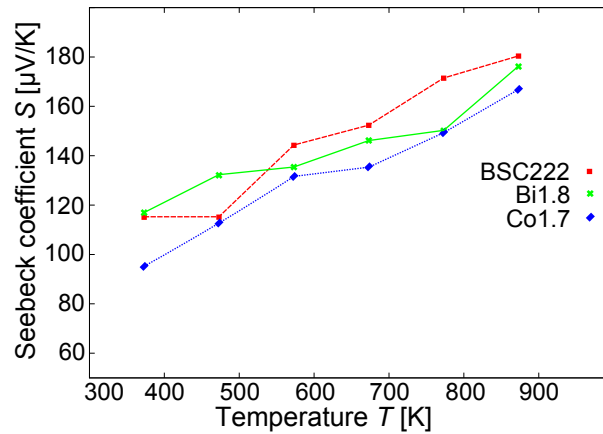
**Figure 5.47.:** Temperature dependent Seebeck coefficient of BSC samples
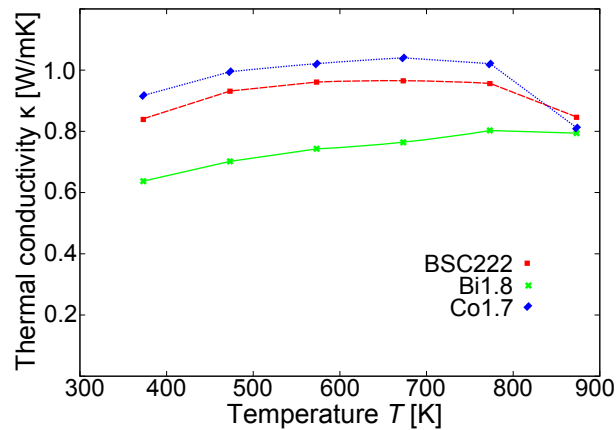


**Figure 5.48.:** Temperature dependent thermal conductivity of BSC samples

[CK58].

Despite the assumed identical Co valence, the Co1.7 sample has a lower $S$ value at $T = 873\,\text{K}$ than the BSC222 sample. As in [FMS00] the difference can be explained by the different carrier concentrations over the spin states of Co. Figure 5.48 shows the thermal conductivity for the three samples. The temperature dependence is almost linear and slightly increasing until $T = 673\,\text{K}$ where a decline of $\kappa$ can be observed. Again, BSC222 and Co1.7 show a very similar behavior and their values differ only slightly. As with the electrical conductivity, Bi1.8 shows a different behavior concerning the thermal conductivity. The thermal conductivity increases incrementally with no change in its slope throughout the measured temperature range. The magnetic measurement of the susceptibility is shown for the samples in figures 5.49 - 5.51. For all samples, the data from $100\,\text{K} < T < 300\,\text{K}$ was fitted using the Curie-Weiss law

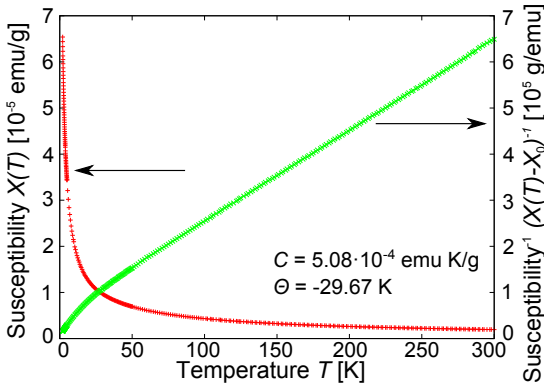$$\chi = \chi_0 + \frac{C}{T - \Theta} \tag{5.31}$$
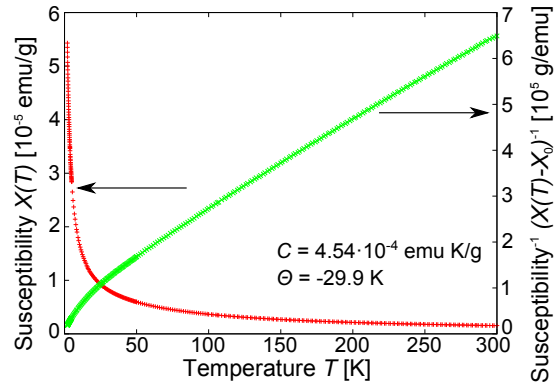
**Figure 5.49.:** Magnetic susceptibility Bi1.8



**Figure 5.50.:** Magnetic susceptibility BSC222
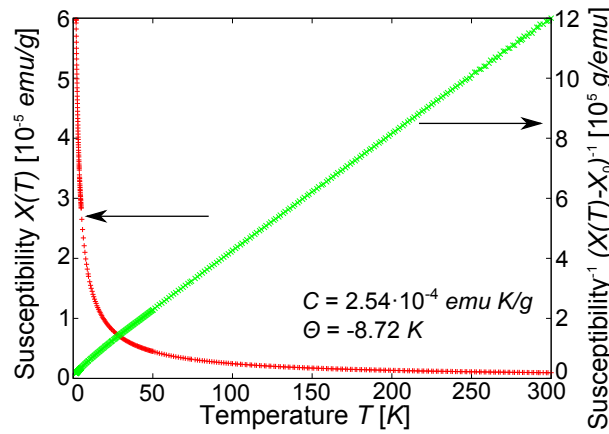


**Figure 5.51.:** Magnetic susceptibility Co1.7

with $\chi_0$, $C$ and $\Theta$ being the temperature independent susceptibility, the Curie constant and the Curie temperature respectively. The linear Curie-Weiss behavior can be observed for $T > 100\,\mathrm{K}$. For all samples, the Curie temperature is negative suggesting an anti-ferromagnetic interaction. Figure 5.52 shows the inverse susceptibility of the samples as well as linear fits to the high temperature data to extrapolate to the Curie temperature. As expected from their compositions, BSC222 and Bi1.8 show a similar susceptibility and Curie temperature.

Only Co1.7 which contains a smaller amount of Co compared to the other samples shows a smaller Curie temperature and a higher inverse susceptibility. The small

| Sample name | $\chi_0$ [emu/g] | $C$ [emuK/g] | $\Theta^1$ [K] | $\Theta^2$ [K] |
|---|---|---|---|---|
| Sample 1 BSC222 | $1.58 \times 10^{-7}$ | $4.54 \times 10^{-4}$ | -29.90 | -30.10 |
| Sample 2 Bi1.8 | $4.13 \times 10^{-7}$ | $5.08 \times 10^{-4}$ | -29.67 | -29.81 |
| Sample 3 Co1.7 | $1.12 \times 10^{-7}$ | $2.54 \times 10^{-4}$ | -8.72 | -10.16 |

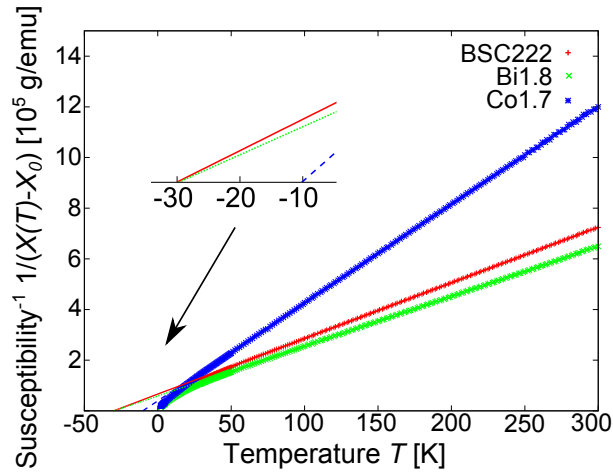**Table 5.12.:** Results Curie-Weiss fit (1) / linear fit (2)

**Figure 5.52.:** Temperature dependent inverse susceptibility

deviation in the data obtained for the Curie Temperature $\Theta$ is due to the different fit accuracies (3-parameter fit of the red data in figures 5.49 - 5.51 using equation 5.31 vs. 2-parameter fit of the inverse susceptibility in figure 5.52).

In order to estimate the amount of $Co^{4+}$ in the samples, the number of Bohr magnetons per formula unit $N_{\mu_B exp}$ was compared to a theoretical value that was obtained by using the Brillouin function. For this, the mole number of each sample was calculated from its weight under the assumption of a constant oxygen content of 9. The number of Bohr magnetons per formula unit was calculated subsequently.

$$N_{fu} = N_{mol} \times N_A \tag{5.32}$$

$$N_{\mu_B exp} = \frac{m}{\mu_B}/N_{fu} \tag{5.33}$$

with $N_{mol}$ being the mole number, $N_A$ the Avogadro number, $m$ the magnetic moment and $\mu_B$ the Bohr magneton.

The theoretical value for the sample containing hypothetically $100\,\%$ $Co^{4+}$ with J = S (pure spin magnetism) was calculated by

$$N_{\mu_B th} = N_{Co} g J f_B \tag{5.34}$$

$$f_B = \left(1 + \frac{1}{2J}\right) \coth\left(\left(1 + \frac{1}{2J}\right)x\right) - \left(\frac{1}{2J}\right) \coth\left(\frac{1}{2J}x\right) \tag{5.35}$$

$$x = \frac{g\mu_B J B}{k_B T} \tag{5.36}$$

Here, $N_{Co}$ stands for the cationic content of Co per formula unit (obtained from EDX measurements, see table 5.11). The Landé factor $g = 2$ and spin S = ½ are used as well as the Brillouin function $f_B$, which takes the orientation of the moments into account. Technically, the Brillouin function is used to describe a paramagnetic substance in an external magnetic field. To account for that, the temperature offset obtained from the Curie-Weiss fits (see figure 5.52) was used. The obtained value for $N_{\mu_B th}$ ($100\,\%$ Co$^{4+}$) was adjusted with a linear scale factor y to match the experimental data of $N_{\mu_B exp}$ in order to find an approximation for the actual amount of Co$^{4+}$ in the investigated sample. This is shown exemplarily in figure 5.53. For the three samples the amount $y$ of Co$^{4+}$ can be seen in table 5.13. From this it is obvious that only a fraction
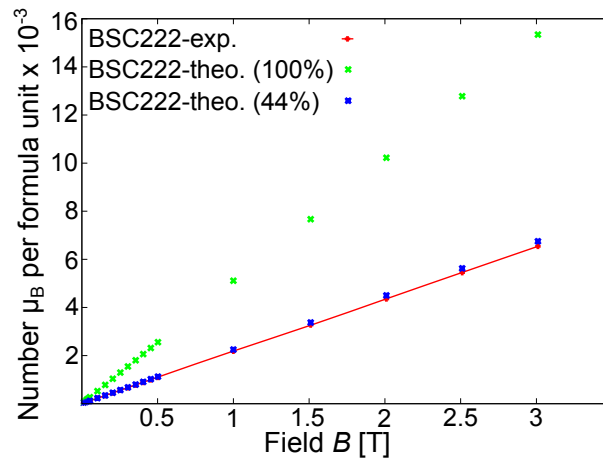


**Figure 5.53.:** Estimation of Co$^{4+}$ content

| Sample name | fraction of Co$^{4+}$ | average Co valence |
|---|---|---|
| BSC222 | 0.44 | 3.44 |
| Bi1.8 | 0.52 | 3.52 |
| Co1.7 | 0.30 | 3.3 |

**Table 5.13.:** Co$^{4+}$ content of the samples

of the Co ions contribute to the overall signal of the magnetization. For Bi1.8, the metallic behavior in electrical conductivity may be explained by the highest average Co valence and therefore the highest hole concentration. The electrical conductivity of the other samples cannot be explained by this because even though the hole concentration in BSC222 is higher than in Co1.7, its resistivity is higher.

Applying the modified Heikes formula [YKMH05]

$$S = -\frac{k_B}{|e|} \ln \left( \frac{1}{g_{Co^{4+}}} \frac{y}{1-y} \right) \tag{5.37}$$

with $g_{Co^{4+}} = 6$, the $Co^{4+}/Co^{3+}$ ratios lead to Seebeck values of $148\,\mu V\,K^{-1}$ (Bi1.8), $175\,\mu V\,K^{-1}$ (BSC222) and $227\,\mu V\,K^{-1}$ (Co1.7). Disregarding the latter, the first two seem to match the experimental findings quite well in the high temperature limit (see figure 5.47). Because the thermoelectric performance is characterized by the dimensionless figure of merit $ZT$, the characterization of the material can be done via $ZT = S^2 T/(\rho\kappa)$. The result is shown in figure 5.54. A $ZT$ value of more than $0.03$ is reached which is about five times lower than in reference [FMS00].
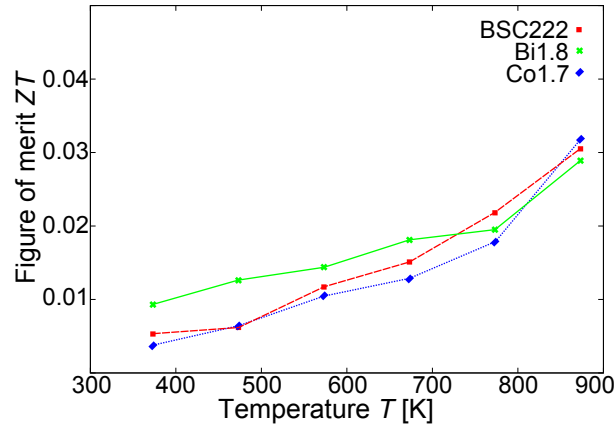


**Figure 5.54.:** $ZT$ data for all samples

## 5.3.3. Conclusions

Sinter glass-ceramic samples with three different cationic compositions have been prepared and measured concerning their thermoelectric and magnetic properties. While comparing the different samples no significant correlation between the thermo-electric properties and the cationic ratio could be calculated. The worse thermoelectric properties compared with pure ceramic $Bi_2Sr_2Co_2O_x$ are mainly due to the lack of homogeneity which comes from the production process of simple casting from an alumina crucible as well as the lack of pressure during the annealing treatment. Techniques like melt spinning and the application of pressure during the phase formation process could be helpful in increasing the homogeneity and density/layer structure which subsequently would improve the thermoelectric properties. In this way, it should be possible to establish a more precise correlation between the compositional details and their impact on the microstructure and properties.

## 5.4. Module fabrication

Since the original idea at the beginning of the thesis was to develop n- and p-type glass-ceramic materials with thermoelectric properties, the ultimate purpose was to integrate them into a thermoelectric module and to measure the resulting output power during operation. Even though the materials' properties were not on par with their corresponding ceramic equivalents, it should be demonstrated, that glass-ceramic materials can withstand the thermal and mechanical requirements within a thermoelectric module. For that, a test module ($16 \times 16$ legs) using both n-type STO and p-type BSCO-2 material was built and tested at the AIST (National Institute of Advanced Industrial Science and Technology, Ikeda, Japan) during a research stay at the Synthetic Nano Function Materials group under the supervision of Dr. Ryoji Funahashi. After the successful assembly but poor performance of the first all glass-ceramic module, a second module (also $16 \times 16$ legs) was built, in which the low efficient n-type $SrTiO_3$ glass-ceramic was replaced by a more efficient, n-type $CaMnO_3$ ceramic, resulting in a mixed-material module made from glass-ceramic and ceramic materials. Measurements on this module being subjected to a temperature gradient of $\Delta T = 600\,\mathrm{K}$ could be carried out and the results of these are presented in the following sections.

### 5.4.1. Thermoelectric properties

Before the materials were integrated into a module, their thermoelectric properties were measured individually. The synthesis of the used sample material has been described in section 5.2.3 and 5.2.4. For the measurement of the electrical properties, the STO and BSCO-2 specimens were glued onto a sample holder and cut into rectangular pieces of $3 \times 3 \times 10\,\mathrm{mm}^3$ with a diamond saw. The obtained sample bars were contacted with thin platinum wires of $0.1\,\mathrm{mm}$ diameter for the temperature-dependent resistivity measurement (four-terminal sensing method). For this, two wires were put on the opposing square ends of the sample and two on top of it and then slightly pressed onto it using silver paste to attach the wires (see figure 5.55). The prepared sample was dried in a furnace overnight at a temperature of $T = 100\,^\circ\mathrm{C}$. For the Seebeck measurement, two thermocouples were prepared for each sample. For this, the ends of a Pt and a Pt/Rh wire were soldered up. These thermocouples were attached to both ends of the sample, so that the contact of both metals was in the middle of the surface on the sample end (see figure 5.56). Again, silver paste was applied to make the wires stick to the sample and everything was dried at the
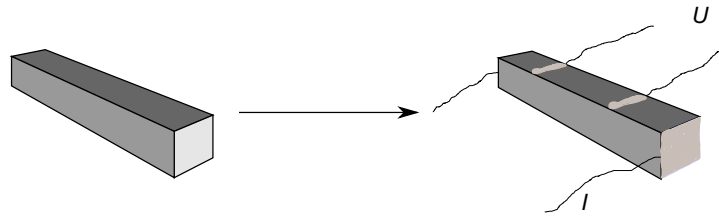
**Figure 5.55.:** Sample contacting electrical resistivity

same conditions as before. For the measurement of the thermal diffusivity $\alpha$ and the
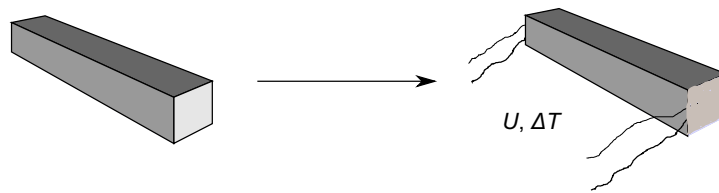


**Figure 5.56.:** Sample contacting Seebeck

specific heat $c_p$, the sample was cut and polished into a thin rectangular geometry of $4 \times 5 \times 0.5\,\mathrm{mm}^3$ and coated with graphite spray twice for optimized laser absorption during the measurement. The density $\rho$, which was needed to calculate the thermal conductivity $\kappa$ from the thermal diffusivity and the specific heat, was determined via the Archimedes method. The electrical measurements have been performed in air while the thermal measurement was carried out in vacuum.

**Properties of n-type STO**

The measured resistivity $\rho$ of STO shows an exponential decrease with rising temperature, which is suggesting a semiconducting character of the material. As with the material from KTE11, a hopping conductivity mechanism is assumed, and an Arrhenius fit of equation 5.27 is applied to the data and shown in figure 5.58. An activation energy $E_A$ of around $0.1\,\mathrm{eV}$ can be obtained. At $T = 625\,^\circ\mathrm{C}$ a value of $\rho = 45\,\Omega\,\mathrm{cm}$ is reached (figure 5.57). The measurement of the Seebeck voltage shows an almost linear correlation between Seebeck coefficient $S$ and temperature $T$. Because of difficulties with the contacts, only the results from $T = 200\,^\circ\mathrm{C}$ and $T = 500\,^\circ\mathrm{C}$ could be used for this plot as these showed steady values over time during the measurement (shown as red data points in figure 5.59). The other data points were taken from the same sample material but from a measurement at a different institute (EMPA, Switzerland). It can be observed, that the data from both measurements seem to be consistent, because they fit into the general trend of the Seebeck coefficient within a similar range. At $T = 600\,^\circ\mathrm{C}$, a maximum value of $S = -474\,\mathrm{\mu V\,K}^{-1}$ can be measured.

The negative sign of the Seebeck coefficient identifies STO to be an n-type, electron conducting material as expected (figure 5.59).

At first, the thermal conductivity $\kappa$ shows hardly any dependence on temperature, only the data point at $T = 600\,°C$ shows a decrease of $\kappa$. Here, the thermal conductivity reaches $\kappa = 1.8\,\mathrm{W\,m^{-1}\,K^{-1}}$. The high resistivity $\rho$ can be understood, since it is known from the XRD and SEM analysis in section 5.2, that the SrTiO$_3$ amount in the glass-ceramic sample is below the percolation threshold. This also explains, why the dimensionless figure of merit $ZT$ calculated from the different properties is below that of all conventional materials, even with acceptable values for Seebeck coefficient $S$ and thermal conductivity $\kappa$. Nevertheless, this subsection on the properties of the n-type glass-ceramic material shows, that the obtained values are consistent with comparable measurements at the EMPA in Dübendorf within the limits of accuracy.

**BSCO-2**

The measured resistivity $\rho$ of BSCO-2 shows a slight increase with rising temperature until $T = 150\,°C$, after that a decrease in $\rho$ can be observed until the end of the measurement, which is suggesting a semiconducting character of the material in this temperature range. At $T = 625\,°C$ a value of $\rho = 0.27\,\Omega\,\mathrm{cm}$ is reached. The measurement of the Seebeck voltage shows a small increase of the Seebeck coefficient with rising temperature. The positive sign of the Seebeck coefficient confirms that BSCO-2 is a p-type, hole conducting material. The thermal conductivity $\kappa$ of BSCO-2 shows a very similar behavior as STO. At first, the temperature dependence is rather insignificant and only at $T = 600\,°C$, a stronger decrease in thermal conductivity can be observed. A minimum value of $\kappa = 1.7\,\mathrm{W\,m^{-1}\,K^{-1}}$ was measured at that temperature. As with
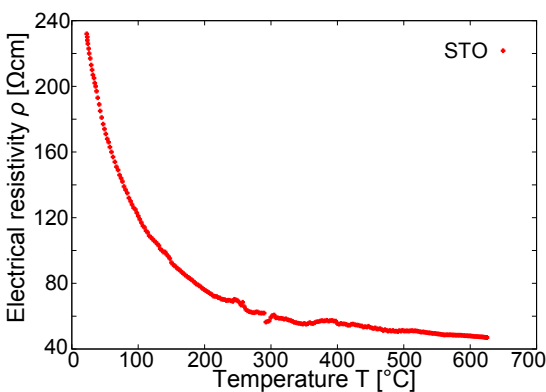


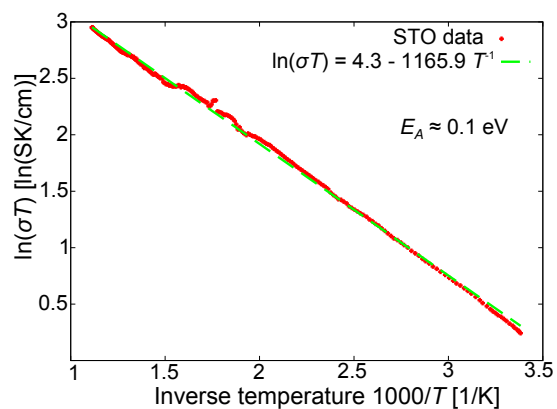**Figure 5.57.:** Electrical resistivity of STO



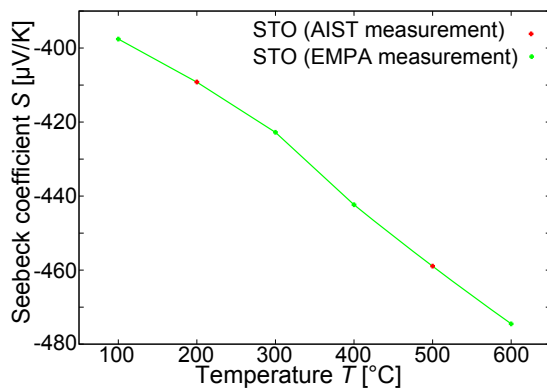**Figure 5.58.:** Calculation of $E_A$ of STO from fit

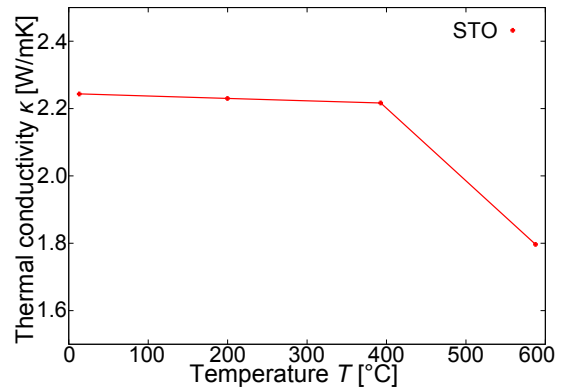**Figure 5.59.:** Seebeck coefficient of STO



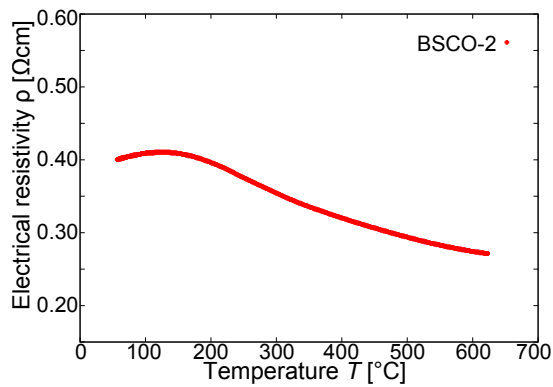**Figure 5.60.:** Thermal conductivity of STO



**Figure 5.61.:** Electrical resistivity of BSCO-2
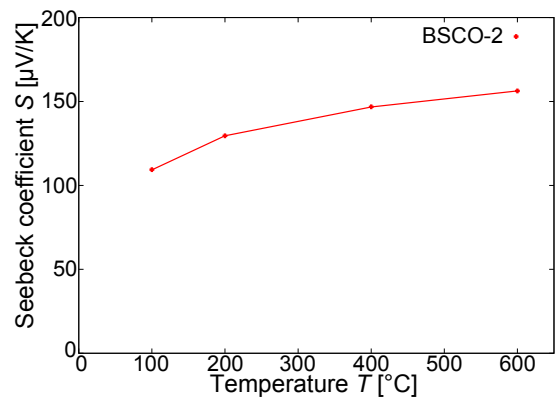


**Figure 5.62.:** Seebeck coefficient of BSCO-2

the STO sample, the BSCO-2 material shows that the electrical conductivity is not high enough in order to compete with ceramic equivalents. The figure of merit $ZT$ is therefore also lower than expected but higher than for the STO sample.

| Quantity at $T = 600\,°C$ | STO | BSCO-2 |
|---|---|---|
| Electrical resistivity $\rho\,[\Omega\,\mathrm{cm}]$ | 45 | 0.27 |
| Seebeck coefficient $S\,[\mu\mathrm{V\,K^{-1}}]$ | -475 | 155 |
| Thermal conductivity $\kappa\,[\mathrm{W\,m^{-1}\,K^{-1}}]$ | 1.8 | 1.7 |
| $ZT$ | $2.4\times10^{-4}$ | $4.6\times10^{-3}$ |

**Table 5.14.:** Thermoelectric properties of n- and p-type glass-ceramics

## 5.4.2. Preparations

Using the material of n-type SrTiO$_3$ glass-ceramic (STO) and p-type Bi$_2$Sr$_2$Co$_2$O$_x$ glass-ceramic (BSCO-2), the samples were cut into equal sized pellets

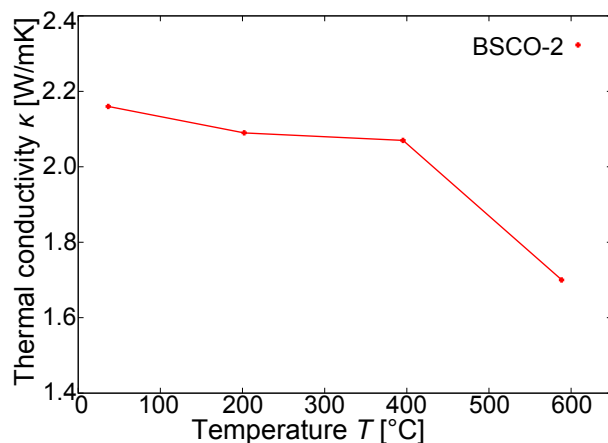**Figure 5.63.:** Thermal conductivity of sample BSCO-2

$(3.5 \times 3.5 \times 5 \, \text{mm}^3)$ with a wire saw. After that, the pellets were placed in an ethanol bath at $T = 80 \, °\text{C}$ (see figure 5.64) and cleaned of all dirt and impurities. In
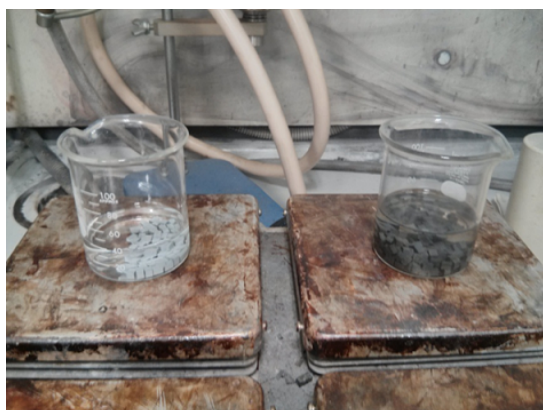


**Figure 5.64.:** Preparation of module pellets
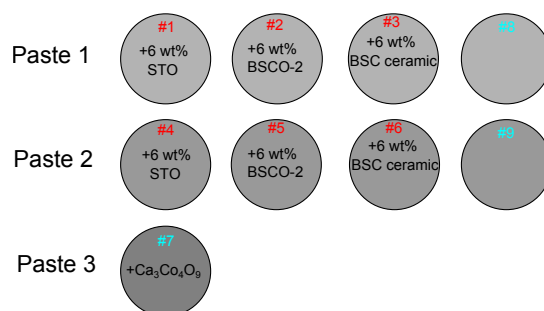


**Figure 5.65.:** Configuration of the silver pastes

the meantime, silver sheets were applied onto an alumina substrate plate as contacts. In order to ensure an optimized contact between sample material (oxide) and silver contacts (metal), it was necessary to establish an appropriate contact between the semiconducting material and the metal. For this reason, two conventional conductive silver pastes were mixed with 6 $\text{wt}\%$ of fine ground ($< 38 \, \mu\text{m}$) oxide powder of STO, BSCO-2 and ceramic $\text{Bi}_2\text{Sr}_2\text{Co}_2\text{O}_x$ respectively. Moreover, a silver paste which already contained additional powder of $\text{Ca}_3\text{Co}_4\text{O}_9$ and the previous pastes without any addition (see figure 5.65) were tested. Using the resulting 7 different silver pastes, small devices ($4 \times 4$, see figure 5.67) were built, contacted and measured to find the minimum of resistance.
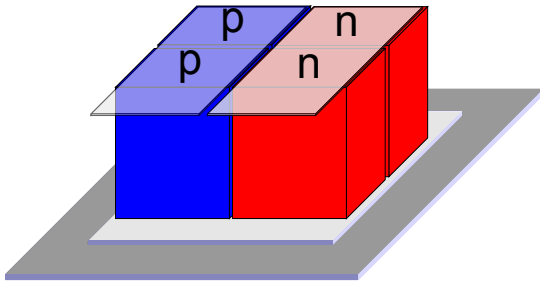
**Figure 5.66.:** Illustration of the device
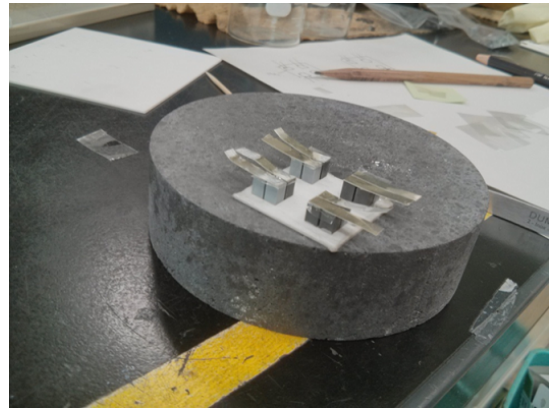


**Figure 5.67.:** Devices before testing

### 5.4.3. Device and Paste testing

For the resistance measurement of the several devices containing the respective silver pastes, different voltages were applied to the devices while measuring the resulting current. Unfortunately, the total resistance of the $SrTiO_3$ glass-ceramic material was too high, so the decision was made to change it to an n-type $CaMnO_3$ ceramic material. With this combination of glass-ceramic and ceramic material, the resistance was measured for all paste configurations. This is shown in figure 5.69. Based on this measurement it was decided that paste number 3, which was mixed with $6\,\mathrm{wt\%}$ of the ceramic $Bi_2Sr_2Co_2O_x$ would be used for the following module setup.
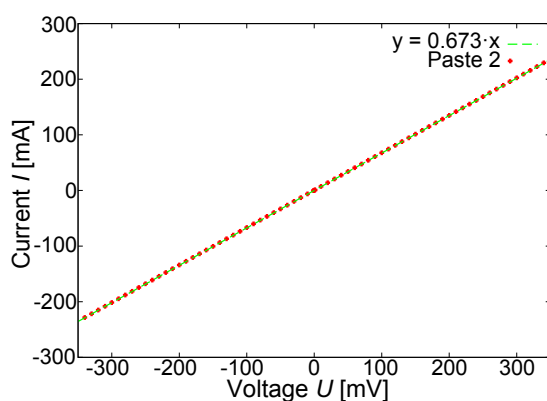


**Figure 5.68.:** Example of current-voltage characteristic of a device



**Figure 5.69.:** Device resistances depending on paste number

## 5.4.4. Setup and properties

The silver paste was applied onto the prepared silver sheets (figure 5.70) on the alumina substrate, using a manual screen printing process. After that, the pellets were attached to the contacts. As with the testing devices, each n- and each p-type pellet was put onto the substrate twice, in order to prevent a disconnection in the series connection of the whole module, in case one leg would break due to thermal or mechanical stress (see figure 5.66). After all pellets had been connected to the contacts,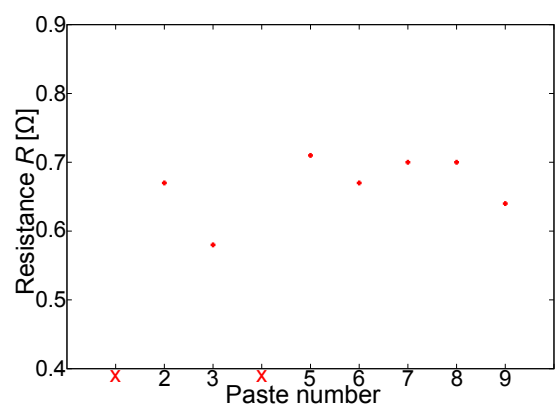 their surface was also contacted with the silver paste. At last, quadratic silver sheets were put on top of 2 n- and 2 p-type pellets each, to complete the contacting. The finished setup was then put in a hot-press machine to reinforce all connections at $T = 650\,°C$. The completed module can be seen in figure 5.71. The
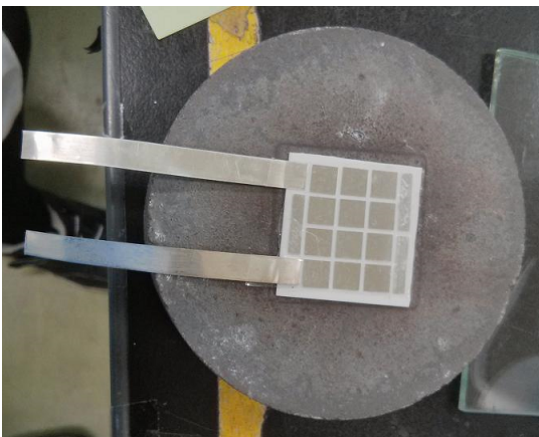


**Figure 5.70.:** Silversheets on the Al$_2$O$_3$ substrate
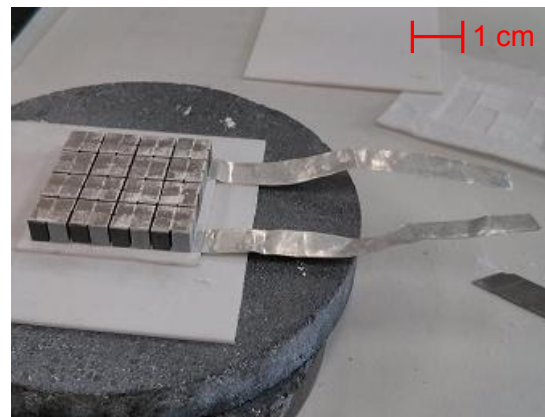


**Figure 5.71.:** Module after hot-pressing

finished module could now be measured. For that, thermocouples were attached to the hot and cold side in order to monitor the temperature and it was mounted onto a testing apparatus. Here it was possible to heat the top while the bottom side was cooled via a water pump system (see figure 5.72). The open circuit voltage of the module $U$ was measured by a high-ohmic voltmeter in the absence of a current. The resistance of the module was determined with the voltmeter-amperemeter method. The module made of STO and BSCO-2 showed an open circuit voltage of $U = 5\,V$ at $T = 700\,°C$ but could not maintain this when a load resistance was applied due to its high internal resistance. Therefore a second module was built using the same process as before but the STO material was replaced by n-type CaMnO$_3$ ceramic. This material is described in more detail in [FMF$^+$06]. With this module, containing ceramic and glass-ceramic elements, the power output seen in figure 5.73 could be obtained. The open circuit voltage reaches a value of $U = 2.3\,V$. If $U$ is calculated
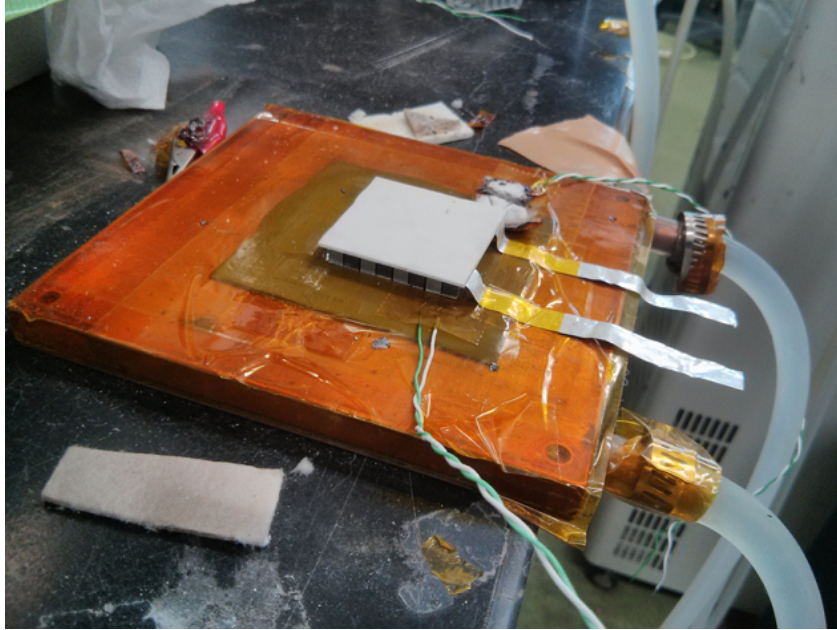
**Figure 5.72.:** Module mounted onto test apparatus
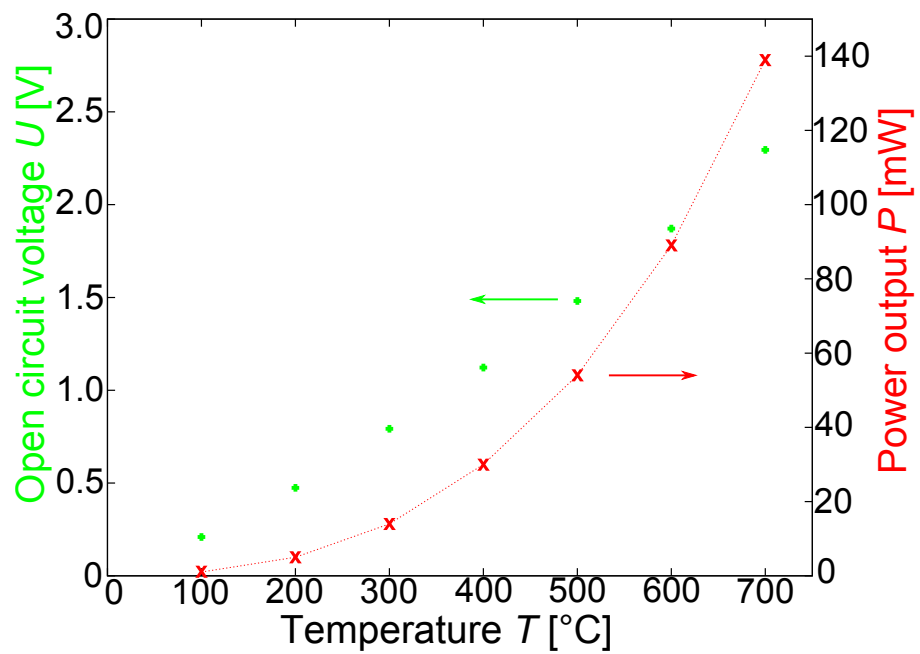


**Figure 5.73.:** Power output of the module

| Temperature $T$ [°C] | 100 | 200 | 300 | 400 | 500 | 600 | 700 |
|---|---|---|---|---|---|---|---|
| $T_h$ [°C] | 93.1 | 186.0 | 281.1 | 377.7 | 477.0 | 571.9 | 668.0 |
| $T_c$ [°C] | 29.0 | 45.6 | 57.6 | 74.9 | 93.0 | 108.9 | 122 |
| Resistance $R$ [Ω] | 10.7 | 10.9 | 10.9 | 10.6 | 10.2 | 9.8 | 9.5 |
| Voltage $U$ [V] | 0.2 | 0.5 | 0.8 | 1.1 | 1.5 | 1.9 | 2.3 |
| Power output $P$ [mW] | 1 | 5 | 14 | 30 | 54 | 89 | 139 |

**Table 5.15.:** Properties of the module

using the average Seebeck coefficients $\widetilde{S_p}$ and $\widetilde{S_n}$ of the corresponding parts of the 4×4 module across the whole temperature range via equation 5.38 it is possible to receive $U = 2.2$ V (using $\widetilde{S_p} = 133\,\mu\text{V K}^{-1}$ (for BSCO-2) and $\widetilde{S_n} = -100\,\mu\text{V K}^{-1}$ (for CaMnO$_3$), as well as $T_h = 700$ °C and $T_c = 100$ °C) which is in good agreement with the measured value.

$$U \approx 16 \times (\widetilde{S_p} - \widetilde{S_n})(T_h - T_c) \tag{5.38}$$

As it can be seen from figure 5.73 the voltage as well as the output power increase during the whole temperature range so that at a hot side temperature of $T_h = 700$ °C an output power of $P = 140$ mW can be measured.

In order to further demonstrate the abilities of the module, a small fan was used as a load resistance during heating. By doing this, it could be shown that thermoelectric modules made from glass-ceramic materials are capable to withstand the thermal and mechanical requirements during operation. The first module showed a large internal resistance so there was no considerable power output which could be measured. After exchanging the n-type glass-ceramic component with a ceramic material, the second module made from both glass-ceramic and ceramic parts yielded power output data which could be analyzed. In order to optimize the modules it would require more efficient material and fatigue tests during several cycles. The coefficient of thermal expansion (CTE) of the different module legs also has to be taken into account when the module is supposed to pass long term durability tests.

# 6. Conclusion

This thesis was focused on the synthesis, the preparation and characterization of glass-ceramic materials concerning their thermoelectric properties. For that, detailed investigations of an n-type glass-ceramic system containing Nb-doped $SrTiO_3$ as a single crystal phase have been carried out. Furthermore, a p-type glass-ceramic system based on $Bi_2Sr_2Co_2O_x$ as the main crystal phase was developed and presented. The synthesis started with a base glass which was subjected to a subsequent heat treatment after casting. The resulting glass-ceramic samples were characterized concerning their thermoelectric properties with the main focus on their electrical conductivity, because this property turned out to be the most difficult to enhance. In the n-type system $SrTiO_3$, the conductivity could be improved by several orders of magnitude and it could be shown, that a reducing atmosphere during the melting process improves the conductivity compared with samples that were produced in air. However, the best values for the electrical conductivity could not surpass $\sigma = 0.1\,\mathrm{S\,cm^{-1}}$ at $T = 650\,°C$. The Seebeck coefficient reached a value of around $S = -450\,\mathrm{\mu V\,K^{-1}}$ at said temperature and a thermal conductivity of about $\kappa = 1.5\,\mathrm{W\,m^{-1}\,K^{-1}}$ could be achieved. For the p-type $Bi_2Sr_2Co_2O_x$ systems, bismuth rich melts have been produced in order to receive a glass-ceramic material based on amorphous $Al_2O_3$ and $Bi_2Sr_2Co_2O_x$ as a single, main crystal phase. Although the samples could not be ceramized in a controlled way, it was possible to obtain $Bi_2Sr_2Co_2O_x$ as a major phase in an inhomogeneous sample material. These specimens showed an electrical conductivity of $\sigma = 10\,\mathrm{S\,cm^{-1}}$, a Seebeck coefficient of $S = 200\,\mathrm{\mu V\,K^{-1}}$ and a thermal conductivity of around $\kappa = 1.5\,\mathrm{W\,m^{-1}\,K^{-1}}$ at $T = 700\,°C$. Even though the obtained properties for both materials were below the ones from their ceramic equivalents, a thermoelectric module from the developed glass-ceramic materials was built. The first module with the n-type leg made of the glass-ceramic $SrTiO_3$ material turned out to be very inefficient since the contact resistance was so high, that no noticeable power output could be measured, once a load resistance was applied to the open circuit. Upon exchanging the n-type $SrTiO_3$ glass-ceramic material for an n-type $CaMnO_3$ ceramic material, a second module could be built using the $Bi_2Sr_2Co_2O_x$ glass-ceramic as a p-type leg. This module could be characterized concerning its power output

and demonstrated, that glass-ceramic materials are able to work in a thermoelectric module under mechanical and thermal load and can generate power by doing so.

## 6.1. Concept assessment and outlook

In order to optimize a multi-component system like an oxide glass-ceramic concerning its electrical conductivity, it has to be ensured that the amount of thermoelectric crystal phase is large enough for the concentration of the crystals to surpass the percolation threshold $p_c$ as described in section 4.2. If this can not be guaranteed, the insulating residual glass phase leads to a resistance of the material, which is too high to provide good thermoelectric properties. Furthermore, the electrical conductivity of the thermoelectric active crystals itself has to be high enough, so that the macroscopic sample yields considerable values. The latter can be achieved by doping and by controlling the atmosphere, under which the samples are prepared, which could be shown in this thesis. However, the properties of the investigated n-type $SrTiO_3$ system seem to be difficult to enhance above the current status by thermal treatment due to the low amounts of forming crystal phase. Methods like melt spinning could allow to decrease the amount of glass-forming oxides in the composition and choosing a sinter glass-ceramic route for this material might enable the crystal fraction to grow beyond the percolation threshold. Likewise, it would be beneficial to create a strong reducing atmosphere during melting, in order to generate oxygen vacancies and therefore additional charge carriers within the material. For this, a special crucible material would have to be found (e.g. boron nitride), which is more durable and less susceptible to alloying with the melt than platinum, which was used as a crucible material during the experiments covered by this thesis. Concerning the p-type $Bi_2Sr_2Co_2O_x$, the main issue with the insufficient efficiency can be blamed on the phase inhomogeneity within the sample. Here, a way to improve the purity of the phase within the amorphous matrix has to be found. This might be done by compositional variations or slower cooling rates as suggested by [Fun03].

In summary it can be said, that thermoelectric glass-ceramics offer an interesting approach to solve the challenge of enhancing the efficiency of thermoelectric materials. Even though an actual increase of said efficiency could not be demonstrated by the investigated glass-ceramics, the potential for this material class still holds, if the aforementioned challenges can be addressed. This thesis, which concluded with the fabrication of the first glass-ceramic containing thermoelectric module, can be taken as the starting point for future developments in this field.

# A. Appendix

## A.1. Attended conferences (selected)

- 9th European Conference on Thermoelectrics (ECT), Thessaloniki, Greece, September 28th - 30th, 2011

  **Poster**: *Nb doped SrTiO$_3$ glass-ceramics as high-temperature stable n-type oxide thermoelectrics*

- 76th annual meeting of the Deutsche Physikalische Gesellschaft (DPG), Frühjahrstagung der Sektion Kondensierte Materie (SKM), Berlin, Germany, March 25th - 30th, 2012

  **Talk**: *Glass-ceramics as high temperature oxide thermoelectrics*

- 29th European Materials Research Society (E-MRS) Spring Meeting, Strasbourg, France, May 14th - 18th, 2012

  **Talk**: *Glass-ceramics as high temperature thermoelectric materials*

- 77th annual meeting of the Deutsche Physikalische Gesellschaft (DPG), Frühjahrstagung der Sektion Kondensierte Materie (SKM), Regensburg, Germany, March 10th - 15th, 2013

  **Talk**: *Glass-ceramics as a new material class for high temperature oxide thermoelectrics*

- 32th International Conference on Thermoelectrics (ICT), Kobe, Japan, June 30th - July 04th, 2013

  **Poster**: *Glass-ceramics as high temperature oxide thermoelectric materials*

- Joint Seminar on Thermoelectrics (AIST Ikeda and Osaka Prefecture University), Ikeda, Japan, December 19th, 2013

  **Talk**: *Thermoelectric oxides in glass-ceramic materials*

- 78$^{th}$ annual meeting of the Deutsche Physikalische Gesellschaft (DPG), Frühjahrstagung der Sektion Kondensierte Materie (SKM), Dresden, Germany, March 30$^{th}$ - April 04$^{th}$, 2014

  **Poster**: *Thermoelectric oxides in glass-ceramic structures*

- 1$^{st}$ Joint Meeting of the Deutsche Glastechnische Gesellschaft (DGG) / American Ceramic Society (ACerS), Glasses and Optical Materials Devision (GOMD), Aachen, Germany, May 25$^{th}$ - 29$^{th}$, 2014

  **Poster**: *Thermoelectric phases in glass-ceramic materials*
  (Hüttentechnische Vereinigung der Deutschen Glasindustrie (HVG) - DGG Best Poster Award, 2$^{nd}$ place)

- DGG-Glasforum, Mainz, Germany, September 18$^{th}$, 2014

  **Talk**: *Thermoelectric glass-ceramics - from concept to power generating modules*

## A.2. Publications

- J. Lingner, M. Letz, G. Jakob - Nb-doped $SrTiO_3$ glass-ceramics as high temperature stable n-type oxide thermoelectrics, *American Institute of Physics (AIP) Conference Proceedings* 1449, pp. 343-346, 2012

- J. Lingner, M. Letz, G. Jakob - $SrTiO_3$ glass-ceramics as oxide thermoelectrics, *Journal of Materials Science* 48 (7), pp. 2812-2816, 2013

- J. Lingner, E. Combe, R. Funahashi, M. Letz, G. Jakob - Thermoelectric sintered glass-ceramics with a $Bi_2Sr_2Co_2O_x$ phase, *Applied Physics A*, 2015 (accepted)

- J. Lingner, M. Jost, E. Combe, R. Funahashi, M. Letz, G. Jakob - Thermoelectric glass-ceramics from a melt process, 2015 (in preparation)

- M. Jost, J. Lingner, M. Letz, G. Jakob - Thermoelectric properties of p-type $Bi_2Sr_2Co_2O_9$ glass-ceramics, *Semiconductor Science & Technology* 29 (12), 124011, 2014

## A.3. Work experience

- Research Intern at Synthetic Nano-Function Materials Group, AIST Ikeda, Japan 15$^{th}$ November 2013 - 15$^{th}$ February 2014

Die vorliegende Arbeit wurde in der Zeit von Oktober 2011 bis Dezember 2014 am Institut für Physik im Fachbereich 08 - Physik, Mathematik und Informatik der Johannes Gutenberg-Universität, Mainz in Zusammenarbeit mit der SCHOTT AG in Mainz angefertigt.

Hiermit versichere ich, dass ich die vorliegende Dissertation selbstständig verfasst und keine anderen als die angegebenen Hilfsmittel benutzt habe. Alle der Literatur entnommenen Stellen sind als solche gekennzeichnet.

Die Arbeit wurde bisher weder im In- noch im Ausland in gleicher oder ähnlicher Form einer anderen Prüfungsbehörde vorgelegt. Ich habe bisher keinen Promotionsversuch unternommen.

Mainz, Januar 2015

# Bibliography

[And58]    P. W. Anderson.   Absence of Diffusion in Certain Random Lattices. *Physical Review*, 109(5):1492–1505, March 1958.

[Ber03]    R. A. Berner.  The long-term carbon cycle, fossil fuels and atmospheric composition. *Nature*, 426(6964):323–326, November 2003.

[BH12]     A. Bunde and S. Havlin. Percolation I. In A. Bunde and S. Havlin, editors, *Fractals and Disordered Systems*, pages 51–114. Springer Berlin Heidelberg, 2012.

[BHH⁺08]   P. Blennow, A. Hagen, K. K. Hansen, L. R. Wallenberg, and M. Mogensen. Defect and electrical transport properties of Nb-doped $SrTiO_3$. *Solid State Ionics*, 179(35–36):2047–2058, June 2008.

[BK05]     A. Bunde and J. W. Kantelhardt. Diffusion and Conduction in Percolation Systems.  In P. Heitjans and J. Kärger, editors, *Diffusion in Condensed Matter - Methods, Materials, Models*, pages 895–914. Springer Berlin Heidelberg, 2005.

[BKSG13]   G. Bakan, N. Khan, H. Silva, and A. Gokirmak.   High-temperature thermoelectric transport at small scales: Thermal generation, transport and recombination of minority carriers.  *Scientific Reports*, 3(2742):1–5, September 2013.

[Bou08]    E. L. Bourhis. *Glass: Mechanics and Technology*. Wiley-VCH, 2008.

[Bre99]    K. F. Brennan. *The Physics of Semiconductors: With Applications to Optoelectronic Devices*. Cambridge University Press, 1999.

[Bro02]    M. E. Brown. *Introduction to Thermal Analysis: Techniques and Applications*, volume 1 of *Hot Topics in Thermal Analysis and Calorimetry*. Springer, 2nd edition, 2002.

[BRRM+14] M. Backhaus-Ricoult, J. Rustad, L. Moore, C. Smith, and J. Brown. Semi-conducting large bandgap oxides as potential thermoelectric materials for high-temperature power generation? *Applied Physics A - Materials Science and Processing*, 116(2):433–470, June 2014.

[Bru97] P. G. Bruce. *Solid State Electrochemistry*, volume 5 of *Chemistry of Solid State Materials*. Cambridge University Press, 1997.

[BSB99] S. Bogdanovich, M. P. Sarachik, and R. N. Bhatt. Scaling of the Conductivity with Temperature and Uniaxial Stress in Si:B at the Metal-Insulator Transition. *Physical Review Letters*, 82(1):137–140, January 1999.

[CB76] P. M. Chaikin and G. Beni. Thermopower in the correlated hopping regime. *Physical Review B*, 13(2):647–651, January 1976.

[Chu10] D.D.L. Chung. *Composite Materials: Science and Applications*. Engineering Materials and Processes. Springer, 2010.

[CK58] N. Cusack and P. Kendall. The Absolute Scale of Thermoelectric Power at High Temperature. *Proceedings of the Physical Society*, 72(5):898, November 1958.

[CvB60] J. Callaway and H. C. v. Baeyer. Effect of point imperfections on lattice thermal conductivity. *Physical Review*, 120(4):1149–1154, November 1960.

[Del48] A. Delesse. Procede Mechanique pour Determiner la Composition des Roches. *Annales des Mines*, 13(4):379–388, 1848.

[Dom13] L. E. Doman. International Energy Outlook 2013. *IEO2013 Report*, July 2013.

[Drö13] B. Dröschel. Abwärmenutzung in Deutschland. In *Abwärmenutzung: Energie für die Zukunft*. Institut für ZukunftsEnergieSysteme, 2013.

[Eag94] M. Eagleson. *Concise Encyclopedia Chemistry*. Walter de Gruyter, 1994.

[EnB14] EnBW. Kernkraft-Standorte der EnBW. `https://www.enbw.com/unternehmen/konzern/energieerzeugung/kernenergie/standorte.html`, December 2014.

[FAC] FACTSAGE. Binary phase diagram $BO_{1.5}$-$SiO_2$. http://www.crct.polymtl.ca/fact/Documentation/All_Figs.htm, visited October 1st 2014.

[Fec95]     H. J. Fecht.   Thermodynamic Properties of Amorphous Solids - Glass Formation and Glass Transition. *Materials Transactions JIM*, 36(7):777–793, February 1995.

[FMF$^+$06]     D. Flahaut, T. Mihara, R. Funahashi, N. Nabeshima, K. Lee, H. Ohta, and K. Koumoto.   Thermoelectrical properties of A-site substituted $Ca_{1-x}Re_xMnO_3$ system. *Journal of Applied Physics*, 100(8), October 2006.

[FMN01]     K. Fujita, T. Mochida, and K. Nakamura. High-Temperature Thermoelectric Properties of $Na_xCoO_{2-\delta}$ Single Crystals. *Japanese Journal of Applied Physics*, 40(7R):4644, 2001.

[FMS00]     R. Funahashi, I. Matsubara, and S. Sodeoka.   Thermoelectric properties of $Bi_2Sr_2Co_2O_x$ polycrystalline materials.   *Applied Physics Letters*, 76(17):2385–2387, 2000.

[Fox12]     M. Fox.   *Optische Eigenschaften von Festkörpern*.   Oldenbourg Wissenschaftsverlag, 2012.

[Fra10]     M. Franz. Topological insulators: Starting a new family. *Nature Materials*, 9(7):536–537, May 2010.

[Fu00]     Y. Fu.   Grain-boundary effects on the electrical resistivity and the ferromagnetic transition temperature of $La_{0.8}Ca_{0.2}MnO_3$.   *Applied Physics Letters*, 77(1):118–120, May 2000.

[Fun03]     R. Funahashi.   Complex oxide having high thermoelectric conversion efficiency, 2003.  US Patent 20030168641 A1.

[GE84]     N.N. Greenwood and A. Earnshaw. *Chemistry of the elements*. Pergamon Press, 1984.

[Gon]     R. J. Gonsalves.   Java Applet:   Percolation. http://www.physics.buffalo.edu/gonsalves/Java/Percolation.html, visited December 1$^{st}$ 2014.

[Göt08]     W. Götze. *Complex Dynamics of Glass-Forming Liquids : A Mode-Coupling Theory: A Mode-Coupling Theory*. International Series of Monographs on Physics. OUP Oxford, 2008.

[GSZ$^+$11]     C. Goupil, W. Seifert, K. Zabrocki, E. Müller, and G. J. Snyder.   Thermodynamics of Thermoelectric Phenomena and Applications. *Entropy*, 13(8):1481–1517, August 2011.

[GW64]     B. M. Gatehouse and A. D. Wadsley. The crystal structure of the high temperature form of niobium pentoxide. *Acta Crystallographica*, 17(12):1545–1554, December 1964.

[Hai95]    P.J. Haines. *Thermal methods of analysis: principles, applications and problems*. Blackie Academic & Professional, 1995.

[HD93a]    L. D. Hicks and M. S. Dresselhaus. Effect of quantum-well structures on the thermoelectric figure of merit. *Physical Review B*, 47(19):12727–12731, May 1993.

[HD93b]    L. D. Hicks and M. S. Dresselhaus. Thermoelectric figure of merit of a one-dimensional conductor. *Physical Review B*, 47(24):16631–16634, June 1993.

[HJL$^+$81]  J. Hansen, D. Johnson, A. Lacis, S. Lebedeff, P. Lee, D. Rind, and G. Russell. Climate Impact of Increasing Atmospheric Carbon Dioxide. *Science*, 213(4511):957–966, August 1981.

[Hol63]    M. G. Holland. Analysis of Lattice Thermal Conductivity. *Physical Review*, 132(6):2461–2471, December 1963.

[Hov11]    M. Hovhannisyan. Phase diagram of $SrTiO_3$-$B_2O_3$, 2011. Private communication.

[HWW07]    A.F. Holleman, E. Wiberg, and N. Wiberg. *Lehrbuch der Anorganischen Chemie*. Walter de Gruyter, 2007.

[HZHJ05]   R. Hansson, B. Zhao, P.C. Hayes, and E. Jak. A reinvestigation of phase equilibria in the system $Al_2O_3$-$SiO_2$-ZnO. *Metallurgical and Materials Transactions B*, 36(2):187–193, 2005.

[IL09]     H. Ibach and H. Lüth. *Festkorperphysik Einführung In Die Grundlagen*. Springer-Lehrbuch. Springer, 2009.

[IR60]     A. Ioffe and A. Regel. *Non crystalline, amorphous and liquid electronic semiconductors*, volume 4 of *Progress in Semiconductors*. Wiley New York, 1960.

[Jon77]    A. K. Jonscher. The 'universal' dielectric response. *Nature*, 267(5613):673–679, June 1977.

[Jos12]    M. Jost.    $Ca_3Co_4O_9$ Keramiken und Glaskeramiken als oxidische Thermoelektrika, 2012. Diplomarbeit, Johannes Gutenberg-Universität Mainz.

[Kis56]    H. E. Kissinger. Variation of Peak Temperature with Heating Rate in Differential Thermal Analysis. *Journal of Research of the National Bureau of Standards*, 57(4):217–221, June 1956.

[Kit49]    C. Kittel. Interpretation of the Thermal Conductivity of Glasses. *Physical Review*, 75(6):972–974, March 1949.

[Kit99]    C. Kittel. *Einführung in die Festkörperphysik*. Springer Science and Business Media, 1999.

[Kle06]    R. Kleiner. Experimentalphysik V - Festkörperphysik. Lecture University Tübingen, 2006.

[KLH$^+$07]    V. V. Krishnamurthy, J. C. Lang, D. Haskel, D. J. Keavney, G. Srajer, J. L. Robertson, B. C. Sales, D. G. Mandrus, D. J. Singh, and D. I. Bilc. Ferrimagnetism in $EuFe_4Sb_{12}$ due to the Interplay of $f$-Electron Moments and a Nearly Ferromagnetic Host. *Physical Review Letters*, 98(12):126403, March 2007.

[KM01]    W. Koshibae and S. Maekawa. Effects of Spin and Orbital Degeneracy on the Thermopower of Strongly Correlated Systems. *Physical Review Letters*, 87(23):236603, November 2001.

[KTM00]    W. Koshibae, K. Tsutsui, and S. Maekawa. Thermopower in cobalt oxides. *Physical Review B*, 62(11):6869–6872, September 2000.

[Kub57]    R. Kubo. Statistical-Mechanical Theory of Irreversible Processes. I. General Theory and Simple Applications to Magnetic and Conduction Problems. *Journal of the Physical Society of Japan*, 12(6):570–586, June 1957.

[KV56]    F. A. Kröger and H. J. Vink. Relations between the Concentrations of Imperfections in Crystalline Solids. In F. Seitz and D. Turnbull, editors, *Solid State Physics*, volume 3 of *Solid State Physics*, pages 307–435. Academic Press, 1956.

[KWZ$^+$10]    K. Koumoto, Y. Wang, R. Zhang, A. Kosuga, and R. Funahashi. Oxide thermoelectric materials: A nanostructuring approach. *Annu. Rev. Mater. Res*, 40:363–394, 2010.

[LCF+15]    J. Lingner, E. Combe, R. Funahashi, M. Letz, and G. Jakob. Thermoelectric sintered glass-ceramics with a $Bi_2Sr_2Co_2O_x$ phase. *Applied Physics A*, -(-):–, - 2015. submitted.

[Lew05]    N. S. Lewis. Basic Research Needs for Solar Energy Utilization. *Report on the Basic Energy Sciences Workshop on Solar Energy Utilization*, April 2005.

[Lid10]    D. R. Lide. *CRC Handbook of Chemistry and Physics*. CRC Press/Taylor and Francis, 2010.

[Lin11]    J. Lingner. $SrTiO_3$ glass-ceramics as oxide thermoelectrics, 2011. Diplomarbeit, Johannes Gutenberg-Universität Mainz.

[LTZU09]    H. Li, X. Tang, Q. Zhang, and C. Uher. High performance $In_xCe_yCo_4Sb_{12}$ thermoelectric materials with in situ forming nanostructured InSb phase. *Applied Physics Letters*, 94(10):102114, 2009.

[LW91]    H. v. Löhneysen and M. Welsch. Quantitative evaluation of electron-electron-interaction effects in the magnetoconductivity of heavily doped metallic Si:P. *Physical Review B*, 44(16):9045–9047, October 1991.

[MI11]    K. Momma and F. Izumi. *VESTA3* for three-dimensional visualization of crystal, volumetric and morphology data. *Journal of Applied Crystallography*, 44(6):1272–1276, December 2011.

[Mot68]    N. F. Mott. Conduction in glasses containing transition metal ions. *Journal of Non-Crystalline Solids*, 1(1):1–17, December 1968.

[MS96]    G. D. Mahan and J. O. Sofo. The best thermoelectric. *Proceedings of the National Academy of Sciences*, 93(15):7436–7439, July 1996.

[MW06]    W. Martienssen and H. Warlimont. *Springer Handbook of Condensed Matter and Materials Data*. Springer Handbook of Condensed Matter and Materials Data. Springer, 2006.

[NAS05]    NASA. Crystallization Kinetics of a Solid Oxide Fuel Cell Seal Glass by Differential Thermal Analysis . In *Ninth International Symposium on Solid Oxide Fuel Cells*, 2005.

[Nic08]    M. C. Nicolaou. *Thermoelectric Figure of Merit of Degenerate and Nondegenerate Semiconductors*. PhD thesis, Northeastern University, Boston, 2008.

[NPK06]   G. S. Nolas, J. Poon, and M. Kanatzidis. Recent Developments in Bulk Thermoelectric Materials. *MRS Bulletin*, 31(3):199–204, March 2006.

[OAY09]   M. Ohtaki, K. Araki, and K. Yamamoto. High Thermoelectric Performance of Dually Doped ZnO Ceramics. *Journal of Electronic Materials*, 38(7):1234–1238, June 2009.

[OK07]    H. Ohta and S. Kim. Giant thermoelectric Seebeck coefficient of a two-dimensional electron gas in $SrTiO_3$. *Nature Materials*, 6(2):129–134, January 2007.

[Ola05]   G. A. Olah. Beyond Oil and Gas: The Methanol Economy. *Angewandte Chemie International Edition*, 44(18):2636–2639, March 2005.

[Ons31a]  L. Onsager. Reciprocal Relations in Irreversible Processes. I. *Physical Review*, 37(4):405–426, February 1931.

[Ons31b]  L. Onsager. Reciprocal Relations in Irreversible Processes. II. *Physical Review*, 38(12):2265–2279, December 1931.

[OOEA94]  M. Ohtaki, D. Ogura, K. Eguchi, and H. Arai. High-temperature thermoelectric properties of $In_2O_3$-based mixed oxides and their applicability to thermoelectric power generation. *Journal of Material Chemistry*, 4(5):653–656, 1994.

[OOK06]   S. Ohta, H. Ohta, and K. Koumoto. Grain Size Dependence of Thermoelectric Performance of Nb-Doped $SrTiO_3$ Polycrystals. *Journal of the Ceramic Society of Japan*, 114(1325):102–105, January 2006.

[Pel34]   J. C. A. Peltier. Nouvelles expériences sur la caloricité des courants électrique. *Annales de Chimie et de Physique*, 56(1):371–386, 1834.

[Pet10]   D. Peter. Anderson-Lokalisierung, 2010. Talk, Universität Stuttgart.

[Pil69]   L. A. B. Pilkington. Review Lecture. The Float Glass Process. *Proceedings of the Royal Society of London. A. Mathematical and Physical Sciences*, 314(1516):1–25, December 1969.

[PJBA61]  W. J. Parker, R. J. Jenkins, C. P. Butler, and G. L. Abbott. Flash Method of Determining Thermal Diffusivity, Heat Capacity, and Thermal Conductivity. *Journal of Applied Physics*, 32(9):1679–1684, September 1961.

[PP72]     M. Pollak and G. E. Pike.  ac Conductivity of Glasses. *Physical Review Letters*, 28(22):1449–1451, May 1972.

[RCF98]    P. Riello, P. Canton, and G. Fagherazzi.  Quantitative Phase Analysis in Semicrystalline Materials Using the Rietveld Method. *Journal of Applied Crystallography*, 31(1):78–82, February 1998.

[RGN99]    R. Ray, A. Ghoshray, and K. Nakamura.  $^{59}$Co NMR studies of metallic $NaCo_2O_4$. *Physical Review B*, 59(14):9454–9461, April 1999.

[Röm96]    H. Römpp. *Lexikon der Chemie*. Thieme, 1996.

[SA64]     E. F. Steigmeier and B. Abeles.  Scattering of Phonons by Electrons in Germanium-Silicon Alloys. *Physical Review*, 136(4A):1149–1155, November 1964.

[SA94]     D. Stauffer and A. Aharony. *Introduction to Percolation Theory*. Taylor & Francis, 1994.

[Sam73]    G. V. Samsonov. *The Oxide Handbook*. Plenum, 1973.

[Sch88]    H. G. Schuster. *Deterministic Chaos - An Introduction*. VCH, 1988.

[Sch00]    B. M. Schulz. *Diffusion in Gläsern und anderen Komplexen Systemen*. PhD thesis, Universität Halle, 2000.

[Sch11]    H. Scholze. *Glass: Nature, Structure, and Properties*. Springer, 2011.

[See22]    T. J. Seebeck.  Magnetische Polarisation der Metalle und Erze durch Temperatur-Differenz.  *Abhandlungen der Akademie der Wissenschaften Berlin*, pages 265–373, 1822.

[SF03]     M. Shikano and R. Funahashi. Electrical and thermal properties of single-crystalline $(Ca_2CoO_3)_{0.7}CoO_2$ with a $Ca_3Co_4O_9$ structure. *Applied Physics Letters*, 82(12):1851–1853, March 2003.

[SHJ11]    J. R. Szczech, J. M. Higgins, and S. Jin. Enhancement of the thermoelectric properties in nanoscale and nanostructured materials. *Journal of Materials Chemistry*, 21(12):4037–4055, 2011.

[Sin00]    D. J. Singh.  Electronic structure of $NaCo_2O_4$.  *Physical Review B*, 61(20):13397–13402, May 2000.

[SJ81]      Y. Sato and R. Jeanloz. Phase transition in SrO. *Journal of Geophysical Research: Solid Earth*, 86(B12):11773–11778, December 1981.

[Sla95]     G. A. Slack. New Materials and Performance Limits for Thermoelectric Cooling. In D. M. Rowe, editor, *CRC Handbook of Thermoelectrics*, pages 407–437. Taylor & Francis, 1995.

[SP03]      A. Steinfeld and R. Palumbo. Solar Thermochemical Process Technology. In R. A. Meyers, editor, *Encyclopedia of Physical Science and Technology*, pages 237–256. Academic Press, New York, 3rd edition, 2003.

[ST08]      J. G. Snyder and E.S. Toberer. Complex Thermoelectric Materials. *Nature Materials*, 7(2):105–114, February 2008.

[STC$^+$12]   A. Sotelo, M.A. Torres, G. Constantinescu, S. Rasekh, J.C. Diez, and M.A. Madre. Effect of Ag addition on the mechanical and thermoelectric performances of annealed $Bi_2Sr_2Co_{1.8}O_x$ textured ceramics. *Journal of the European Ceramic Society*, 32(14):3745–3751, June 2012.

[Sto59]     S. D. Stookey. Catalyzed Crystallization of Glass in Theory and Practice. *Industrial and Engineering Chemistry*, 51(7):805–808, July 1959.

[Ter03]     I. Terasaki. Transport properties and electronic states of the thermoelectric oxide $NaCo_2O_4$. *Physica B: Condensed Matter*, 328(1–2):63–67, April 2003.

[Tes13]     R. Teschner. *Glasfasern*. Springer Berlin Heidelberg, 2013.

[TSU97]     I. Terasaki, Y. Sasago, and K. Uchinokura. Large thermoelectric power in $NaCo_2O_4$ single crystals. *Physical Review B*, 56:12685–12687, November 1997.

[vBEF01]    K. van Benthem, C. Elsässer, and R. H. French. Bulk electronic structure of $SrTiO_3$: Experiment and theory. *Journal of Applied Physics*, 90(12):6156–6164, December 2001.

[Vog92]     W. Vogel. *Glaschemie*. Springer, 1992.

[WEL96]     E. J. Winder, A. B. Ellis, and G. C. Lisensky. Thermoelectric Devices: Solid-State Refrigerators and Electrical Generators in the Classroom. *Journal of Chemical Education*, 73(10):940, October 1996.

[Wes07]    T. Westphal. *Quantitative Rietveld-Analyse von amorphen Materialien*. PhD thesis, Martin-Luther-Universität, Halle-Wittenberg, 2007.

[Woo88]    C. Wood. Materials for thermoelectric energy conversion. *Reports on Progress in Physics*, 51(4):459, April 1988.

[WRCO03]   Y. Wang, N. S. Rogado, R. J. Cava, and N. P. Ong. Spin entropy as the likely source of enhanced thermopower in $Na_xCo_2O_4$. *Nature*, 423(6938):425–428, May 2003.

[WS94]     A. Winkelmann and O. Schott. Ueber thermische Widerstandscoefficienten verschiedener Gläser in ihrer Abhängigkeit von der chemischen Zusammensetzung. *Annalen der Physik*, 287(4):730–746, 1894.

[YC09]     C. Yu and K.T. Chau. Thermoelectric automotive waste heat energy recovery using maximum power point tracking. *Energy Conversion and Management*, 50(6):1506 – 1512, April 2009.

[YKMH05]   S. Hébert Y. Klein, D. Pelloquin, A. Maignan, and J. Hejtmanek. Thermoelectric $[Sr_2(Bi,Co)_{n-2}O_n]^{RS}[CoO_2]_{1.8}$ layer cobaltites: The role of the intergrowth between the n = 3 and n = 4 terms. *Journal of Applied Physics*, 98(1):013701, July 2005.

[YUT02]    T. Yamamoto, K. Uchinokura, and I. Tsukada. Physical properties of the misfit-layered (Bi,Pb)-Sr-Co-O system: Effect of hole doping into a triangular lattice formed by low-spin Co ions. *Physical Review B*, 65(18):184434, May 2002.

[Zac32]    W. H. Zachariasen. The atomic arrangement in glass. *Journal of the American Chemical Society*, 54(10):3841–3851, October 1932.

# Danksagung

Aus Datenschutzgründen entfernt.

# Lebenslauf

Aus Datenschutzgründen entfernt.